UNIVERSIDADE FEDERAL DE SÃO CARLOS (UFSCar)

CENTRO DE CIÊNCIAS EXATAS E DE TECNOLOGIA

PROGRAMA DE PÓS GRADUAÇÃO EM FÍSICA

RAFAELLA BARTZ PENA

Correlation Between Structure and Optical Properties of Lead Metasilicate Glass-Ceramic Under High Hydrostatic Pressures

Supervisor: Prof. Dr. Paulo Sergio Pizani

São Carlos, 2022

UNIVERSIDADE FEDERAL DE SÃO CARLOS (UFSCar)

CENTRO DE CIÊNCIAS EXATAS E DE TECNOLOGIA

PROGRAMA DE PÓS GRADUAÇÃO EM FÍSICA

RAFAELLA BARTZ PENA

Correlation Between Structure and Optical Properties of Lead Metasilicate Glass-Ceramic under High Hydrostatic Pressures

Thesis presented to the Graduate Program in Physics at the Universidade Federal de São Carlos as a partial requirement to obtain the degree of Doctor of Science.

Concentration area: Applied Physics

Supervisor: Prof. Dr. Paulo Sergio Pizani

São Carlos, 2022

UNIVERSIDADE FEDERAL DE SÃO CARLOS

Centro de Ciências Exatas e de Tecnologia
Programa de Pós-Graduação em Física

Folha de Aprovação

Defesa de Tese de Doutorado da candidata Rafaella Bartz Pena, realizada em 21/09/2022.

Comissão Julgadora:

Prof. Dr. Paulo Sergio Pizani (UFSCar)

Prof. Dr. Edgar Dutra Zanotto (UFSCar)

Prof. Dr. Marcelo Nalin (UNESP)

Prof. Dr. Silvio Buchner (UFRGS)

Prof. Dr. Valmor Roberto Mastelaro (IFSC/USP)

O Relatório de Defesa assinado pelos membros da Comissão Julgadora encontra-se arquivado junto ao Programa de Pós-Graduação em Física.

To my beloved family:

My dad Nilson, my mom Deonise and my sister Gabriella

ACKNOWLEDGEMENTS

Foremost, I would like to thank my supervisor and mentor Prof. Dr. Paulo Pizani for his valuable scientific and personal instructions over the years that began when I was a sophomore student. Have been valuable to me your guidance and support. Thanks for encouraging me to pursue ideas and ideals that have been modeling me as a researcher!

I am very grateful to Dr. Christine Martinet and Dr. Thierry Deschamps for the supervision and support during my time in France. I wish to thank the then master student Valentin Laurent with whom I worked closely during my first six months in France developing part of the research presented here. Generally, I thank the entire SOPRANO group for the welcoming, amazing time, and memorable discussions during my internship… *Merci beaucoup!*

I am grateful to the GEOR laboratory team, with whom I had the pleasure to work together and learn over the years: Dr. Renilton Correa, Dr. David Sampaio, Dr. Thiago Cunha, Dr. Ana Curcio, and Prof. Dr. Ariano Rodrigues. My sincere gratitude goes to Dr. Benjamin Moulton who besides inspiring me, has opened many doors across the world! Beyond the scientific matter, I thank you all for your friendship!

I recognize this work would not be possible without the effort of some collaborators of ours with whom I am very thankful: Prof. Dr. Adalberto Picinin and Prof. Dr. Jose Rino for the molecular dynamics bases; MSc. Ricardo Lancelotti for the crystalline samples and some measurements.

A special thanks to UFSCar and the Physics Department for the academic formation. I could not name them all, but I am very thankful for the professors who inspired me in my quest for scientific knowledge!

I also thank the friends from São Carlos and 'from far away' I got the pleasure of meeting, and who have made this journey memorable…

I would like to thank sincerely my family for teaching me to pursue 'knowledge, the good nobody can take away from me'. Your love and unconditional support are the most valuable goods I own…

Very warm and special thanks also to Ludovico. It has been a stressful path the last years of my Ph.D., yet amazing and magical at your side, my love!

Finally, yet importantly, I am grateful to São Paulo Research Foundation (FAPESP) for the financial support through the research grants 2017/118968-2 and 2019/11446-6.

« L'essentiel est invisible pour les yeux »
Antoine de Saint-Exupéry

ABSTRACT

Glass structures are determined by not only composition, pressure, and temperature but also by the pressure and thermal histories in which the glass was submitted. In this thesis, a systematic study of these variables was performed in undoped and cobalt-doped lead metasilicate ($PbSiO_3$) glasses and mainly probed by Raman spectroscopy. High pressure was applied in a Diamond Anvil Cell (DAC), and the samples were studied *ex-situ* and *in-situ*. *Ex-situ* Raman investigation appoints for an unusual increase in the non-bridging oxygens (NBO) population, at the expense of the bridging oxygens (BO) population, leading to slight depolymerization of the densified metasilicate structure. *In-situ* investigation of this glass under pressure suggests the densification mechanisms occurring via the formation of an intermediary more polymerized state. Such modifications are accompanied by a change in the lead environment with the formation of highly coordinated PbO_n polyhedra. High-temperature investigations were performed in isothermal and non-isothermal runs, providing evidence that the phase evolution from the glass to the stable alamosite is intermediated by two metastable crystalline phases, with a temperature-dependent crystallization path. For the same composition submitted to extremal conditions, the controlling of these structures may offer vast possibilities to tailor the glass-ceramic optical properties.

Keywords: *Lead Metasilicate Glass; High-Pressure; Overall Crystallization; Raman Spectroscopy; Photoluminescence.*

RESUMO

Estruturas vítreas são determinadas não apenas pela composição, pressão e temperatura, mas também pelas histórias térmicas e de pressão em que o vidro foi submetido. Nesta tese, um estudo sistemático dessas variáveis foi realizado em vidros de metassilicato de chumbo ($PbSiO_3$) não dopado e dopados com cobalto, e analisado principalmente por espectroscopia Raman. Altas pressões foram aplicadas utilizando uma célula diamante do tipo bigorna, e as amostras foram estudadas *ex-situ* e *in-situ*. Os resultados de espectroscopia Raman *ex-situ* apontam para um aumento incomum na população de oxigênios não ponteantes (NBO), às custas da população de oxigênios ponteantes (BO), levando a uma sutil despolimerização da estrutura densificada do metasilicato. A investigação *in situ* deste vidro sob pressão sugere que os mecanismos de densificação ocorrem através da formação de um estado intermediário mais polimerizado. Tais modificações são acompanhadas por uma mudança no ambiente do íon de chumbo, com a formação de poliedros PbO_n altamente coordenados. Investigações a altas temperaturas foram realizadas com aquecimentos isotérmicos e não isotérmicos, fornecendo evidências de que a evolução estrutural do vidro para a alamosita é intermediada por duas fases cristalinas metaestáveis, com rotas de cristalização dependentes da temperatura. Para uma mesma composição química submetida a condições extremas, o controle da formação dessas estruturas pode oferecer amplas possibilidades de adequar as propriedades ópticas das vitrocerâmicas.

Palavras-chave: *Vidro Metasilicato de Chumbo; Altas Pressões; Cristalização Total; Espectroscopia Raman; Fotoluminescência.*

LIST OF PUBLICATIONS

1) D.C. Silva; D.V. Sampaio; J.H.L Silva; A.M. Rodrigues; **R.B. Pena**; B.J.A. Moulton; P.S. Pizani; J.P. Rino; R.S. Silva, "Synthesis of $PbO{\cdot}SiO_2$ glass by CO_2 laser melting method", *Journal of Non-Crystalline Solids*, vol. 522, p. 119572, 2019.

2) **R.B. Pena**, D. V. Sampaio, R. F. Lancelotti, T. R. Cunha, E. D. Zanotto, and P. S. Pizani, "In-situ Raman spectroscopy unveils metastable crystallization in lead metasilicate glass," *Journal of Non-Crystalline Solids*, vol. 546, p. 120254, 2020.

3) **R.B. Pena**, V. Laurent, T. Deschamps, E. Romeo, A. Picinin, C. Martinet and P.S. Pizani, "High-pressure plastic deformation of lead metasilicate glass accessed by Raman spectroscopy: Insights into the Q^n distribution", *Journal of Non-Crystalline Solids*, vol. 567, p. 120930, 2021.

4) D.V. Sampaio, **R.B. Pena**, B.J.A. Moulton, M.V. Rezende, D.C. Silva, R.S. Silva, T. R. Cunha, V.R. Mastelaro, E.D. Zanotto, P.S. Pizani, "Chromium in lead metasilicate glass: Solubility, valence, and local environment via multiple spectroscopy", *Ceramics International*, vol. 48, n. 1: p. 173-178, 2022.

5) **R.B. Pena**, T. Deschamps; A. Amato; S. Le Floch; P.S. Pizani; C. Martinet, "Normal to abnormal behavior of $PbSiO_3$ glass: A vibrational spectroscopy investigation under high-pressure", *Journal of Non-Crystalline Solids*, vol. 589: p. 121614, 2022.

6) T.R. Cunha; D.V. Sampaio; **R.B. Pena**; B.J.A. Moulton; R.F. Lancelotti; F.G. Alabarse; A.D. Rodrigues; E. D. Zanotto; P. S. Pizani, "Thermal expansion and compressibility of alamosite ($PbSiO_3$) determined by in-situ synchrotron X-ray diffraction", Ceramics International (in press).

7) **R.B. Pena**; T.R. Cunha; D.V. Sampaio; A.D. Rodrigues; P.S. Pizani, "Temperature Effects on the Vibrational Raman-modes of Alamosite ($PbSiO_3$)" (to be submitted).

8) **R.B. Pena** *et al.,* "In situ Structural Analysis of Lead Metasilicate Glasses under High Pressure a Raman Scattering and Molecular Dynamics Combinatory Study" (manuscript in preparation).

9) **R.B. Pena** *et al.*, "Cold- and Hot-Densified Depolymerized Glass: A Multiscale Vibrational Investigation" (manuscript in preparation).

LIST OF FIGURES

LIST OF TABLES

LIST OF ABBREVIATIONS AND ACRONYMS

BO	Bridging Oxygen
BP	Boson Peak
CN	Coordination Number
<CN>	Average Coordination Number
CRN	Continuous Random-Network
DAC	Diamond Anvil Cell
DSC	Differential Scanning Calorimetry
DTA	Differential Thermal Analysis
HWHM	Half Width at Half Maximum
G-L	Gaussian-Lorentzian
$g(r)$	Pair Correlation Function
H-PS	Hexagonal $PbSiO_3$
LRO	Large-Range Order
L-PS	Low $PbSiO_3$
MD	Molecular Dynamics
MRN	Modified Random Network
MRO	Medium-Range Order
NMR	Nuclear Magnetic Resonance
NBO	Non-Bridging Oxygen

O^{2-}	Free-Oxygen
PL	Photoluminescence
SCL	Super Cooled Liquid
SRO	Short-Range Order
T	Temperature
T_c	Crystallization Temperature
T_g	Glass Transition Temperature
T_m	Melting Temperature
P	Pressure
P’	Elastic Limit
Patmo	Atmospheric Pressure
Pmax	Maximum Pressure
PTM	Pressure Transmitting Medium
PS	Lead Metasilicate, $PbSiO_3$
Q^n	Quaternary Entity or Population
$<Q^n>$	Average Quaternary Population
XAS	X-Ray Absorption Spectroscopy
XPS	X-Ray Photoelectron Spectroscopy
XRD	X-Ray Diffraction

CONTENTS

INTRODUCTION

Glass-ceramics are prospective materials obtained through the partial and controlled crystallization of the glass. By interrupting the heat treatment in certain stages, different stable and metastable crystalline phases can precipitate in varying crystallization degrees, resulting in glass-ceramics with essentially the same composition but distinct properties [1, 2]. The pressure further expands the degree of freedom, modifying the glassy and crystalline structures, which leads to a final composite with a tailored combination of properties.

For the development of glass-ceramics, controlled nucleation is mandatory [1, 2], whereas a vast number of glass compositions nucleate heterogeneously and randomly on the surface [3, 4], requiring the addition of nucleant agents [5, 6]. To this end, the introduction of transition metal ions in these glasses is two-fold. Firstly, these ions can aid in inducing favored nucleation sites. Secondly, these dopants present electronic energy level distributions sensitive to the surrounding environment, and hence optical properties that are tunable [7, 8].

Despite the current concern for eliminating lead from daily use materials, lead-bearing glasses still find technological applications due primarily to their high density, high refractive index, X- and γ-ray attenuation [9]. Because silica is the archetypal glass and the system $PbO\text{-}SiO_2$ forms glass over a wide range of compositions, unraveling the nuances of their structure under extreme conditions may shed further light on the structural role of Pb and guide the choice of ecological alternatives offering similar properties.

To this end, the lead metasilicate ($PbSiO_3$, abbreviated as PS) glass is an interesting model system. Among the metasilicates, the PS shows an excellent glass-forming ability even at low cooling rates, whereas other compositions such as alkali and alkaline earth metasilicates are reluctant glass formers [10]. The PS glass also presents important fundamental and technological properties well tabulated in the literature at room condition and/or in a wide range of temperatures: crystal growth rates for the isochemical alamosite [10, 11]; diffusion coefficients of network cations [10, 12-14]; mechanical properties [15-17]; optical properties [17-21]; structural relaxation [22]; viscosity [10, 22-26]; *etc.*

Before the work of this thesis, as an undergraduate student, I took part in the synthesis and characterization of a set of doped glasses presenting minor gradual variations to the PS

composition with the insertion of transition metal ions comprising chromium, cobalt, and nickel. The doped glasses were investigated at room conditions by multi-spectroscopic means leading to a collaborative publication for chromium-doped PS glass [27]. Among the investigated dopants, cobalt was the most optically appealing, presenting a red photoluminescent band, which inspired the main subject of this thesis towards its 'solo' investigation, sponsored by FAPESP through a direct doctorate scholarship.

This thesis globally addresses the "*Correlation Between Structure and Optical Properties of Lead Metasilicate Glass-Ceramic Under High Hydrostatic Pressures*", where the influence of each variable: pressure, temperature, and composition was carefully investigated. In the case of composite materials such as glass-ceramics, are of paramount importance the understanding of their constituents: (i) the glass matrix; (ii) the precipitated crystal(s); (iii) the interaction between these distinct phases. We explore the first two by Raman spectroscopy, a vibrational probe efficient to accompany the modifications under extreme conditions, such as high pressure and high temperature. Noteworthy, pressure and temperature studies are complementary: temperature affects the population of different energy levels, enabling one to study concurrent processes separated by an energy barrier, whereas the pressure may affect the equilibrium distance between the atoms, hence affecting the configuration of the energy barrier [8].

Throughout the chapters, polymerization and depolymerization permeate the description of the structural modifications driven under extreme conditions. According to the Merriam-Webster dictionary, polymerization can be generally defined as "*a chemical reaction in which two or more molecules combine to form larger molecules that contain repeating structural units*". In silicates, such a reaction occurs by the formation of Si-O bonds, when SiO_4 tetrahedra increase their degree of connectivity within the network. In its turn, depolymerization is the reverse structural mechanism.

The chapters have been ordered to constructively understand the cobalt-doped lead metasilicate glass under extreme conditions. The outline is as follows: the first chapter delivers theoretical fundamentals regarding the nature of glass matter and vibrational spectroscopy. In the second chapter, we present the methodologies comprising the samples syntheses; Raman instrumental description, quantitative spectral analysis; general scheme of conventional high-pressure experiments performed in a diamond anvil cell (DAC), and the search for alternative

pressure calibrants to replace ruby, as required for the characterization of the photoluminescent signal of the doped glass upon compression.

In the course of this thesis, a great deal of effort was made to understand the pressure effects on the structure of PS glass, which progressed through the collaborative effort between the *Institute Lumière Matière* (ILM-France) and *Grupo de Espectroscopia Óptica e Espalhamento Raman* (GEOR-Brazil), culminating in an internship abroad sponsored by FAPESP. We have investigated by vibrational spectroscopies two non-equivalent pressure conditions: after densification at room temperature and different maximum pressures (Chapter 3) and during the compression and decompression cycle at room temperature (Chapter 4), *i.e.*, *ex-situ* and *in-situ* experiments, respectively. *Ex-situ* measurements were performed after taking away the pressure, focusing on the resulting irreversible effects when the glass is retrieved to room condition. On the other hand, *in-situ* experiments were driven while the system was under pressure, then providing further information about the pathways involved and the pressure mechanisms leading to the permanent transformation. In this context, pressure variables were here distinguished into maximum pressure (Pmax) and pressure (P), whether the study was performed *ex-situ* or *in-situ*, respectively.

In Chapter 5, non-isothermal and isothermal heating treatments were systematically applied to understand the phase evolution during the overall crystallization of PS glass. Our *in-situ* Raman investigation indicated temperature-dependent crystallization pathways, as published therein [28]. Departing from the total crystallization as in Chapter 6, the stable alamosite and the metastable hexagonal (H-PS) and low-temperature (L-PS) polymorphs were investigated under extreme conditions to shed further light on the crystallization routes, phase transformations, and stability in the isochemical $PbSiO_3$ system.

Finally, but importantly, the seventh chapter focuses on the cobalt-doped PS samples and the effects of cobalt content with temperature or pressure. In small concentrations, the dopant is expected not to modify expressively the glass structure and the crystallization dynamics. Such that, the results obtained for the PS glass under extreme conditions are extended to the cobalt-doped glasses, which presented the incremental photoluminescent signal in relation to the undoped glass.

A. Goals

The goals of this thesis comprised

(I) Describing the pressure-induced effects on the structure of lead metasilicate glass;

(II) Understanding the *in-situ* structural modifications of the glass upon compression and the pressure mechanisms involved;

(III) Studying the dynamics of crystallization, achieving comprehensive conditions to stabilize the metastable and stable crystalline phases;

(IV) Describing the effect of the temperature and pressure on the precipitated crystalline phases;

(V) Verify the composition range for which the crystallization of the undoped glass extends towards the cobalt-doped samples;

(VI) Mapping the vibrational and optical properties of the resulting glass ceramics as a function of the precipitated crystalline phases.

CHAPTER 1 – FUNDAMENTALS

1.1. Glass

The development of optical glass and optical science trails parallelly, exemplified by the construction of the first telescopes and microscopes, which allowed respectively to expand the knowledge of the universe in which we are inserted and the discovery of the cell and microorganisms expanding the human knowledge towards either the 'very big' as the 'very small' scales [29]. Nowadays, glasses find a wide range of important applications in our everyday life and prospects for technological development in the very close future, leading some experts to denote the current period as the 'Glass Age' [30].

More fundamentally, since the seminal work of Zachariasen [31], the glass structure and its overall comprehension have evolved over the years. In 2017, Zanotto *et al.* [32] published a critical review of some of the most popular definitions in the literature and proposed an extended glass definition such as: *"nonequilibrium, noncrystalline condensed state of matter that exhibits a glass transition. The structure of glasses is similar to that of their parent supercooled liquids (SCL), and they spontaneously relax toward the SCL state. Their ultimate fate is to solidify, i.e., crystallize"*. As in the core of the definition, glasses are universally characterized by their (i) glass transition; (ii) thermodynamic instability, and (iii) non-crystalline structure, fundamental concepts further discussed below.

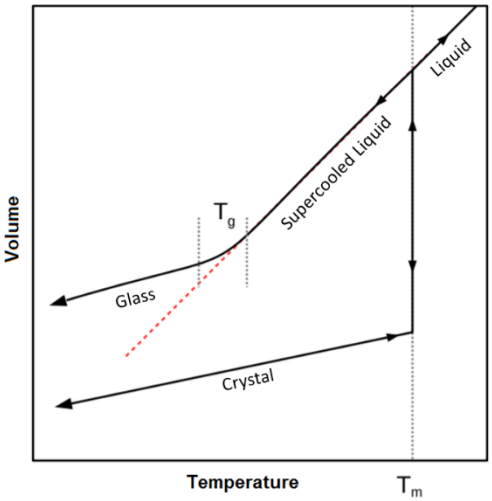

Figure 1.1: Volume as a function of the temperature for a glass-forming substance showing liquid, supercooled liquid (SCL), glass, and crystal states, with T_m= melting temperature and T_g= glass transition temperature.

I. Glass Transition

The glass transition temperature (T_g) between the SCL and the glass state does not constitute a thermodynamic phase transition [33]. In fact, it is a kinetic transition whose phenomenological description is associated with the structural relaxation process, *i.e.*, translational and rotational movements of the structural units, which introduces an internal time scale to the

system. The glass transition can be interpreted in terms of the relation between this internal time scale and the external observation time. While in liquids ($T > T_m$, m = melting) and in SCL ($T_g < T < T_m$) the average relaxation time is short, in glasses ($T < T_g$) this process happens in very long times, compared to the observation time [32]. In its turn, the glass transition is the temperature range (Figure 1.1) where the average time structural relaxation is comparable to the observation time. It is worth mentioning that glass transition temperatures are not intrinsic to a given composition, but depend significantly on the analyzed property, the experimental technique used, and the cooling and pressure histories [34].

II. Thermodynamic Instability

Glasses are thermodynamically unstable, as a consequence, their properties depend not only on the composition but also on the thermal and pressure histories, as well as on the observable time [33, 35]. This instability manifests by spontaneous relaxation towards the SCL state (Figure 1.2a) and subsequent crystallization [32].

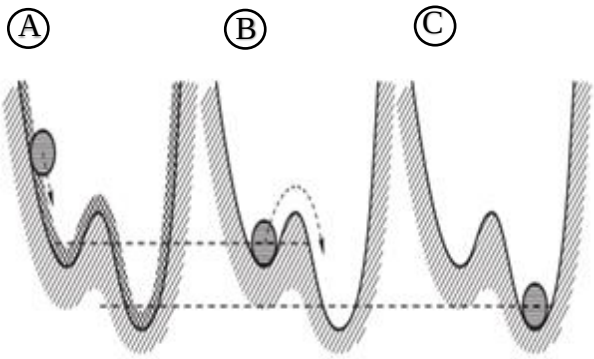

Figure 1.2: Mechanical analogy for the interpretation of thermodynamic stability differences between (a) glass; (b) SCL, and (c) crystals. Adapted from Gutzow et al., 1995 [33].

From a mechanical analogy with a potential well [33], the SCL corresponds to a thermodynamically metastable state, presenting as a higher local minimum (Figure 1.2b), stable for small fluctuations, but unstable for high deviations from the initial position, while the crystal represents a stable state, illustrated as the absolute minimum (Figure 1.2c). In this sense, crystallization consists of the nucleation process, from which the energy barrier is transposed by nucleation through small composition fluctuations, followed by the spontaneous growth process occurring through limited diffusion from the surrounding.

III. Non-crystalline Structure

Glasses present non-crystalline structures, with the translational periodicity present in crystal counterparts then absent, configuring a structure topologically disordered over long-range orders (LRO), but with preserved short-range order (SRO), as displayed in Figure 1.3 [36].

The first formulation to describe the glass structure referred to as continuous random-network (CRN) found support in the works developed by Zachariasen [31] and Warren [37]. The CRN model pictures the silicate glass as a continuously homogeneous structure, where the cations are randomly distributed in the interstices of a corner-sharing SiO_4 tetrahedra network.

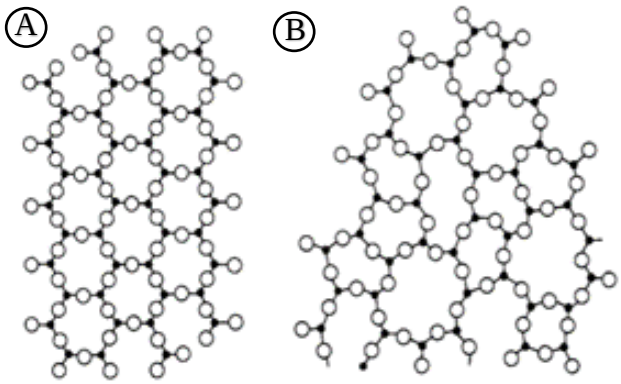

Figure 1.3: Hypothetical compound A_2O_3 with (a) crystalline and (b) glassy two-dimensional structure. Retrieved from Zachariasen, 1932 [31].

According to the CRN model [31], the structure of oxide glasses can configures as a three-dimensional network of polyhedra interconnected by vertexes. Thus, due to interatomic interactions, these structural entities present SRO, with well-defined coordination, atomic angles, and distances. In turn, the long-range disorder is due to the various connecting angles from adjacent polyhedra relative to the oxygen atoms that interconnect them, presenting homogenous and topologically connected along the network [38]. In general, structural ordering in glass decreases with increasing distance, configuring as organized for SRO (2 - 5 Å), disorganized for LRO (> 20 Å), whereas the medium range order (MRO) is mostly interpreted statistically [39]. Noteworthy, the SRO comprises the polyhedral unity and its interconnection to the other adjacent structural unities [40].

Still from the CRN model [31], a given cation can be distinguished into 'network former' or 'network modifier', whether it forms a polyhedron network or not, respectively. For a pure former glass, every polyhedron has its corners ideally connected to another (so-called Q^4 in the notation described below), while for multi-component oxide glasses, the progressive insertion of modifier cations leads to network depolymerization. Due to this fact, oxygens are labeled 'bridging oxygens' or 'non-bridging oxygens', taking into account if they make the connection between two network former polyhedra or not. In this sense, the connectivity

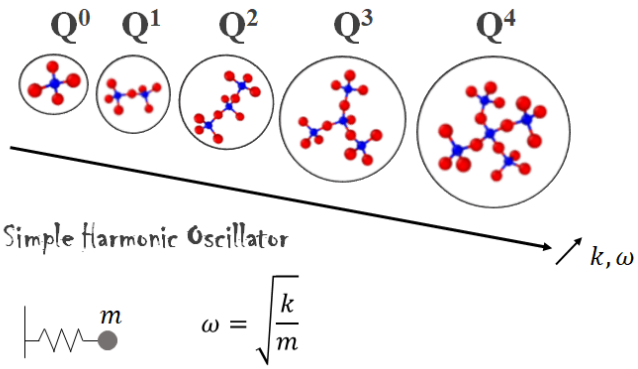

Figure 1.4: The Q^n units picture the SiO_4 tetrahedra connectivity within the glass network, where n ranges from 0 to 4 bridging oxygens per tetrahedron. Their vibrational dynamics are analogous to the simple harmonic oscillator with different spring constant.

in silicate glasses can be interpreted statistically in terms of the Q^n ('quaternary') population species, where n varies from 0 to 4 and is the number of bridging oxygens connected to a given SiO_4 tetrahedron [39], as illustrated in Figure 1.4.

Despite the easiness of explaining some important structural concepts of glass, the alleged homogeneity stated in the core of the CRN model came into the debate. In 1985, the investigation of soda silicates by X-ray absorption spectroscopy performed by Greaves [41] revealed the heterogeneous distribution of modified cations within the glass network. Such an observation gave rise to the Modified Random Network (MRN) model, later extended to other glass compositions [42]. The MRN model is based on the complementary presence of cation-rich domains percolating the silicate main lattice.

In the context of the MRN model, it is further introduced the free oxygen (O^{2-}), which refers to O *not* bonded to Si but to the modifier cation (*i.e.,* M-O-M), potentially connecting the sub-lattice. The equilibrium between the oxygen species occurs through the depolymerization reaction [43, 44]:

$$BO + O^{2-} \leftrightarrow 2NBO \tag{1.1}$$

Where BO is the bridging oxygen and NBO is the non-bridging oxygen, respectively bonding two Si to each other (*i.e.,* Si-O-Si), or one Si to a modifier cation (*i.e.,* Si-O-M). We highlight the O^{2-} at the same side as the BO in Eq. (1.1), such that an increase in NBO implies a decrease in both, BO and O^{2-}. The O^{2-} is considered the most reactive among the oxygen species, important for understanding thermodynamic and kinetic reactions of natural silicates [43-46].

A. Lead Metasilicate Glass Structure

The $PbO\text{-}SiO_2$ glass system displays a wide range of compositions, reaching nominally up to 96 mol.% PbO [47]. Because of their exceptionally good glass-forming ability, these glasses have been the focus of a great number of structural studies at ambient pressure comprising: nuclear magnetic resonance (NMR) [48-58]; X-ray and/or neutron diffraction [54, 57, 59-65]; X-ray absorption spectroscopy (XAS) [52, 66, 67]; X-ray photoelectron spectroscopy (XPS) [43, 68-70] Raman spectroscopy [23, 55, 71-77]; infrared spectroscopy [55, 72-74, 78, 79]; and molecular dynamics (MD) simulations [67, 77, 80-82]. Many of these studies attempted to describe the role played by lead atoms in the glass network, whether as modifiers or intermediate cations.

Nevertheless, there is no consensus in the literature on the precise composition where this transition in the role of lead occurs.

Previous reviews addressing the SRO in lead silicate glass can be found therein [83-86]. At ambient conditions, the PS glass presents well-defined tetrahedral silicon sites organized mostly as Q^2 entities, *i.e.*, interconnected with the other two silicon tetrahedra [23, 51, 53, 55, 77]. As a straight consequence, these glasses present a depolymerized structure, indicated by their high proportion of NBO to BO. A modest fraction of O^{2-} is reported for the metasilicate composition, evaluated at around 2% as probed by ^{17}O NMR [56]. Focusing on the ordering around lead, despite the lack of consensus in the literature about the structural role played by these cations, most of the structural studies performed in the last two decades converged on PbO_3 and PbO_4 [51, 52, 54, 57, 64, 66, 67].

1.2. Raman Spectroscopy

I. Selection Rule

In this work, pressure and temperature effects on the glass structure were investigated by inelastic vibrational spectroscopy that relies on the interaction of light with the matter by inelastic scattering, probing the vibrational energy of the molecules. In this way, the structural modifications under extreme conditions are indirectly accessed by the related modifications in their dynamical character.

By the classical approach, when monochromatic radiation is focused on a material medium, the interaction of the electromagnetic field occurs with the electronic cloud of atoms, which consequently deforms. The electric field vector of radiation can be described as varying with time in such a way that:

$$\boldsymbol{E}(t) = \boldsymbol{E_0}\, cos(\omega_o t) \tag{1.2}$$

Where E_0 is the amplitude and ω_0 is the angular frequency of the incident light, usually a laser beam. When light is irradiated on the matter, an electric dipole moment is induced:

$$\boldsymbol{P}(t) = \boldsymbol{\alpha}(\boldsymbol{t}).\boldsymbol{E}(\boldsymbol{t}) = \boldsymbol{\alpha}(\boldsymbol{t}).\boldsymbol{E_0}\, cos(\omega_o t) \tag{1.3}$$

Here $\boldsymbol{\alpha}$ is the electronic polarizability tensor. Proceeding with an expansion of $\boldsymbol{\alpha}$ as a Taylor series around the equilibrium position:

$$\boldsymbol{\alpha}(\boldsymbol{t}) = \boldsymbol{\alpha_0} + \left(\frac{\partial \alpha}{\partial q}\right)_{q_0} \boldsymbol{q}(t) + \ \ldots \tag{1.4}$$

With **q** normal coordinate of atomic vibration that indicates nuclear displacement. If the vibration atoms vibrate with a frequency ω_m, it can be assumed based on the harmonic model of a solid:

$$\boldsymbol{q}(t) = \boldsymbol{q_0}\, cos(\omega_m t) \tag{1.5}$$

So that,

$$\boldsymbol{P}(t) = \boldsymbol{\alpha}(\boldsymbol{t}).\boldsymbol{E_0}\, cos(\omega_o t) = \boldsymbol{\alpha_0}\,\boldsymbol{E_0}\, cos(\omega_o t) + \left(\frac{\partial \alpha}{\partial q}\right)_{q_0} \boldsymbol{q_0}\,\boldsymbol{E_0}\, cos(\omega_o t)\, cos(\omega_m t) \tag{1.6}$$

Which can be rewritten as:

$$\boldsymbol{P}(t) = \boldsymbol{\alpha_0}\,\boldsymbol{E_0}\, cos(\omega_o t) + \frac{1}{2}\left(\frac{\partial \alpha}{\partial q}\right)_{q_0} \boldsymbol{q_0}\,\boldsymbol{E_0}\,[\cos[(\omega_o - \omega_m)t] + \cos[(\omega_o + \omega_m)t]] \tag{1.7}$$

The first term on the right in Eq. (1.7) represents the scattering in which the frequency of scattered radiation is the same as that of incident radiation (Rayleigh). In turn, the second term represents Raman scattering, with scattered light and energy frequency lower ($\omega_o - \omega_m$, Stokes) or higher than the incident ($\omega_o + \omega_m$, Anti-Stokes). The difference in frequency of the inelastically scattered to the incident photons is associated with the frequency of vibration of the network, providing, therefore information about the vibrational spectrum of the investigated material.

While Rayleigh scattering is always present, inelastic scattering is observed only if the following condition is satisfied:

$$\left(\frac{\partial \alpha}{\partial q}\right)_{q_0} \neq 0 \tag{1.8}$$

This way a selection rule for Raman scattering to occur is that a variation of polarizability with nuclear displacement must be non-zero, *i.e.*, the polarizability has to be modulated by atomic vibration. A quantum description of the vibrations in terms of phonons is presented in Appendix A, extending the formalism toward the non-crystalline matter.

Raman spectroscopy arises from the inelastic scattering of light by the 'optical' phonons probing the shift of frequencies in the range of THz, but is conventionally presented in wavenumber in unities of cm^{-1}:

$$\Delta\omega = 10^7 \left(\frac{1}{\lambda_0} - \frac{1}{\lambda_m}\right) \tag{1.9}$$

Where $\Delta\omega$ is the Raman shift expressed in wavenumber, λ_0 is the incident excitation light wavelength and λ_m is the scattered light wavelength, both in nm. Raman spectra are fingerprint signatures of the material at a given phase, being sensitive to the nature of the bonds and the group symmetries [87].

II. Lead Silicate Glasses

In this section, we summarize the main attributions regarding the Raman spectrum of PS glass, whereas those of the isochemical crystals are addressed in Chapter 6. Generally, vibrational spectra of lead silicate glasses were historically analyzed by gradually varying the lead concentration and observing the resulting spectral changes to the vitreous silica [23, 71, 72].

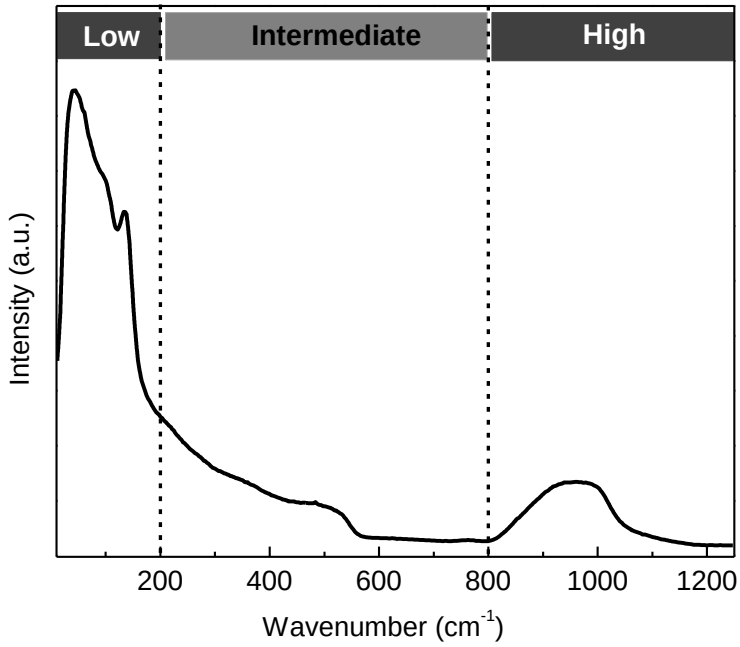

Figure 1.5: Raman spectrum of lead metasilicate glass at room conditions. The dashed lines evidence the border of the low, intermediate, and high wavenumber spectral regions.

PS glass spectrum (Figure 1.5) exhibits, at the low-wavenumber region, an intense peak referred to as the Boson peak (40 cm^{-1}), which is observed in all amorphous silicate materials, and whose nature is still a matter of discussion [88-90]; and two peaks (centered at 93 cm^{-1} and 137 cm^{-1}), both assigned to Pb-O vibration [23, 71, 72, 76]. The plateau observed between 460 and 550 cm^{-1} is attributed to delocalized vibrations with mixed O-Si-O bond stretching and characteristic bond bending [55]. In its turn, the asymmetrical high-wavenumber envelope (800-1200 cm^{-1}) is due to the symmetric stretching of the Si-O bonds composing the different Q^n units [23, 77]. Noteworthy, prior to any curve-fit procedure, the degree of polymerization described in terms of the Q^n distribution finds an easy analogy in the vibrational dynamics of simple harmonic oscillators, correlating directly the modulus of the spring constant with the characteristic frequency of vibrations (Figure 1.4). In other words, less polymerized Q^n units vibrate at characteristically

lower frequencies, whereas more polymerized Q^n units vibrate at higher frequencies. A more detailed discussion regarding the low- and high-wavenumber regions is addressed as follows.

A. Low-wavenumber region

A.1. Boson Peak

In the very low-wavenumber region of the Raman spectra, an intense asymmetrical broad peak is universally observed in glasses, consisting of an excess of vibrational density of states in contrast to the Debye prediction for crystals [91]. The so-called Boson peak (BP) has its physical origin controversial in the literature, a summary concerning the most relevant theoretical approaches can be found elsewhere [92].

We will focus here on the elastic heterogeneities approach, which finds strong theoretical and experimental evidences, explaining subjects such as the glass transition and the glass relaxation. According to this model proposed by Duval *et al.* [90], glasses display non-continuous structures configuring a collection of non-crystalline nanometric domains with distinct elastic constants. From this approach, the BP arises from the motion of these cohesive domains separated by softer interdomain zones [93].

Some studies in the literature address the relationship between the BP and intermediate length scales within the glass structure [91, 94]. Once this peak can be fitted as a Lognormal function [95], it indicates that the size distribution of these ‘clusters’ would also be Lognormal [96, 97], displaying a collection of domains with varying sizes such as a mosaic structure. Experimental means to probe the BP comprises inelastic neutron and Raman scattering spectroscopies.

As firstly perceived by Malinovsky *et al.* [91], the peak shape of the BP is universal for glasses showing different compositions. Meanwhile, peak parameters such as the position of the maximum and relative intensity of the peak are reported to modify with: the glass composition [98-100], temperature treatment [101, 102], and applied pressure [101, 103]. On various oxide glasses, the BP is more sensitive to pressure than to temperature [101]. Noteworthy, compression is reported to shift the BP maximum towards higher wavenumbers and to decrease the peak intensity [104-107].

A.2. Peaks at 93 cm^{-1} and 135 cm^{-1}

Raman spectra of lead glasses with distinct compositions [100, 108-111] and lead oxides [72] present bands at comparable wavenumbers, being therefore characteristic of the lead presence. Due to the large atomic mass of lead atoms, the frequencies of the Pb-O vibrations occur at the low region of the vibrational spectra.

By increasing the lead concentration, Hagiwara *et al.* [71] observed an intensification of the band at 135 cm^{-1}, attributed initially to the vibration of the Pb^{2+} ion. Afterward, this band was identified as being analogous to those found on the PS crystalline phases [72-74] and lead oxides [72], indicating the existence of Pb-O covalent bonding. Zahra et al. [112] ascribed both of the low-wavenumber Pb-O peaks to the PbO_4 pyramids, specifying the peak at 135 cm^{-1} as due to symmetric stretching vibrations of these polyhedra. Such assignment agrees with partial reports conducted on these glasses [73, 76, 78].

B. High-wavenumber Region

At the high-wavenumber region, the Raman spectrum of PS glass presents an asymmetrical envelope assigned to the symmetric stretching of Si-O bonds associated with the different Q^n species. In pristine lead metasilicate glasses, the Q^n distribution has been studied by NMR [51, 53, 55], Raman spectroscopy [23, 77], and MD simulations [77, 80]. From the reported studies, the structure of PS glass contains mostly Q^2 tetrahedra, although the difference on the absolute values (Table 1.1). We discuss below the quantifications performed by curve fit of the Raman spectra.

Table 1.1: Q^n distributions and average, $<Q^n>$ in PS glass according to different studies. Adapted from Sampaio et al., 2018 [77].

Reference	Method	Q^0	Q^1	Q^2	Q^3	Q^4	$<Q^n>$
Cormier et al. **[80]**	MD	2	19	42	30	7	2.2
Fayon et al. **[51]**	NMR	0	13	51	30	6	2.3
Schneider et al. **[53]**	NMR	0	21	47	26	6	2.2
Takaishi et al. **[54]**	NMR	0	19	51	25	5	2.2
Feller et al. **[55]**	NMR	6	25	38	25	6	2.0
Kacem et al. **[23]**	Raman	2	24	59	12	3	1.9
Sampaio et al. **[77]**	MD and Raman	3	25	39	28	5	2.1

Kacem *et al.* [23] proposed the curve fit model for the high-wavenumber Raman spectra of the $PbO\text{-}SiO_2$ glass system by progressively varying the composition from pure silica up to 70 mol.% PbO. These authors have assumed seven Gaussian functions due to the Q^0, Q^1, Q^2, Q^3, Q^{4I}, and Q^{4II} and T_{2s} species. This model distinguishes the contribution of Q^4 into two different species,

Q^{4I} and Q^{4II}. Concerning the attributions, Q^{4I} corresponds to the large angle (or large fold rings) and Q^{4II} to small angle (or small fold rings) entities, the contribution of the former is dismissed for glasses with more than 30 mol.% PbO. In its turn, T_{2S} was assigned to the vibrational mode inside the silica tetrahedron, corresponding to two oxygens approaching the central Si atom and two oxygens moving away. For improving the spectral fit quality of glasses from 20 to 50 mol.% PbO, these authors introduce a T_{2b} band for which the area contribution is excluded in the Q^n normalization. In the case of the PS glass, Kacem's curve fit model delivers a high proportion of Q^2 to Q^3 species when contrasted to the other structural studies (Table 1.1).

By corroborating Raman spectroscopy and molecular dynamics results, Sampaio *et al.* [77] proposed a model to curve fit the high-wavenumber Raman envelope of PS glass into six Gaussian functions assigned to the vibrations of Q^0, Q^1, Q^2, Q^3, $Q^{3'}$, and Q^4 species. In particular, this model introduces the two distinct Q^3 species, Q^3 and $Q^{3'}$, then associated with a bimodal distribution displayed by the Pb-Si pair correlation function, presenting longer or shorter bridging distances between the NBO and the lead cations. By means of this extra specie of Q^3, Sampaio's curve fit model provides a good agreement with the Q^2 and Q^3 proportions determined by NMR at room temperature (Table 1.1), and with the Q^n distribution derived from molecular dynamics simulations at high temperatures comprising the glass, SCL, and melt states.

CHAPTER 2 – EXPERIMENTAL METHODS

2.1. Samples Syntheses

I. PS Glass Sample

$PbSiO_3$ (PS) glass was prepared by standard splat quench method in a 100 g batch made from ground SiO_2 (Vitrovita, Brazil) and Pb_3O_4 (Sigma-Aldrich, USA), further annealed close to the glass transition temperature (T_g) and slowly cooled to release residual stresses. The estimation of $T_g \approx$ 682 K was performed by differential scanning calorimetry (DSC) in a Netzsch 404 equipment at a heating rate of 10 K/min from room temperature to 1073 K, using Pt–Rh crucibles as reference (LaMaV, Brazil). Figure 2.1 illustrates the DSC curve for the PS glass marking the respective T_g and T_m temperatures, which are in good agreement with the literature [77, 113-118]. More details regarding the crystallization temperatures (T_c) are provided in Chapter 5.

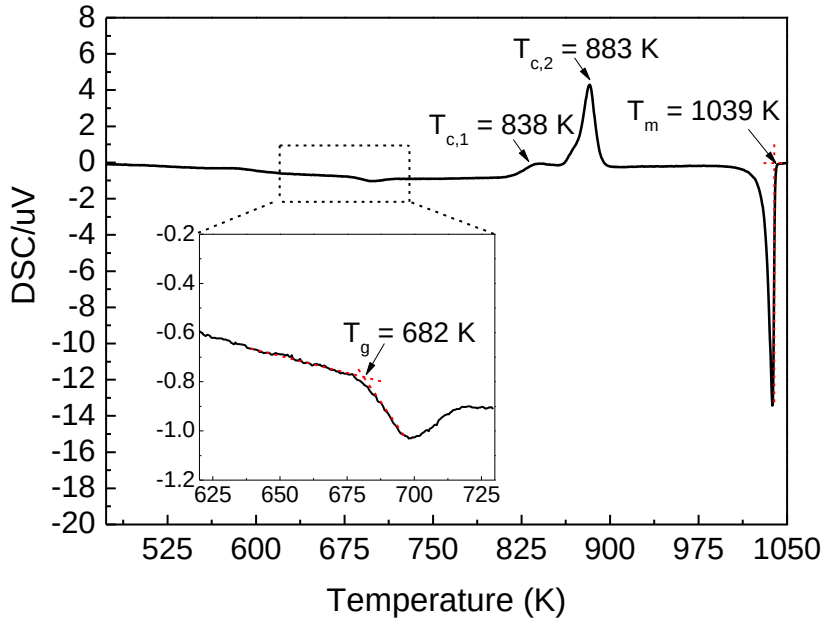

Figure 2.1.: DSC curve for the PS glass at a 10 K/min heating rate. Data kindly provided by Msc. Ricardo Lancelotti.

The chemical composition was evaluated by electron probe microanalysis (EPMA) on a JEOL JXA8230 5-WDS using a 15 nA current and 15 kV voltage on a 1 μm spot size at ten

different points. The sample had a homogeneous composition, averaging 49.7 mol.% SiO_2 and 50.3 mol.% PbO, with the estimated uncertainty to the first decimal place.

II. Cobalt-Doped PS Glass Samples

A set of cobalt-doped glasses in batches of 5 g each were prepared in partial substitution to the lead ($Co_xPb_{1-x}SiO_3$). In addition to the aforementioned reagents, CoO (Sigma-Aldrich, USA) was used. Under the same experimental conditions, T_g^{DSC} was found to decrease with the cobalt content down to 677 K for the highest doping concentration (not shown). The stoichiometries were evaluated similarly to the undoped PS glass, for which the average compositions and the related nomenclature herein applied are listed in Table 2.1. Trace contamination comprised metals such as Cr, Cu, Ni, and Fe, which together accounted for the remaining 0.2 mol.%.

Table 2.1: Chemical compositions of the Co-doped PS glass samples.

Nomenclature	CoO (mol.%)	PbO (mol.%)	SiO_2 (mol.%)
PSCo0.2	0.2	49.8	49.8
PSCo0.5	0.5	50.2	49.1
PSCo1.1	1.1	48.8	49.8
PSCo1.5	1.5	48.7	49.6
PSCo2.1	2.1	48.7	49.1
PSCo2.6	2.6	48.5	48.7

2.2. Raman Spectroscopy

I. Instrumental Description

Raman spectrometer setup comprises mainly a laser beam as a light source; a diffraction grating as a wavelength selector; a Charge Coupled Device radiation detector, and a computer where the signal is processed and read [87]. In a micro-Raman spectrometer, the monochromatic excitation light is focused on a probed sample through a microscope objective, the backscattered light is collected and filtered by a prechromator and interference filters to cut the Rayleigh scattering. The remaining light is diffracted by a diffraction grating and then collected on a Charge Coupled Device detector, this last cooled by the Peltier effect. In this thesis, measurements were obtained through the micro-Raman spectrometers LabRAM Aramis (ILM-France) or a LabRAM HR (ILM-France and GEOR-Brazil), equipments from Horiba Jobin Yvon.

LabRAM Aramis spectrometer is equipped with an edge filter, enabling the Stokes measurement from around 100 cm^{-1}. In the case of the LabRAM HR, a super-notch filter enables the Stokes measurements from ~10 cm^{-1}. The excitation light wavelengths used in this thesis

comprised 433 nm (blue), 532 nm (green), and 633 nm (red) laser sources. Diffraction gratings applied were 600, 1800, or 2400 slits/mm, based on the spectral resolution required.

Extreme condition Raman measurements were conducted independently under high pressure and high temperature, then achieved through different stages. Pressures up to 23 GPa were attained in a diamond anvil cell (DAC), addressed in detail in section 2.3. Temperature measurements up to 1000 K were performed in a Linkan TS1500 micro furnace. More details regarding the specific spectral acquisition conditions and the applied protocols are available in each chapter.

II. Spectral Analysis

Quantitative spectral analysis of the high-wavenumber spectral region ('Q^n envelope') was alternatively performed by the determination of the one-parameter barycenter or the multiple functions curve fit. The discussion below focuses on the glass spectra, even though the barycenter was also used to track the overall crystallization process (Chapter 5).

A. Barycenter

The barycenter (χ_b) was determined by integrating the Raman spectrum from 790 to 1200 cm^{-1}, the spectral region that corresponds to the vibrations of the different Q^n units, and subsequently estimating the wavenumber that separates the normalized integrated function and therefore the Q^n envelope into two parts of equal area, as schematically showed in Figure 2.1. This one-parameter is the geometric mean, which reflects the simultaneous evolution of the line shape and offset of the peak maximum. Similar analysis procedures has been applied in Raman spectroscopic studies of other glass compositions in order to characterize the evolution of distinct vibrational bands with pressure or temperature [119-121].

Noteworthy, due to the inherent integration process, the absolute barycenter value depends on the grating and excitation wavelength used during the spectral acquisition, a fact that correlates to the spectral resolution and the consequent number of points available for performing this mathematical operation.

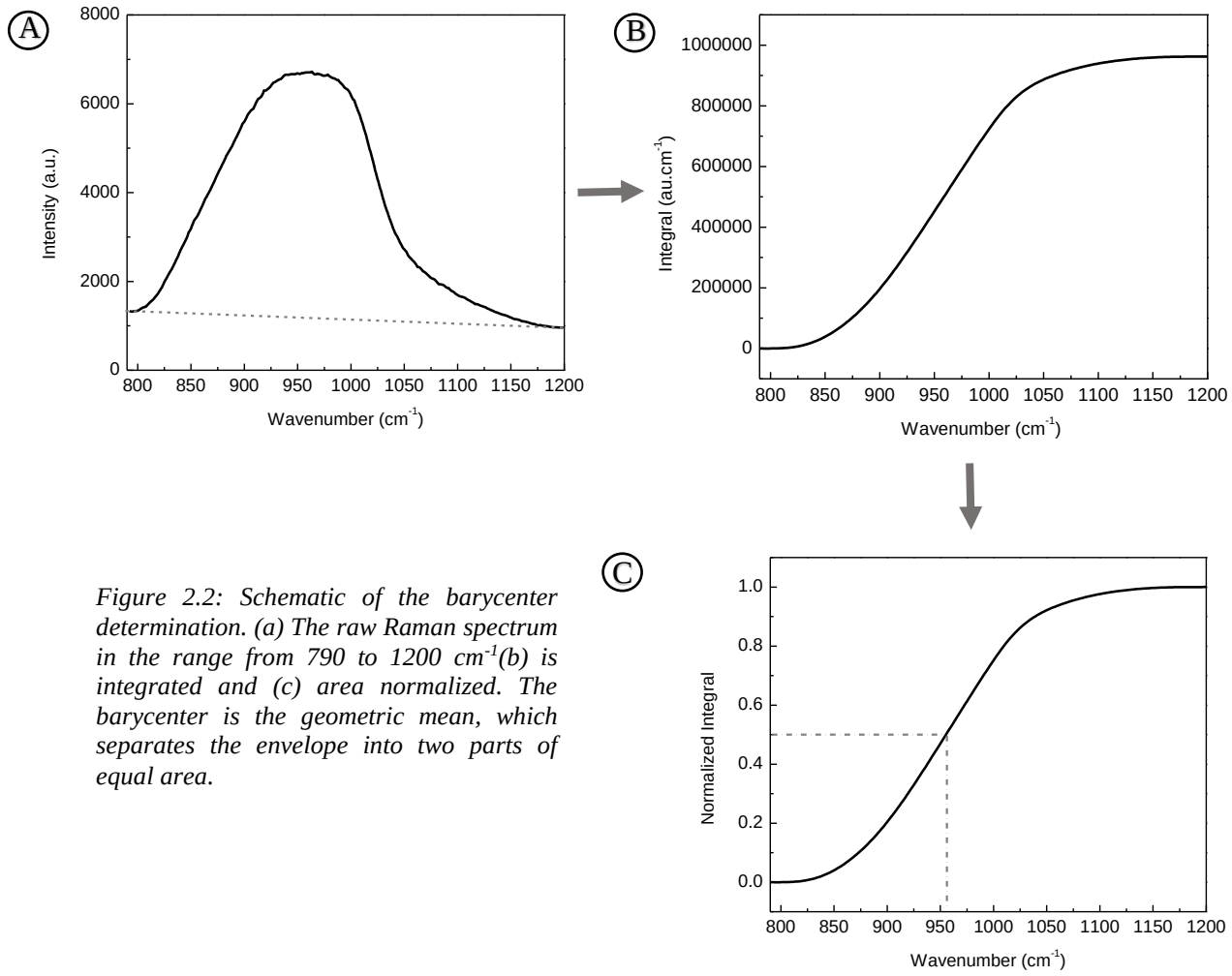

Figure 2.2: Schematic of the barycenter determination. (a) The raw Raman spectrum in the range from 790 to 1200 cm^{-1}(b) is integrated and (c) area normalized. The barycenter is the geometric mean, which separates the envelope into two parts of equal area.

B. Q^n Curve fit

Data were fit using the software Fityk (version 0.9.8) by applying the Nelder-Mead Simplex fitting algorithm. Raw data was baseline corrected with a cubic function fit by selecting the flat spectral region that precedes and follows the Q^n envelope range. Besides improving the overall fitting quality, such a baseline correction was reported to not affect the Q^n distribution of the PS glass [77].

In glasses, the curve fit of spectral broadbands without well-defined peaks such as the Q^n envelope is a model-dependent procedure, since the empirical analysis requires making *assumptions*. The Q^n evaluation is obtained by curve fitting a series of functions to model the distinct Q^n vibrational modes, where the number of fitted peaks and their shape might be physically justifiable. The final quantification of a given Q^n depends on the spectral relative intensity; peak width; peak position; and the area ratio of the individual function to the total set of functions.

Noteworthy, the number of fitted peaks in many glass systems is higher than the actual number of Q^n species [40].

Raman spectra of silicate glasses are classically curve-fit with Gaussian functions [122, 123]. Mysen *et al.*[124] assumed symmetric distribution and Gaussian line shapes. Preserving the assumption of function symmetry, Efimov *et al.* [123] argued on the physical use of Lorentzian functions and their linear combination, since their widths are associated with the phonon lifetime. In support of the Gaussian function applied in their studies, Rossano and Mysen [125] attributed such a line shape to the distribution of environments in the glass leading to a Gaussian distribution of Lorentzian functions. The mathematical character of the applied components has recovered the attention of the glass society recently, as approached in the investigations on alkali and alkaline earth silicates [126-128].

2.3. High-Pressure Experiments

For performing high-pressure experiments, an investigated sample is immersed in a pressure transmitting medium (PTM), which ideally distributes the exerted pressure homogeneously through space. At a given point, the stress is described by a tensor such as:

$$\overleftrightarrow{\sigma} = \begin{bmatrix} \sigma_{xx} & \sigma_{xy} & \sigma_{xz} \\ \sigma_{yx} & \sigma_{yy} & \sigma_{yz} \\ \sigma_{zx} & \sigma_{zy} & \sigma_{zz} \end{bmatrix} \quad (2.1)$$

Where σ_{ij} is the stress component oriented on the surface î directed upon ĵ. The diagonal components represent the normal stress, while the off-diagonal elements represent the shear stress [129].

The hydrostatic condition sought vastly for these experiments means simultaneously that there is no shear stress contribution and that the normal components show the same magnitude. In other words, the stress is directed toward the sample surface and is spatially the same. One can simply define the mean pressure $\bar{P}$ as the average of the three normal stress components:

$$\bar{P} = \frac{1}{3}[\sigma_{xx} + \sigma_{yy} + \sigma_{zz}] \quad (2.2)$$

Where the sum in the square brackets is the trace of the stress tensor, with $\sigma_{xx} = \sigma_{yy} = \sigma_{zz}$.
The hydrostatic mean pressure is a thermodynamic parameter, and the results obtained under such conditions are intrinsic material properties that can be compared with simulations [130].

Figure 2.2 illustrates different high-pressure apparatuses evidencing the compromise between the sample volumes and the maximum attained pressures. Once pressure is defined by the

force perpendicularly applied to the surface per unit area, the smaller the surface of application and the sample sizes, the higher the achieved pressures.

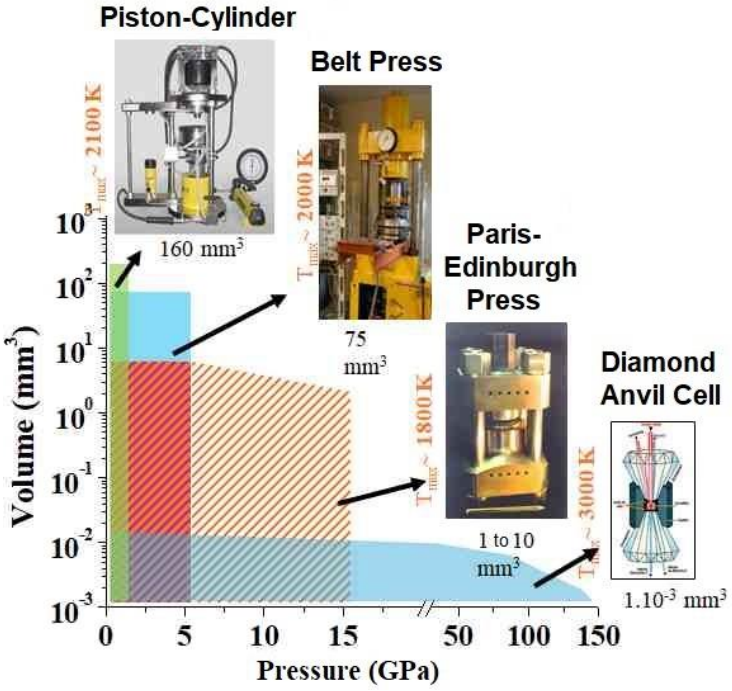

Figure 2.3.: Different high-pressure apparatuses evidencing its sample size requirements and maximal pressures. Illustration kindly provided by Dr. Alfonso San Miguel.

Optical experiments performed in Diamond Anvil Cell (DAC) rely on the diamond hardness and fair transparency to light in the visible spectral range, which enables *in-situ* characterizations in an extensive pressure range. The disadvantage comes from the sample size (~1.10^{-3} mm^3) which makes it impracticable to determine macroscopic properties (*e.g.*, density, refractive index, mechanical properties, *etc.*).

I. DAC Apparatus

A comprehensive review addressing DAC apparatuses is presented therein [131]. Conventional preparation of DACs involves initially indenting and drilling a metal gasket that will remain between the diamonds. Above one of the diamond faces, the gasket chamber is then loaded with (i) the probed sample; (ii) a PTM; and (iii) a pressure calibration sensor, as displayed in Figure 2.3. The other diamond closes hermetically the system.

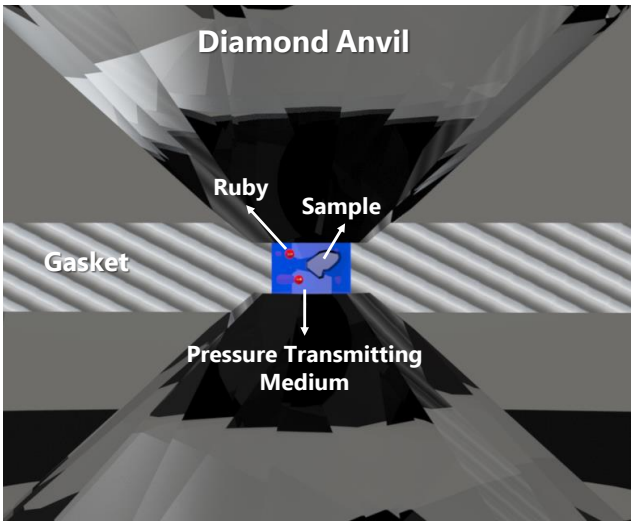

Figure 2.4.: Schematic of the DAC apparatus. Illustration kindly provided by MSc. Valentin Laurent.

As aforementioned described, PTM is the medium responsible for distributing the uniaxial force exerted by the diamonds through the volume, ideally in hydrostatic conditions. The comparison between the hydrostaticity of 11 different PTMs is presented therein [130]. A selected PTM may influence the experiment in two different ways. Firstly, the effect of its nonzero shear stress beyond its hydrostatic limit can anticipate glass densification [132]. Secondly, any eventual parasitic media signal can coincide with that of the probed sample. In the case of the widespread 4:1 methanol-ethanol alcohol solution, it presents characteristic Raman modes centered at room conditions on 882 and 1032 cm^{-1}, further discussed in the next section. These parasitic bands preclude an *in-situ* characterization of the high-wavenumber region of PS glass but can be applied in *ex-situ* measurements in the same spectral range since these alcohols evaporate when the DAC apparatus is opened.

In its turn, a pressure calibration sensor allows the determination of the accurate pressure in the DAC. Historically, the photoluminescence (PL) of ruby has been the classical pressure-calibrating sensor applied in these sorts of experiments, due to its intense signal and remarkably high pressure coefficient. In experiments where its application is not feasible, further alternatives have been sought over the years, relying mainly on PL properties of different materials [133, 134]. We have pursued the selection of new candidates to study *in-situ* the cobalt-doped PS glass, whose PL lies about the same spectral position as these alternatives (~700 nm). The loading of the DAC with these alternative pressure calibrants was applied solely in Chapter 7, but because of the interesting insights into the main constituents of DAC, it is discussed in detail below.

2.4. Pressure Calibrant Candidates

In this section, we discuss the classical ruby calibrant method, and some alternatives already present in a conventional DAC apparatus setup: the diamond and the PTM alcohol solution. We have further considered silicon, routinely available in Raman laboratories as the standard to calibrate the Raman wavenumbers at room conditions.

I. Ruby Luminescence Method

Since the early seventies, the PL property of ruby ($Al_2O_3:Cr^{3+}$) enables an accurate and powerful tool to calibrate the pressure in DAC apparatuses. Initially, the shift of the R lines in ruby (Figure 2.5) were constrained to X-ray diffraction data of salt and metal standards. Forman, Piermarini, and co-workers [135] were the first to report the linear shift of the R lines for pressures up to 2.2 GPa. In a succeeding work using NaCl as the standard, these authors showed that the R_1 linearity held up to 19.5 GPa, presenting an angular coefficient estimated as 7.53 cm^{-1} / GPa [136].

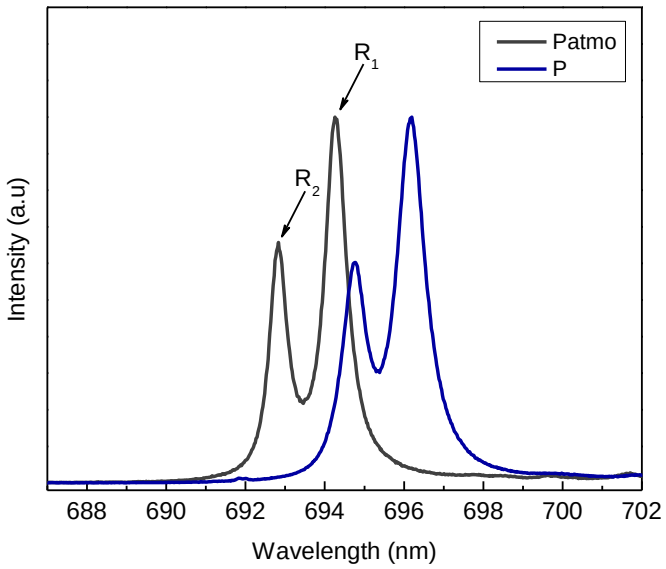

Figure 2.5.: Ruby luminescence spectra at atmospheric pressure (Patmo) and under high-pressure (P>Patmo) evidencing the R_1 and R_2 lines.

As the pressure reached in DACs gradually increased, further works reexamined the shift of the R_1 ruby line in a wider pressure range. Over the years, the works of Mao and co-workers were particularly relevant [137, 138]. In their first contribution, Mao *et al.* [137] extended the ruby scale calibration to 100 GPa, then determined by comparison with metal standards (Cu, Mo, Pd, and Ag), both immersed in a 4:1 methanol-ethanol as the PTM, obtaining:

$$P = \frac{A}{B}\left[\left(\frac{\lambda}{\lambda_0}\right)^B - 1\right] \text{ (GPa)} \quad (2.3)$$

Where λ is the measured peak wavelength of the ruby R_1 line, $\lambda_0 = 694.24$ nm is the zero-pressure value at 298 K, and A = 1904 and B = 5 are the obtained fitting parameters. From this calibration, a deviation from the linearity is negligible below 20 GPa, whereas a linear extrapolation would overestimate the pressure values under higher pressures [131]. A few years later, Mao *et al.* [138] repeated their ruby calibration in an argon media up to 80 GPa, using copper and silver standards, and determined for the Eq. (2.3) fit parameters of A = 1904 GPa and B = 7.665. For many years, this last calibration in quasi-hydrostatic conditions was the ruby pressure standard.

One of the most recent works was published by Chijioke *et al*. [139] considering pressures up to 150 GPa. These authors provided a detailed list of ruby pressure scales, analyzing their predecessors critically. For their calibration, they fitted two sets in the literature [140, 141], and their data, which was obtained in quasi-hydrostatic conditions applying hydrogen and helium, and constrained to metal standards requiring minor thermal corrections. Their fit parameters for the Eq.(2.3), were A = 1876 and B = 10.71 [139]. In 2020, an internationally accepted ruby gauge up to 150 GPa was established [142], accounting on the non-linear evolution of the R_1 ruby line according to:

$$P = 1870\left(\frac{\lambda}{\lambda_0}\right)\left[1 + 5.63\left(\frac{\lambda}{\lambda_0}\right)\right] \text{ (GPa)} \quad (2.4)$$

II. Diamond

Hanfland *et al*. [143] were the pioneers to propose the use of the first-order Raman mode of diamond (ν_0 =1333 cm^{-1}) as a pressure calibrant for experiments running in DACs. In loading with water as the PTM, these authors observed at the center of the diamond culet a linear shift up to 30 GPa with $\frac{\partial \nu}{\partial P} = 2.33 \pm 0.01 \text{ cm}^{-1}.\text{GPa}^{-1}$. Because of their relatively low pressure coefficient to previous Raman studies performed to 2.5 GPa [144, 145], they repeated their calibration up to 40 GPa, then applying xenon as the PTM. They updated the diamond pressure coefficient to $\frac{\partial \nu}{\partial P} = 2.90 \pm 0.05 \text{ cm}^{-1}.\text{GPa}^{-1}$ [146]

A comparable pressure coefficient was contemporary reported by Boppart *et al.* [147], who carried their calibration up to 30 GPa by placing diamond samples into the DAC in loadings with hydrogen, argon, and xenon. These authors reported a pressure coefficient of $\frac{\partial \nu}{\partial P} =$

$2.87 \pm 0.10\ \mathrm{cm^{-1}}.\mathrm{GPa^{-1}}$, arguing that diamond plates do not show wavenumber dependence with the probed position in contrast to the diamond composing the DAC. Tardieu *et al.* [148] went one step further, analyzing at simultaneous high P–T conditions up to 15 GPa and 673 K, the shift of the first-order Raman mode of diamond samples immersed in a 4:1 methanol-ethanol PTM. These authors found decoupled effects of pressure and temperature on the phonon evolution, reporting a relatively low pressure coefficient in contrast to their predecessors $\left(\frac{\partial \nu}{\partial \mathrm{P}} = 2.64 \pm 0.10\ \mathrm{cm^{-1}}.\mathrm{GPa^{-1}}\right)$.

Foreseeing the diamond as the calibrant sensor under pressures where the R_1 ruby calibration no longer applies, recent studies extended the pressure gauge obtaining non-linear pressure coefficients of the diamond first-order Raman mode in this range [149-155].

III. Methanol-Ethanol Solution

A. Literature Review

Either methanol or ethanol alcohols crystallize at low pressures [156], whereas the 4:1 mixture of these alcohols is reported to vitrify at 10.5±0.5 GPa, presenting hydrostaticity up to this pressure and quasi-hydrostaticity above [130]. Previous studies reported in the literature have described the pressure evolution of this alcohol solution in the pressure range up to 6 GPa [157, 158], despite its potential to be applied as a PTM and pressure calibrant at higher pressure ranges.

Lemos *et al.* [157] observed the pressure evolution of the first-order Raman modes centered at room conditions on 882 $\mathrm{cm^{-1}}$, 1032 $\mathrm{cm^{-1}}$, and 1454 $\mathrm{cm^{-1}}$. These peaks are respectively attributed to the stretching modes of C-C in methanol; C-O in ethanol and asymmetric bending of CH_3 in methanol. A linear evolution was reported for the peaks initially at 882 $\mathrm{cm^{-1}}$ $\left(\frac{\partial \nu}{\partial \mathrm{P}} = 4.3\ cm^{-1}/GPa\right)$ and 1454 $\mathrm{cm^{-1}}$ $\left(\frac{\partial \nu}{\partial \mathrm{P}} = 5.5\ cm^{-1}/GPa\right)$, whereas the peak at 1032 $\mathrm{cm^{-1}}$ was fitted as a quadratic function. Singh *et al.* [158] reexamined the pressure evolution of this alcohol solution focusing on the spectral range between 1400 and 1600 $\mathrm{cm^{-1}}$. For the Raman mode initially centered on 1454 $\mathrm{cm^{-1}}$, these authors reported a pressure coefficient lower than their predecessor $\left(\frac{\partial \nu}{\partial \mathrm{P}} = 4.4 \pm 0.7\ \mathrm{cm^{-1}/GPa}\right)$.

B. Experiment

For extending the pressure range for the 4:1 methanol-ethanol calibration, we charged the DAC with multiple ruby chips and the aforementioned alcohol mixture. The ruby luminescence method enabled the pressure determination *in-situ*, then calibrated by Mao and Bell adjust [138]. Figure 2.6 displays the *in-situ* Raman spectra obtained up to 19±1 GPa.

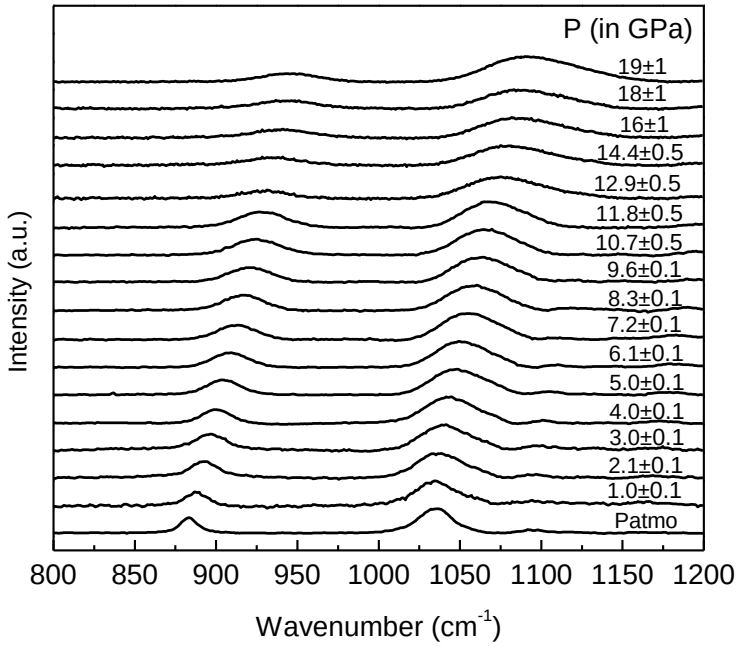

Figure 2.6: In-situ Raman spectra of the 4:1 methanol ethanol solution as a function of the pressure (P).

The spectra were baseline corrected and curve fit into four Gaussian functions (Figure 2.7a and Figure 2.7b), which among Gaussian, Lorentzian, and Pseudo-Voight functions provided the best fit over the full pressure range. At room conditions, the vibrational modes in the high-wavenumber region are centered on 883, 1032, 1095, and 1158 cm^{-1} and respectively attributed to the C-C stretching in ethanol; C-O stretching in methanol, and to two CH_3 rocking modes, from the contribution of both, methanol and ethanol [156]. For calibration purposes, we focused the analyses on the center position evolution of the two more intense peaks (Figure 2.5c). The red and green lines show the Lemos *et al.* [157] fit, which presents a good agreement with our experimental data up to 6 GPa.

These two more intense peaks were fitted by:

$$\nu = 883 + 4.5\,P - 0.07\,P^2\ (cm^{-1}) \qquad (2.5)$$

Due to the C-C stretching peak in ethanol and:

$$\nu = 1032 + 3.6\,P - 0.04\,P^2\ (cm^{-1}) \qquad (2.6)$$

Due to the C-O stretching peak in methanol, with the pressure expressed in GPa.

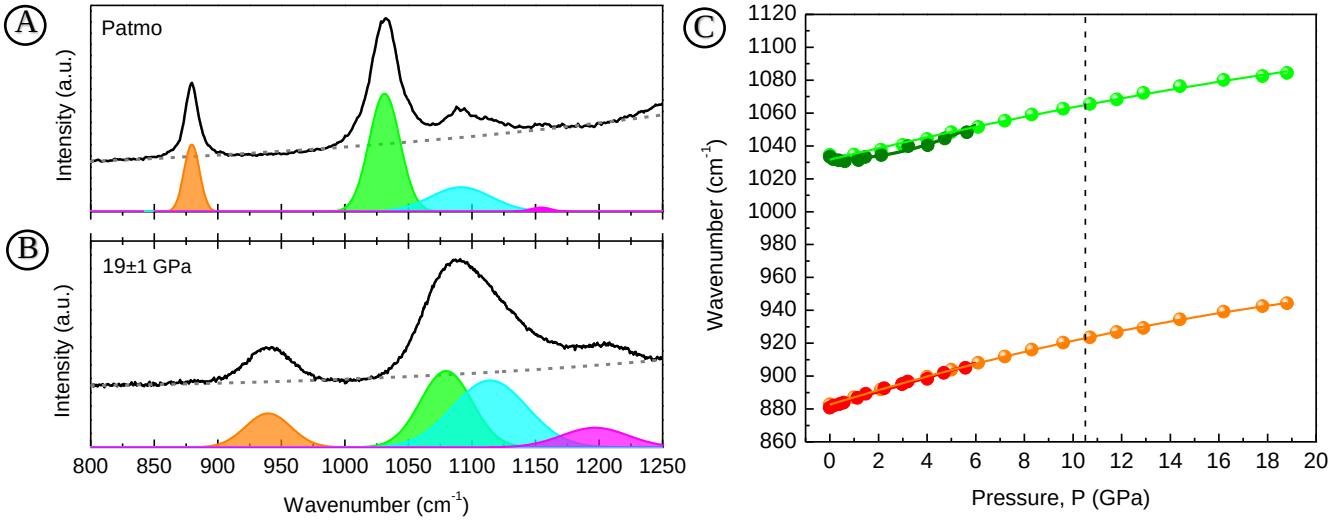

Figure 2.7: Raman spectra and Gaussian curve fit of the 4:1 methanol ethanol at (a) atmospheric pressure (Patmo) and (b) 19±1 GPa; (c) center position evolution for the C-O and C-C stretching modes as a function of the pressure (P). The dashed line indicates the hydrostatic limit of the alcohol solution.

IV. Silicon

Besides the well-established ruby luminescence method [136], Piermarini *et al.* worked on the pressure calibration by other luminescent means [133] and semiconductors such as silicon and GaP [159]. Disposing silicon monocrystals in a DAC, along with ruby chips and a 4-1 methanol-ethanol solution as the PTM, they observed *in-situ* the pressure evolution of the first-order Raman modes of Si up to 12.5 GPa, which shifted without change in the spectral line shape following [159]:

$$\nu = 519.5 + 5.2\,P - 0.07\,P^2\ (cm^{-1}) \qquad (2.7)$$

Where P is the pressure expressed in GPa, and the uncertainties are in the last decimal place.

At 12.5 GPa, these authors described a permanent first-order phase irreversible transition into a highly opaque phase, evidenced by an evident decrease in the Raman intensity. Two decades later, the same investigation was repeated by Mernagh *et al. [160]*, who found reproducible results within the uncertainties but the phase transition at around 14 GPa.

V. Pressure Coefficient Comparison

According to Barnett *et al.* [133], some relevant criteria for a pressure sensor candidate comprise: the position of the peak in contrast to the probed sample spectrum; low or high

continuum background; spectral intensity; pressure coefficient; temperature coefficient; spectral linewidth, etc.

Among these criteria, we will focus primarily on the pressure coefficient at room temperature, which plays an important role in the pressure calibration sensibility. Figure 2.8 illustrates the pressure coefficient for ruby, diamond, silicon, and the two more intense peaks in 4:1 methanol-ethanol solution as a function of the pressure up to 19 GPa. In this pressure range, we can treat as linear either the ruby [136] and diamond [146] shift, whereas the other coefficients were derived from Eq. (2.5) to (2.7). Notably, we observe that ruby presents the highest pressure coefficient, whereas the efficiency of the other candidates for pressure calibrants depends on the pressure range:

A. Up to 12.5 ~14 GPa: silicon presents as the best alternative among the candidates, displaying not only the highest pressure-coefficient but also a single and intense first-order Raman peak whose shape remains about the same up to the pressure-induced phase transition.

B. Above 12.5 ~ 14 GPa: the resulting silicon high-pressure phase does not present any Raman-active vibration, whereas diamond presents the highest pressure coefficients among the candidates, being a suitable choice as a pressure calibrant in this range.

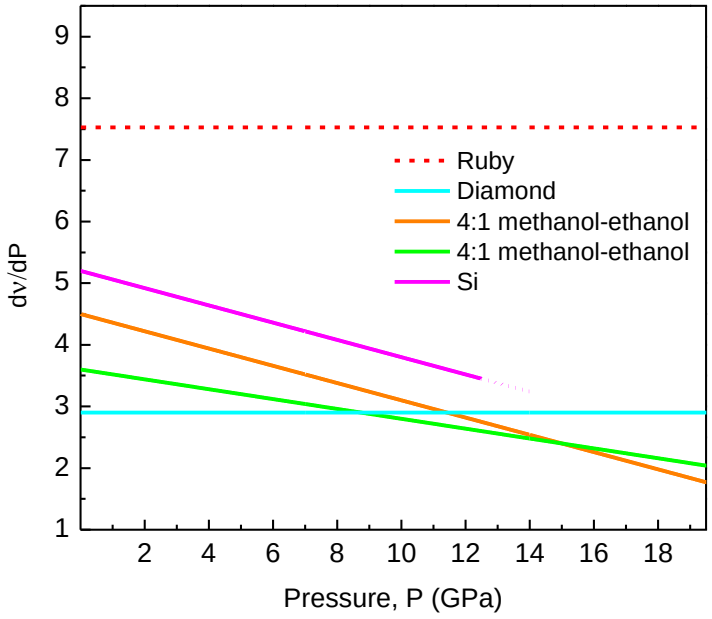

Figure 2.8: Pressure coefficient for ruby, diamond, the two more intense peaks in 4:1 methanol-ethanol solution, and silicon as a function of the pressure (P).

CHAPTER 3 – EX-SITU MEASUREMENTS: THE DENSIFIED GLASS STRUCTURE

3.1. Introduction

The effect of high pressure on the glasses manifests in enhancing their density, refractive index, and mechanic properties. Microscopically, may modify the SRO and MRO in the glass structure, evidencing changes to coordination number; cation-oxygen bond lengths and angles; network polymerization; and ring statistics

To the best of our knowledge, previous to the works related to this thesis, the only high-pressure study of the $PbO\text{-}SiO_2$ glass was conducted by Yoshimoto *et al.* [161] focusing on the mechanical properties. They indicated an increase in the hardness and Young's modulus driven by the hot-densification of $PbO\text{-}SiO_2$ glasses with compositions ranging from 33 to 67 mol.% PbO. According to these authors, pressure treatment under 6 GPa and $0.75*T_g$ resulted in network depolymerization, as probed by infrared spectroscopy. Densification rates decreased monotonically with PbO content, whereas Young's modulus and hardness were reported to display a minimum at the metasilicate composition at a 2.6% densification ratio. Despite the great picture of the general pressure effect as a function of the glass composition, this study underexplored the variable pressure at a given glass composition.

We present here our analysis addressing the structure of the densified lead silicate glass as recently published in our article entitled "*High-Pressure Plastic Deformation of Lead Metasilicate Glass Accessed by Raman Spectroscopy: Insights into the Q^n distribution*" *[162]*. In this study, a set of glasses submitted to different maximum pressures (Pmax) in a DAC was probed *ex-situ* by Raman spectroscopy. Such an investigation enabled to determine the elastic deformation limit and permanent structural modifications regarding the Q^n distribution. In this chapter, we advance one step further by inspecting the mathematical character of the components applied to curve fit the Si-O stretching region of the Raman spectra. Albeit the broadband shape, we notice a low degree of Gaussian-Lorentzian (G-L) mixing to $Q^{3'}$ and essentially the same Q^n evolution trend as reported in Ref. [162].

3.2. Experimental Procedures

Stainless steel gaskets were indented and drilled, resulting in chambers with a ~50 μm height and 200 μm diameter. In each run, a Chervin-type DAC was loaded with PS samples, ruby

chips as a pressure sensor, and a 4:1 methanol-ethanol mixture as the PTM. The R_1 ruby fluorescence line of Cr^{3+} excited with a 633 nm laser enabled the pressure determination *in-situ* [138]. The pressure was incremented up to a maximum pressure (Pmax) in a compression-decompression cycle. Eight distinct PS glass pieces were compressed to the following Pmax: 4.1 GPa; 5.7 GPa; 9.9 GPa; 12.6 GPa; 14.3 GPa; 15.5 GPa; 20 GPa and 23 GPa. The pressure uncertainties inside the DAC were estimated to be ±0.1 GPa within the hydrostatic pressure region, ±0.5 GPa up to 16 GPa, and ±1 GPa above 16 GPa. Raman spectra were acquired at room conditions after the pressure treatment.

Raman measurements were taken using a LabRAM Aramis micro-Raman spectrometer (ILM, France) from Horiba Jobin Yvon with a 473 nm laser wavelength as an excitation source. The Raman spectra were collected *ex-situ* for each of the densified PS glass samples using the 2400 slits/mm grating between 600 and 1300 cm^{-1}. Each spectrum is an average of five measurements of 300 seconds of accumulation time. Quantitative analyses were carried out considering the high-wavenumber region of the Raman spectra, performed independently by the barycenter determination or the Q^n curve fit. In the second section, the Q^n analysis was performed with Gaussian functions by systematically adjusting or holding constant the peak centers and width, as presented therein [162]. In the third section, G-L mixing was allowed and the function parameters were let to vary.

3.3. Results and Discussions

Figure 3.1 shows the high-wavenumber region of the Raman spectra of densified PS glasses. This spectral region is assigned to the symmetric Si-O stretching vibrations [77]. The spectra show a broad envelope, which shifts to lower wavenumbers with increasing Pmax. Similar results using infrared spectroscopy were reported on 2.6% densified PS glasses released from 6 GPa and ~500 K [161].

The discussion is divided into four sections: In the first, the modifications on the high-wavenumber envelope are described by the on-parameter barycenter (χ_b), providing an estimation of the elastic and saturation limits. The second part describes the curve fit modeling of the Q^n species with multiple Gaussian functions, systematically adjusting or holding constant the peak centers and widths from Sampaio's model [77]. In the third section, the curve fit procedure is repeated relaxing the Gaussian assumption by testing Pseudo-Voigt functions and hence allowing

the G-L character to vary. Finally, we present the structural modifications manifesting by network depolymerization, with an increase in the NBO proportion, as derived by the ensemble of curve fit procedures.

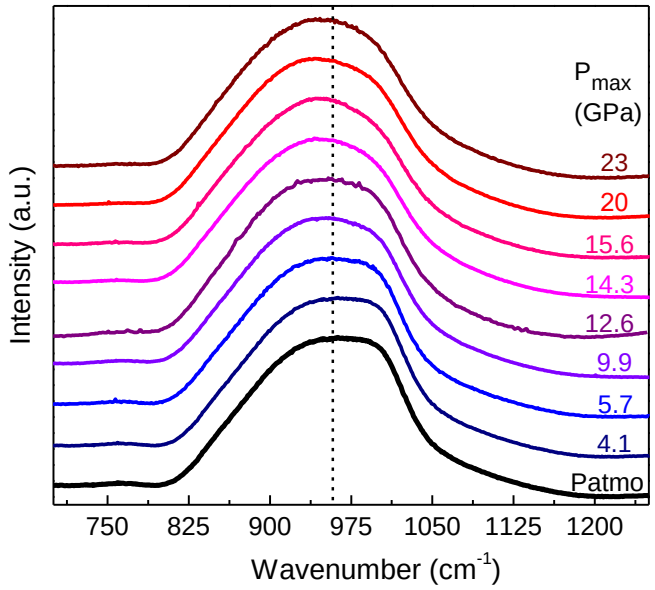

Figure 3.1: High-wavenumber Raman spectra of permanently densified PS samples. The dashed line marks the barycenter at atmospheric pressure. Adapted from Pena et al.,2021 [162].

I. Barycenter evolution: Elastic and Plastic Limits

Initially, we analyze the evolution of the high-wavenumber Raman envelope by determining their barycenter (χ_b). This one-parameter unveils three important trends for the densified PS samples:

(i) For uncompressed PS glass: χ_b remains invariant for the sample recovered up to ~4 GPa;

(ii) Above 4 GPa: the compression induces a progressive decrease in χ_b

(iii) Around 20 GPa: the shift in χ_b stops.

In the range of Pmax between 4 and 20 GPa, the χ_b shifts toward lower wavenumbers along with a subtle change in the envelope shape is an indication of depolymerization as the more polymerized Q^n species would shift χ_b to the higher wavenumbers [23, 77]. Such a proposition will be verified in the next sections.

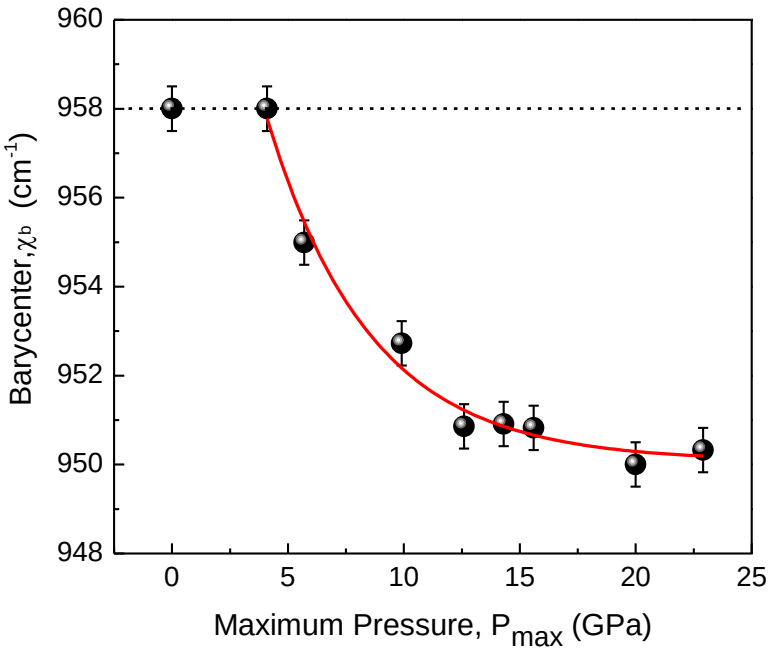

Figure 3.2: Barycenter of the high-wavenumber Raman region as a function of the maximum pressure (Pmax). An exponential decay function (red line) fits the experimental points (black circles), while a horizontal line marks the uncompressed value. Adapted from Pena et al.,2021 [162].

We define two pressure limits hereinafter referred to as elastic and saturation limits. According to the sensibility of the applied probe, the elastic limit corresponds to the maximum pressure below which the system can recover its initial state once returned to ambient conditions. Above the elastic limit, irreversible structural modifications and permanent densification occur up to Pmax where higher compression loadings at room conditions do not induce further permanent structural changes on the densified glass, marking then the saturation limit. The χ_b behavior indicates that the elastic limit of the lead metasilicate glass is about 4 GPa, whereas the saturation limit is around 20 GPa (Figure 3.2). Brillouin spectroscopy corroborates these limits as reported therein [163]. We highlight the potential of spectroscopic means in determining the elastic limit either by exploring pressure-sensitive properties and/or by SRO and MRO structural description.

The elastic limit of PS glass is low when compared to vitreous silica and other silicate glasses. Regarding vitreous silica, its elastic limit is estimated at around ~9 GPa, at room temperature and under hydrostatic conditions [164-170]. Above 9 GPa, the retrieved glass shows permanent densification [165], with a densification rate that varies gradually with Pmax, reaching up to 21% at 25 GPa, where it saturates [164-166, 168-170]. In soda-lime silicate glass, containing SiO_2 (72 mol.%), Na_2O (15 mol.%), and CaO (8 mol.%), the elastic limit lies around 7 GPa as

above this pressure, an increase of Q^2 at the expense of Q^3 tetrahedra has been observed [171]. $Li_2Si_2O_5$ glass also presents a comparable elastic limit, once drastic changes in the radial distribution function were observed for samples cold densified at 7.7 GPa [172]. Besides, pressure-induced modification of the Q^n distribution was also inferred from XPS measurements [173]. Under hydrostatic pressure, a glass composed of SiO_2 (80 wt.%), CaO (6 wt.%), MgO (5 wt.%), and Na_2O (5 wt.%) shows irreversible compaction beyond 8 GPa [174]. In a nominal $Mg_3Al_2Si_3O_{12}$ glass, the elastic limit was determined to be 6 GPa. Above this pressure, the Al coordination number increases, whereas the presence of highly coordinated Si species is negligible [175].

The compaction mechanism of vitreous silica involves a narrowing of the inter-tetrahedral angle in the elastic regime [166, 167, 170], in such a way that the SRO remains preserved, without significant changes in the Si-O distances and tetrahedral O-Si-O angles [167]. Meanwhile, as the pressure increases into the plastic regime, the coordination is reported to gradually change, from ^{IV}Si to ^{V}Si, and then to ^{VI}Si [167, 170, 176-179]. The densified vitreous silica recovers its SRO original features (^{IV}Si coordination, tetrahedral O-Si-O angle distribution [167]), but presents modification in MRO, with a decrease in the Si-O-Si angle distribution [180], which brings the Si-Si nearest neighbors closer to each other by decreasing the void space. In multicomponent silicate glasses, the permanent structural modifications due to high pressure affect the SRO by partially irreversible ^{V}Si and ^{VI}Si (and related modifier cation) coordination, affecting the M-O bond distance and inter-polyhedral angles, further modifying the Q^n distribution population [120, 171, 175, 181-185].

In contrast to vitreous silica, the PS glass exhibits a more compact and depolymerized structure. Kohara *et al.* [64] estimated that the total volume occupied by the voids in vitreous silica is 31.9%, while in PS glasses it amounts to 11.3%. In fact, Yoshimoto *et al.* [161] observed a decrease in the densification rate with the increasing PbO content at fixed compression conditions (6 GPa and $0.75*T_g$). The authors argued that this behavior is linked to the difficulty in accommodating large Pb^{2+} ions into the atomic scale voids within the silica glass network. This argument is consistent with the decrease in the inter-tetrahedral (Si-O-Si) angle playing a role in the densification mechanism, and the progressive decrease in the elastic limit at higher lead contents, as observed from vitreous silica to PS glass. To our knowledge, PS glass shows the lowest probed elastic limit in the literature, likely due to its dense packing and low void space.

The PS glass densification mechanisms are investigated in detail in Chapter 4. We anticipate that its correlation to the pressure-induced mechanisms occurring in vitreous silica is not straightforward. Noteworthy, vitreous silica presents ideally a completely polymerized, Q^4 structure, whereas the PS structure contains mostly Q^2 tetrahedra, with a great number of NBOs. Further complexity comes from the addition of lead cations, which in this composition is indicated to already present a sub-network, such that some lead cations act as modifiers while a small portion might play the role of network formers.

II. Q^n Curve Fit: The Gaussian Line Shape

In this section, we apply the curve fit model developed by Sampaio *et al.* [77]. This model was structurally consistent with molecular dynamics simulations and fits the high-wavenumber Raman envelope using six Gaussian components corresponding to Q^0, Q^1, Q^2, Q^3, $Q^{3'}$ and Q^4 contributions (Figure 3.4a). Given the new developments addressing the Q^n line shapes, the assumption of Gaussian functions could be attributed either to the high lead content or to the broader Si-O-Si angle distribution of this glass [77, 80]. For quantifying the Q^n species as a function of the Pmax, we further assumed no new peaks should be added as none are observed in the spectra and that the relative cross-sections for the Raman scattering do not change for the compressed samples. The cross-section is associated with the modulation magnitude of the electronic polarizability, and hence the perceived intensity of vibration. These assumptions are more easily enforced, whether the fundamental SiO_4 tetrahedral geometry is preserved after releasing the high-pressure [186]. Except for the Gaussian lineshape constraint, the ensemble of assumptions also holds for the next section where the G-L mixing will be allowed.

Table 3.1: Center position and half width at half maximum (HWHM) parameters for the curve fit of the high-wavenumber Raman spectra of PS glasses at room temperature. Adapted from Sampaio et al.,2018 [77].

	Center Position (cm^{-1})	**HWHM (cm^{-1})**
Q^0	847	26.0
Q^1	897	36.5
Q^2	955	39.0
Q^3	1001	26.5
$Q^{3'}$	1043	39.5
Q^4	1103	51.5

Gaussian parameters determined by Sampaio *et al.* [77] at room temperature are presented in Table 3.1. For each of the analyses, this set is used as initial values, holding the center position and half width at half maximum (HWHM) either as a constant or as a variable. Where left variable,

the variation of the peak center was constrained to $\Delta\nu = \pm 2$ cm^{-1}, and the ΔHWHM was constrained to ±0.1 cm^{-1}. These parameters may affect the area under a given Gaussian component, directly as the width may vary, or indirectly as the center position varies, once the spectral intensity is a function of the wavenumber. For clarity, each fitting procedure is listed in Table 3.2, where, for example, the 'P1' procedure uses constant parameters, whereas procedure 'P4' allowed both parameters to vary.

Table 3.2: Distinct procedures applied for performing the Q^n curve fit holding the center position and half width at half maximum (FWHM) either as a constant or as a variable. Retrieved from Pena et al.,2021[162].

	Center Position	**HWHM**
P1	Constant	Constant
P2	Variable	Constant
P3	Constant	Variable
P4	Variable	Variable

Figure 3.3 illustrates the contribution of each of the altered Gaussian parameters over the total Q^n quantification. We observe unsatisfactory results for the procedure "P3", where only the width was let to vary to fit the pressure-induced data, which naturally presents some center-shift, as pictures the barycenter position that displaces up to ~ 8 cm^{-1}. Comparing the outcomes of each procedure, we note that the P2 procedure shows deviations in the estimation of Q^4, whereas the P3 procedure underestimates the Q^2 population, and delivers worse agreement with the Q^1 and Q^0 population. The P1 and P4 procedures display the same trends, where both the Q^0 and Q^1 populations increase slightly, whereas Q^4 decreases modestly and Q^2 remains about the same still configuring the dominant structural unit. More interestingly, as the Pmax increases, the $Q^{3'}$ is favored over the Q^3 units. Due to their link with the Pb-Si pair correlation function, the P1 and P4 results suggest that pressure brings Pb closer to Si by converting part of the Q^3 to $Q^{3'}$ units, while Q^3_{tot} decreases.

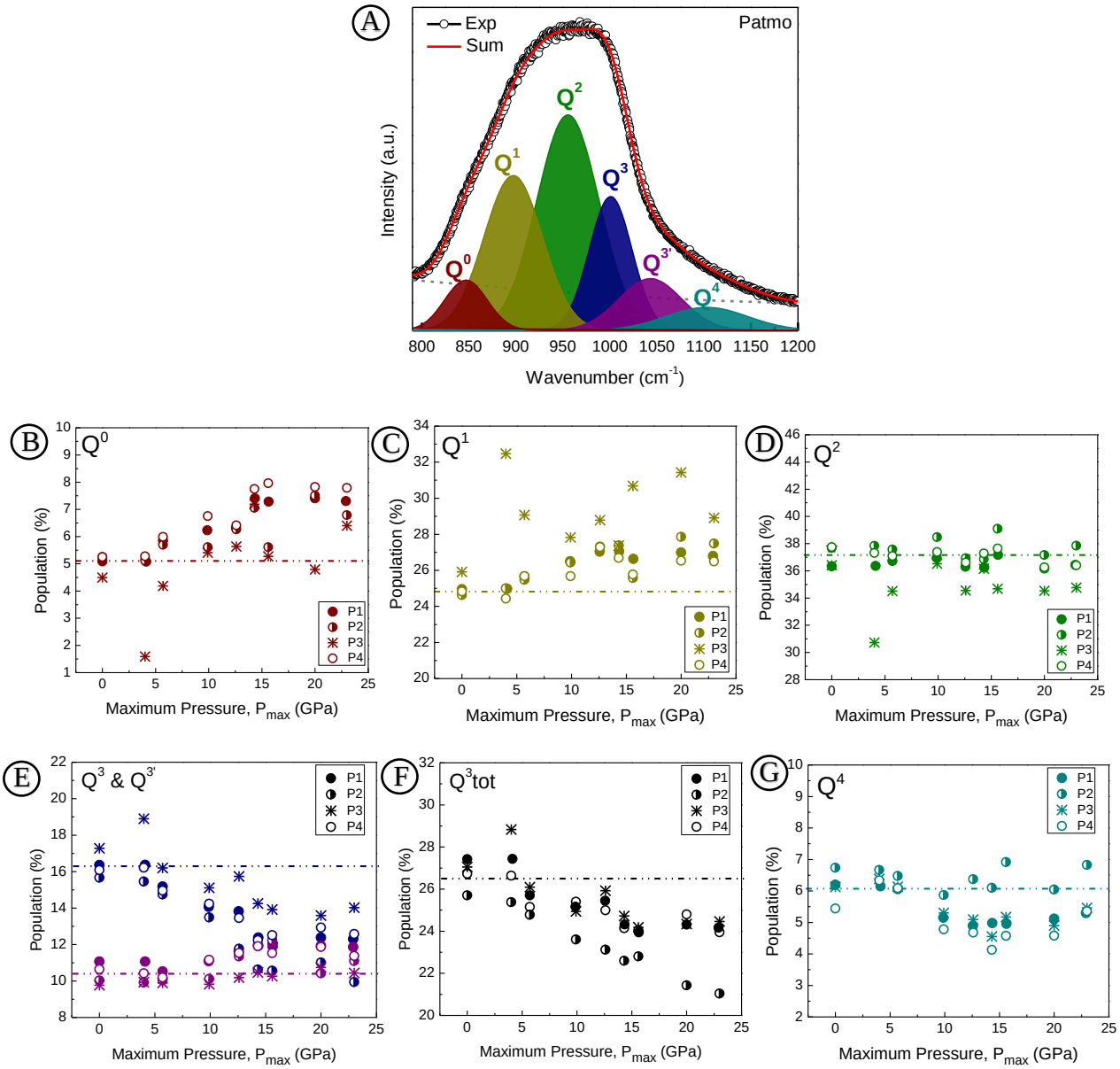

Figure 3.3: (a) Q^n population curve fit of the uncompressed PS glass (Patmo) and the evolution of (b) Q^0; (c) Q^1; (d) Q^2;(e) Q^3 and $Q^{3'}$; (f) Q^3tot and (g) Q^4 as a function of the maximum pressure (Pmax) obtained using the four distinct procedures (Table 2). The horizontal lines mark the population average for each Q^n at Patmo. Uncertainty in the Q^n population evaluation is estimated as ±1% (not shown). Adapted from Pena et al., 2021 [162].

III. Q^n Curve Fit: The Gaussian-Lorentzian Line Shape

Since 2018, there are new developments in the literature concerning the curve fit of the Si-O stretching region into multiple components, either applying Voigt [126] or Pseudo-Voigt functions [127, 128]. These studies [126-128] consider the G-L mixing nature of Q^n bands, covering a large range of alkaline-earth glasses with different Li, Na, K, Rb, Cs, or K content. According to Ref. [126], a factor influencing the Lorentzian character and the component function

width could be the variation in the O-Si-O angles. Once the O-Si-O angle closure is an important mechanism leading to the glass densification, we re-evaluated our entire data using two new fit procedures, denoted below as P5 and P6.

In the wavenumber domain, the aforementioned mixing occurs mathematically in different ways, represented in the Voigt function as a convolution (multiplication), whereas in Pseudo-Voigt functions is due to a linear combination (sum) of these characters. We carried on analyses with the latter function, as the linear combination leads to a more physical comprehension of the G-L mixing of the functions, providing an easy criterion to extend Sampaio's fit model [77], and compare the set of parameters, as well as their outcomes. The Gaussian, Lorentzian, and Pseudo-Voigt functions are in Fityk built-in function form respectively as:

$$y(height, center, hwhm) = height.\, exp\left[-\ln(2)\left(\frac{x-center}{hwhm}\right)^2\right] \tag{3.1}$$

$$y(height, center, hwhm) = \frac{height}{1+\left(\frac{x-center}{hwhm}\right)^2} \tag{3.2}$$

$$y(height, center, hwhm, shape) = height\left\{(1-shape).\, exp\left[-\ln(2)\left(\frac{x-center}{hwhm}\right)^2\right] + \frac{shape}{1+\left(\frac{x-center}{hwhm}\right)^2}\right\} \tag{3.3}$$

For Eq. (3.3), $shape = 0$ recovers the Gaussian and $shape = 1$ the Lorentzian characters. Any value between these limits indicates a linear combination of these functions to the Pseudo-Voigt profile. Note that the procedures performed previously with a Gaussian function given by Eq.(3.1) are mathematically equivalent to allowing the center and the width to vary in Eq. (3.3), holding constant the $shape = 0$.

Proceeding with P5, we relax the Gaussian character assumption for the Q^n (n=1-3') components. Noteworthy, Q^4 is constrained as a Gaussian function even in these studies allowing the G-L mixing [126-128]. In this turn, the center position, width, and function shape were allowed to vary simultaneously. The constraints were settled as $\Delta\nu = \pm 2$ cm^{-1} for the center position, and ΔHWHM = ± 2 cm^{-1} for the width; the initial shape was set as zero, with a Δ Shape in the [0,1] interval. Different from the four procedures applied in the previous section, here the ΔHWHM constraints to all the components were more relaxed because the Gaussian linewidths are characteristically wider than those reported therein [126-128]. To the best of our knowledge, the open-source Fityk software does not allow restrictions to the final parameter that is left to vary.

Hence, we obtained small negative values to the shape of some Q^n units, which definitively have *no* physical meaning, as highlighted in the shaded forbidden region in Figure 3.4.

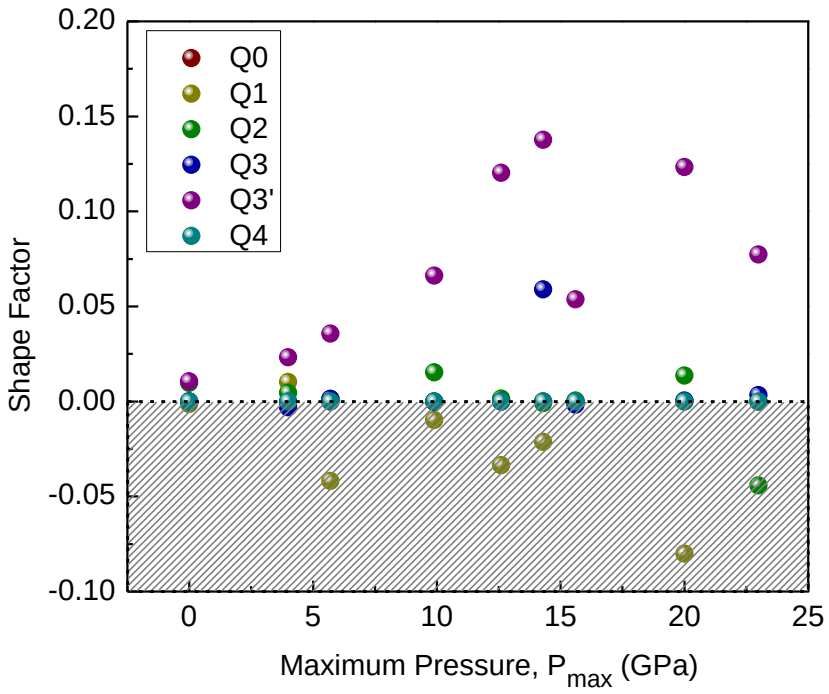

Figure 3.4: Shape Factor to the Q^n unities as a function of the maximum pressure (Pmax) obtained by the P5 procedure.

Since center position, HWHM, and shape parameters were altogether left to vary in the P5 procedure, and the outcome values for shape were not physically reasonable, we were forced to consider further constraints. Among the Q^ns, we observed that the $Q^{3'}$ mode presents the most evidence for G-L mixing, albeit to a low degree, in agreement with the conclusion outlined in Ref.[126]: *"The Lorentzian character of the silicate peaks decreases with a decrease in Q^n with n = 3 > 2 > 1"*. However, it would not yet explain whether there is mixing to $Q^{3'}$ nor why it would not apply to the Q^3 species. We repeated the curve fit through the P6 procedure, assuming $Q^{3'}$ as the only component which could show mixing. This time, the other components were set as Gaussian functions while $Q^{3'}$ was set as a Pseudo-Voigt function with an initial shape of 0.2, further considering $\Delta\nu = \pm 2$ cm^{-1} for the center position, ΔHWHM $= \pm 2$ cm^{-1} for the width, and a Δ shape in the [0,1] interval.

Figure 3.5 illustrates the estimated shape parameters and the Q^n population, contrasting the results obtained with P4 and P6 procedures. Noteworthy, even relaxing the Gaussian assumption we observe essentially the same evolution trend detailed in the previous section, and a shape factor

averaging 0.15. The G-L mixing is notably low and means that the full set of Q^n components in lead metasilicate glass is likely to be Gaussian, as constrained by Sampaio *et al*.[77]. Such outcomes provide more confidence for the multicomponent treatment of densified PS glass, and also for curve fitting the *in-situ* Raman data by the straight application of Sampaio`s fit model based on Gaussian functions.

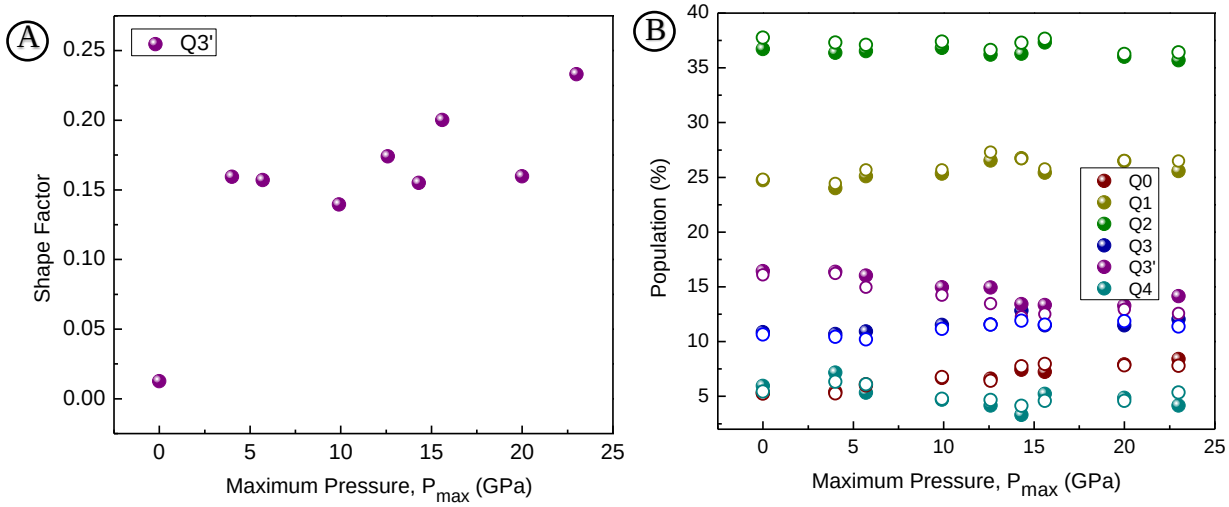

Figure 3.5: (a) Shape Factor to the $Q^{3'}$ unity obtained by the P6 procedure and (b) Q^n unities as a function of the maximum pressure (Pmax). The dots symbolize the P4(empty) and P6 (spherical) procedures.

IV. Pressure-Induced Structural Modifications

Some studies on alkaline [181, 183] and alkaline-earth [184, 185] silicates under high-pressure show that the Q^n change follows the disproportionation reaction:

$$2Q^n \rightarrow Q^{n+1} + Q^{n-1} \tag{3.4}$$

This equation predicts that the consumption of two given Q^n tetrahedra produces one immediately more polymerized (Q^{n+1}) and the other less polymerized (Q^{n-1}) tetrahedra. In the case of PS glass, one may expect the disproportionation reaction $2Q^2 \rightarrow Q^3_{tot} + Q^1$, however, the full set of curve-fit procedures is unanimous in showing no appreciable variation in the Q^2 population. It is important to note that we observe a trend, although subtle, in the depolymerization where Q^4 and Q^3_{tot} are ultimately converted to produce Q^1 and Q^0 species. It follows that the simple forms of Eq. (3.4) do not hold in describing the Q^n population modifications on the densified PS glass. BO and NBO contents were extrapolated based on the assumption that these are the only oxygen species in the glass, the same procedure was explicitly adopted in Ref.[187], to the $NaO\text{-}SiO_2$ glass

system investigated by ^{29}Si NMR spectroscopy. The NBO content can be determined from the Q^n population:

$$NBO = 4Q^0 + 3Q^1 + 2Q^2 + Q^3_{tot} \quad (3.5)$$

And the BO content as well:

$$BO = \frac{1}{2}(Q^1 + 2Q^2 + 3Q^3_{tot} + 4Q^4) \quad (3.6)$$

Where Q^3_{tot} is the sum of the two distinct Q^3 and $Q^{3'}$ units. This extrapolation gives a picture of the silicate lattice, providing BO and NBO proportions between them. Evaluation of PS at room conditions indicates a 2% O^{2-} content in the uncompressed glass [56]. However, these species are not directly accessible from Raman spectroscopy data [73].

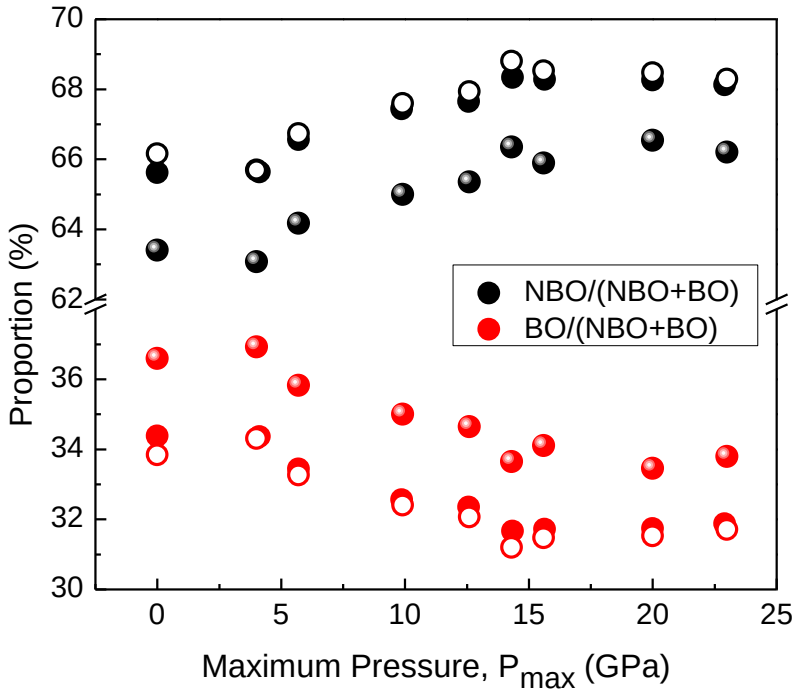

Figure 3.6: Bridging oxygen and non-bridging oxygen proportion as a function of the maximum pressure (Pmax). The dots symbolize the extrapolation by the P1(full-colored), P4 (empty), and P6 (spherical) procedures. The error bar due to the uncertainty propagation in the proportions is estimated as ±2% (not shown). Adapted from Pena et al., 2021 [162].

Figure 3.6 illustrates the NBO and BO proportions with Pmax calculated by the three different curve fit procedures. We observe that the P6 procedure delivers a more polymerized uncompressed structure in relation to the P1 and P4 procedures, which we attribute to its intrinsic overestimation of the Q^3_{tot} over the less polymerized tetrahedra. As a function of Pmax, we observe that an increase in the proportion of NBO occurs at the expense of BO (Figure 3.7), leading to network depolymerization. In line with the depolymerization reaction stated in Eq. (1.1), such

occurrence implies not only the existence of free oxygen (O^{2-}) within the uncompressed glass structure but also their consumption in the permanently densified glasses. Perhaps the saturation limit at 20 GPa is related to the complete consumption of O^{2-} within the glass structure.

From their IR spectra for hot-densified lead silicate glass, Yoshimoto *et al.*[161] reported modification of the Si-O stretching envelope, with a shift of the maximum towards lower wavenumbers, indicating also a possible silicon network depolymerization and overall NBO increase for the entire 33 to 67 mol.% PbO composition range. This last fact is contrary to the trend found in pressure-induced silicate glass with other compositions (e.g. sodium and aluminum), where the overall NBO population is generally reported to decrease [181, 188-190].

3.4. Summary and Conclusions

Ex-situ Raman measurements at room temperature were performed in a set of PS glass samples subjected to different Pmax covering a range up to 23 GPa. Such a procedure enabled the determination of the elastic and saturation limits at 4 GPa and 20 GPa, respectively. The former is low when contrasted to other silicate compositions, evidencing the more compact structure of the PS glass as found in the literature.

For the densified glass, the barycenter evolution of the high-wavenumber region, attributed to Si-O stretching modes, displays a shift toward lower wavenumbers, which can be associated with network depolymerization with increasing Pmax. This conclusion was refined with the spectral curve fit, giving a good estimation of the structural modifications of the Q^n population that was essentially the same applying Sampaio`s fit model, either with Gaussian functions or allowing a Gaussian-Lorentzian mixing. Noteworthy, due to the high lead content and broad Si-O-Si angle distribution of PS glass, the assumption of Gaussian shapes is justifiable and can be constrained for the full set of Q^n components.

Regarding the structural modifications: Q^0 and Q^1 populations were found to increase slightly, densification favored the $Q^{3'}$ over the Q^3, with an overall decrease in Q^3_{tot}, while Q^2 remained about the same. We observed a silicon network depolymerization as a pressure-induced effect as shown by an increase in the NBO proportion. These results are in opposite trend to those reported for other silicate compositions, implying not only the existence but also the consumption of free oxygen (O^{2-}) within the PS glass structure after a compression-decompression cycle.

CHAPTER 4 – IN-SITU MEASUREMENTS: PS GLASS STRUCTURE UNDER PRESSURE

4.1. Introduction

It is long known that the structure of densified glass is not equivalent to the structure of the glass under pressure; the intrinsic distinctions have justified the *in-situ* investigation of various glass compositions upon compression. In 1986, the first *in-situ* Raman study of glasses under pressure was performed by Hemley *et al.* [191] for vitreous silica compressed at room temperature up to ~30 GPa. Over the years, later investigations addressed silica [106, 192, 193], and other glass compositions [120, 184, 194-196].

For the PS glass, qualitative modifications on the low-wavenumber region applying 4:1 methanol-ethanol alcohol as the PTM comprised a combinatory *in-situ* Raman and Brillouin spectroscopic investigation of ours, ultimately reported in *The Journal of Non-Crystalline Solids* as "*Normal to abnormal behavior of $PbSiO_3$ glass: a vibrational spectroscopy investigation under high-pressure*" [163]. To the best of our knowledge, this was the only spectroscopic study performed for the PS glass under pressure, suggesting continuous pressure-induced modifications of the lead coordination as indicated by the changes in the low wavenumber region of the Raman spectra (Figure 4.1). This spectral region comprises three peaks: the BP, and two peaks initially centered at 95 cm^{-1} and 135 cm^{-1}, both assigned to Pb-O vibration.

At high pressures, *in-situ* Raman spectra displayed an inversion relationship to the intensity of the low-wavenumber peaks: decreasing the BP intensity and increasing the peak centered at 95 cm^{-1}, gradually suppressing the 135 cm^{-1} peak [163]. The decrease of the BP intensity with pressure was also observed in other glass compositions [101, 103-106]. In light of the elastic heterogeneities model proposed by Duval *et al.*[90], this effect on the BP is due to the reduction of the average nanodomain size [101] and softening of the interface regions between the correlation domains [103], decreasing the elastic constraints and hence homogenizing the glass network. Because of the PbO_4 attribution of the Pb-O peaks [112], the observed spectral modifications suggested a progressive change in the Pb environment possibly extending from minor deformation within the tetragonal pyramids (*e.g.* Pb-O bond lengths and internal angles) to the formation of highly coordinated PbO_n polyhedra [163].

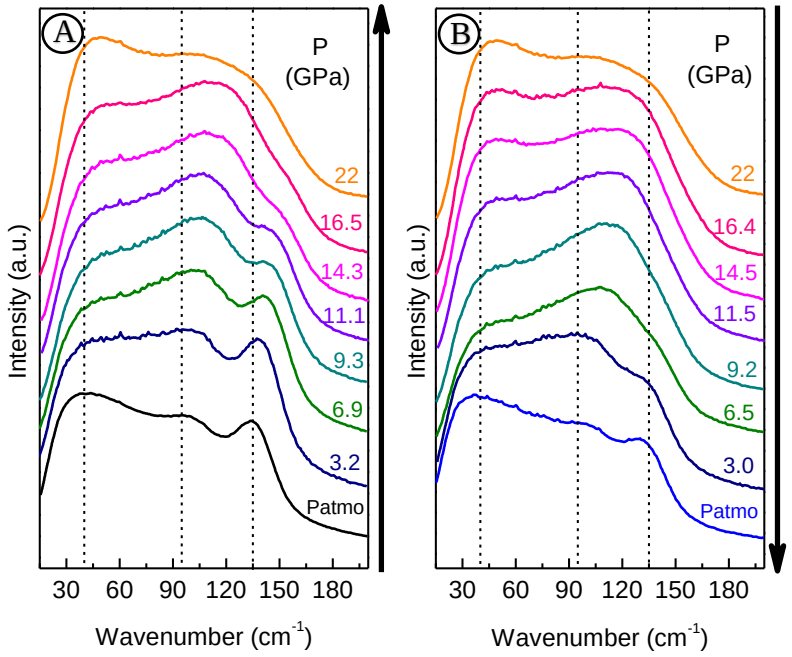

Figure 4.1:Low-wavenumber Raman spectra of PS glass recorded in-situ as a function of pressure (P) in a complete (a) compression and (b) decompression cycle, applying 4:1 methanol-ethanol solution as the PTM. Retrieved from Pena et al, 2022 [163].

The PTM applied in our published high-pressure studies of PS glass was the 4:1 methanol alcohol mixture, which has already enabled [162, 163]: (i) elastic and saturation pressure limits; (ii) a picture of the depolymerization in densified $PbSiO_3$ obtained in multiple loadings; (iii) and preliminary *in-situ* structural multiscale behaviors. Nevertheless, this alcohol solution presents bands at room pressure centered on 883, 1035, 1095, and 1158 cm^{-1} (as shown in Chapter 2), precluding an *in-situ* description of the high-wavenumber region of PS glass.

In order to describe the *in-situ* modifications in the Si-O stretching modes, and related pressure mechanisms leading to the depolymerization observed in the densified glass, we have combined efforts from spectroscopic and simulation means. We performed *in-situ* Raman measurements of PS glass under pressure, using as the PTM either nitrogen or argon gases in two independent runs, and correlated them to completed molecular dynamics simulations performed by our collaborators Dr. Adalberto Picinin and Dr. José Pedro Rino. These simulations referred to as 'our' as a way to distinguish them from those available in the literature [197-200], extended towards high-pressure the same potential reported therein [77].

This chapter is the basis for a future publication to be submitted to *The Journal of Non-Crystalline Solids*, in an attempt to describe the pressure modifications on the different range orders of the PS glass structure.

4.2. Experimental and Simulation Procedures

I. Experimental Procedures

In-situ Raman spectra of PS glass under high pressure were acquired at room temperature in independent loadings applying nitrogen or argon gas as the PTM. These gases require cryogenic conditions for their condensing and trapping into the DAC. The R_1 ruby luminescence line of Cr^{3+} enabled the pressure determination calibrated by Mao and Bell adjust [138]. In each run, vibrational spectra were recorded for a complete compression-decompression cycle up to the maximum pressure displayed in Table 4.1. At each pressure point, we performed the pressure increment, waiting at least 10 minutes for pressure stabilization before recording the Raman spectrum. Raman measurements were taken using a LabRAM HR micro-Raman spectrometer (ILM, France) from Horiba Jobin Yvon with a 532 nm laser wavelength as an excitation source. Each spectrum is an average of seven measurements of at least 60 seconds accumulation time in a range window. This way, Raman spectra acquisitions took from seven to twenty-one minutes at each pressure step.

Table 4.1: In-situ Raman Spectroscopy analysis for the PS glass performed with different PTM.

PTM	Hydrostatic Limit [130]	Maximum Pressure	Recorded Interval
Nitrogen gas	10.0 GPa	21±1 GPa	800-1200 cm^{-1}
Argon gas	10.0 GPa	20±1 GPa	5-1250 cm^{-1}

The high-wavenumber region of the Raman spectra was alternatively analyzed by the barycenter and the Q^n curve fit. In the latter, the bands were fitted by Gaussian functions applying Sampaio`s model [77]. Center position and HWHM there derived at room temperature, were allowed to change iteratively at each pressure applying the same constraints as in procedure P4 (see page 51).

II. MD Simulation Procedures

The algorithm of MD simulations consists of four main steps performed recurrently [201]: (i) summing up all interatomic interactions for the atomic positions computing the system's potential energy; (ii) calculating the resultant force experienced by each atom via energy differentiation; (iii) obtaining each atom's acceleration from Newton's law of motion; and (iv) updating the atomic positions and velocities after a time step via numerical integration.

The simulated PS glass comprises a set of 15,000 particles (3000 Pb + 3000 Si + 9000 O atoms), for which the effective interatomic potential and further technical details are described

therein [77]. Our collaborators have kindly provided MD results for progressing the understanding of the PS structure under pressure and extending the collaborative effort there published toward high-pressure conditions.

4.3. Results and Discussions

The organization of this chapter is as follows: In the first section, we will describe the evolution of the barycenter and general spectral modifications. In the second section, proceeding with the spectral curve fit, we will derive the Q^n evolution and contrast them to that obtained in the simulations. Finally, the last section addresses some MD insights into the overall glass structure under pressure.

I. Barycenter evolution

In-situ Raman measurements of the high-wavenumber spectral region were performed through two independent runs, with the DAC loaded either with argon or nitrogen gas as the PTM. Figure 4.2 illustrates the evolution of such spectral region for the argon gas loading, attributed to symmetric Si-O stretching vibrations without any parasitic sign from the PTM. Similar spectral evolution is obtained for the nitrogen loading.

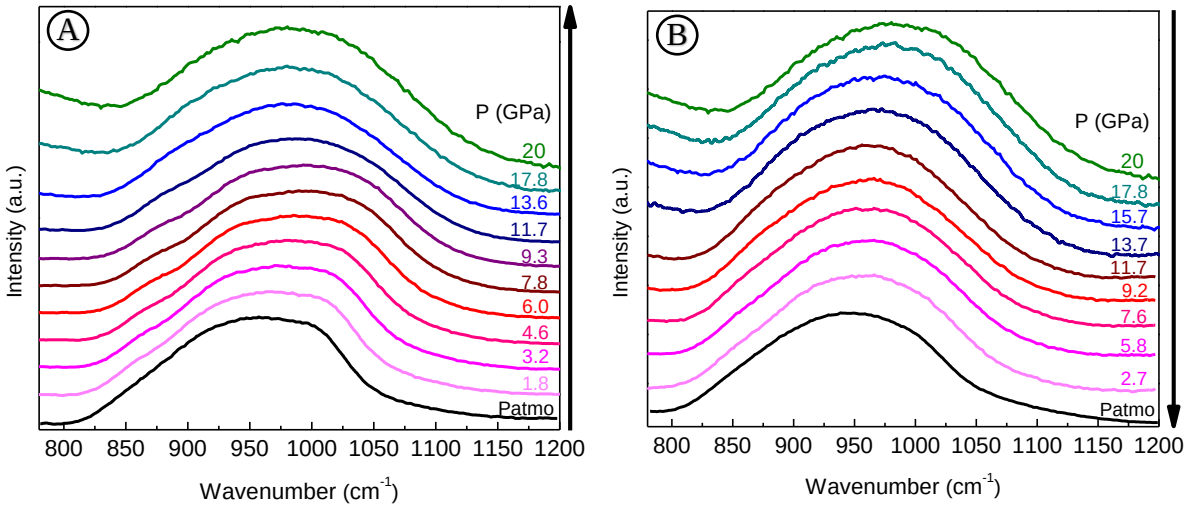

Figure 4.2: High-wavenumber Raman spectra of PS glass recorded in-situ as a function of pressure (P) in a complete (a) compression and (b) decompression cycle, applying argon as the PTM.

Figure 4.3 presents the barycenter evolution in complete pressure cycles. We observe a good agreement between the behavior obtained with nitrogen (empty dots) and argon (full-colored dots). The barycenter displays expressive changes under pressure, presenting higher values for the

compression than for the decompression path. The χ_b evolution upon compression suggests the occurrence of important structural modifications, which cannot be fully attributed to anharmonic effects. Then, the barycenter decreases monotonically upon decompression, reaching values lower than the uncompressed glass once the pressure is released.

Ex-situ measurements guide some of the descriptions for the *in-situ* data, allowing us to distinguish the pressure limit of ~ 4 GPa, which marks the transition from the elastic to the plastic regime. During the compression in the elastic regime, the envelope shifts linearly ($\frac{\partial \chi_b}{\partial P}$ = 5 $cm^{-1}.GPa^{-1}$), showing spectral features close to the uncompressed glass. Oppositely, in the plastic regime, the envelope evolves with major changes in the line shape and minor band-shift, resulting in a non-monotonic χ_b evolution that depends on the pressure range:

A. Up to 9.3 GPa: χ_b increases with pressure, as the high-wavenumber boundary moves toward high wavenumbers, letting the envelope width slightly larger;

B. From 9.3 to 15 GPa: χ_b remains about the same, whereas the spectral lineshape evolves toward a band symmetrization;

C. Above 15 GPa: χ_b increases again with pressure, as a result of a symmetric band that shifts toward high wavenumbers with small or no modifications on the lineshape.

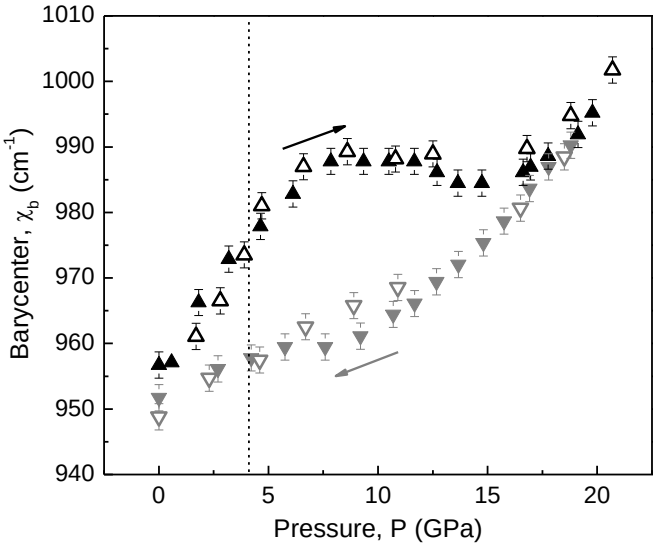

Figure 4.3: Barycenter of the high-wavenumber region as a function of the pressure (P). The full-colored symbols represent argon loading while the empty represent nitrogen gas. The dashed black line indicates the elastic limit.

Contrasting the *ex-situ* and *in-situ* displacements at 20 GPa, while in a densified glass the barycenter shifts by -8 cm^{-1} [162], the variation upon compression scales to $+45$ cm^{-1}. Given that

the more polymerized Q^n species correspond to the higher wavenumber modes [77, 162], these opposite trends suggest the formation of an intermediate more-polymerized state under high-pressure. In the decompression path, the envelope shifts toward the lower wavenumbers as the pressure drops. These modifications suggest that the pressure-induced network depolymerization reported in Chapter 3 takes place during the decompression, not necessarily by inverse mechanisms of the compression.

II. Curve fit: Raman and MD simulation

The correlation between the Raman experiment and MD simulation as a function of the pressure is directly accessed through the Q^n population, predicted independently by each method. A curve fit of the high-wavenumber region was performed considering the compression path, for which completed MD simulations developed by our collaborators can provide general structural insights into the SRO and MRO structure. These results are here contrasted as a function of the normalized pressure (P/P'), obtained by dividing the absolute pressures obtained in each method (P) by their respective pressure elastic limit (P`), defined in the previous chapter (see page 48). Vibrational means such as Raman and Brillouin spectroscopies estimate P'_{VIB}=4 GPa [162, 163]. Analogously, by analyzing the Q^n distribution of simulated glass obtained after compression under different maximum pressures (not shown), MD simulations presented P'_{MD}=30 GPa.

Contrasting their results, as illustrated in Figure 4.4, Raman spectroscopy and MD simulation appoint to a gradual polymerization upon compression in fair agreement with each other and with the trend suggested by the barycenter in the previous section. Nonetheless, the curve concavities and the absolute population between the experiment and simulation may differ. Despite these distinctions, the uncompressed structure configured mostly as Q^2 tetrahedra evolves towards that of Q^3 as the dominant tetrahedra at high pressure. More generally, the modifications comprise a decrease in Q^0, Q^1, and Q^2, whereas the total Q^3 and Q^4 increase. For the experimental data, we notice an overall underestimation of Q^4 by the curve fit under pressure, which we attribute to the baseline compensation for removing the background signal due to the diamonds (ν_0 =1333 cm^{-1}) [120].

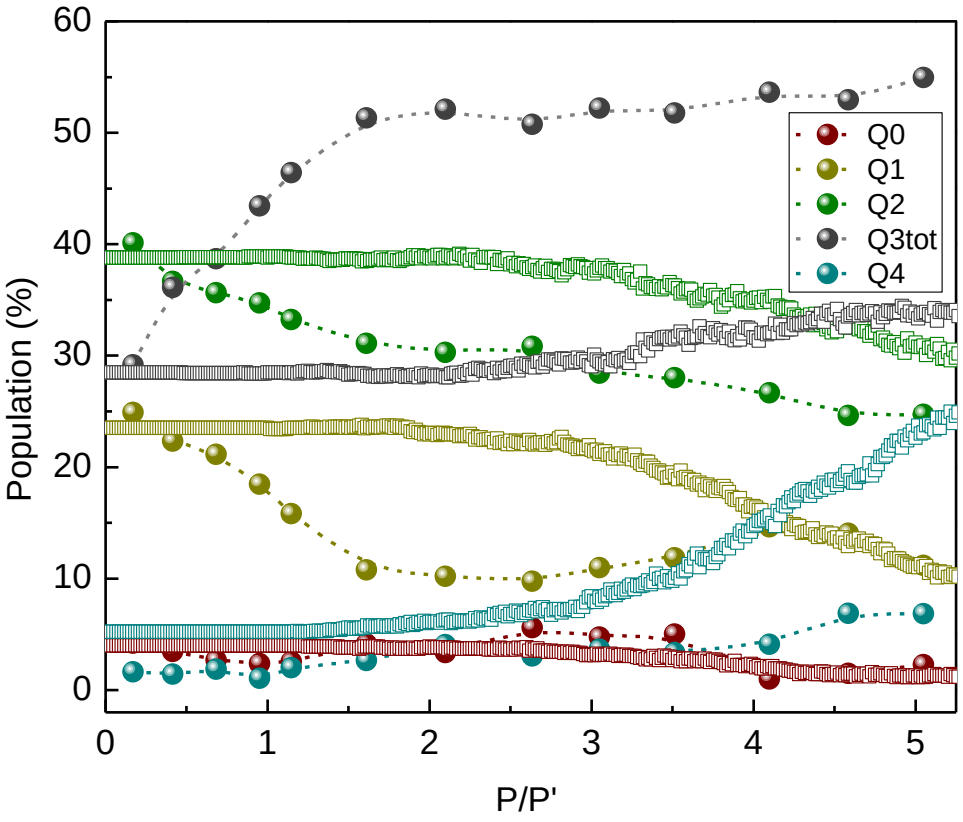

Figure 4.4.: Q^n evolution of PS glass upon compression obtained by combining Raman spectroscopy (spheres) and MD simulations (squares). MD data was kindly provided by Dr. Adalberto Picinin.

Figure 4.5a illustrates the oxygen proportion extrapolated from the Q^n population estimated by the Raman curve fit and MD simulation indicating the conversion of NBO in BO upon compression, which corroborates the silicate network polymerization. In the simulations, the distinct oxygen populations were alternatively obtained limiting $R_{cut} = 2.0$ Å, and inquiring about the oxygen coordination, which ranged from zero to three silicon cations (Figure 4.5b). In its turn, oxygen not connected to silicon is the so-called free oxygen (O^{2-}); the bonding to only one silicon is NBO; whereas the bonding to two silicon cations is BO. Oxygen coordinated to three silicon cations is called 'tricluster' and is inferred to account for charge balancing in other glass compositions such as the aluminates [40, 202]. Strictly, the physical interpretation of these last entities delivered by our simulations redundantly indicates a 3-fold clustering of silicon around the oxygen atoms for coordination spheres of fixed radius centered on the oxygens.

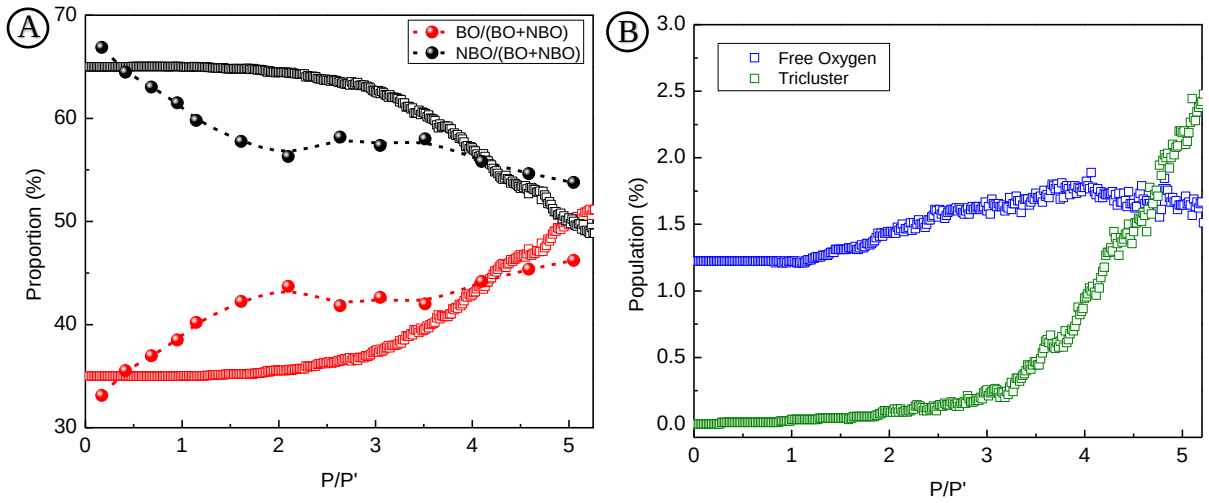

Figure 4.5.: (a) Proportion of bridging and non-bridging oxygen and (b) population of free oxygens and triclusters as a function of the normalized pressure. MD data was kindly provided by Dr. Adalberto Picinin.

High-pressure MD simulations of depolymerized silicates available in the literature indicate a progressive increase in BO at the expense of NBO, with a small but present triclusters population in the structure [203-205]. Although the initial abundance of free-oxygens and triclusters can correlate with the applied cooling rate of the simulations [206], our uncompressed glass presents the concentration of the former agreeing with ^{17}O-NMR quantifications and the latter absent [77]. As a function of pressure, our simulations picture a nearly constant free-oxygen proportion, whereas triclusters are formed, ranging up to 2.4% of the total oxygens. The population of the latter considers solely oxygen coordinated to three silicon cations, whereas the proportion of triclusters heterogeneously coordinated to silicon and lead or solely lead is estimated to be negligible. In the case of PS glass, the opposite variation trends between triclusters and NBOs imply an overall charge compensation within the network [207], not exclusively linked to charge-balancing the NBO, but probably performing the balance of highly coordinated lead environments that form under pressure, as further addressed in the next section.

III. Further MD Structural Insights

Besides the Q^n distribution and the NBO proportion, MD simulations may provide relevant insights into the glass structure under pressure: pair correlation functions, bonding distances, bond angles distribution, coordination numbers, etc.

The pair correlation functions, $g(r)$, indicate high-pressure prompting a decrease in the Pb-O, Si-O, and Pb-Si interatomic distances within the PS glass structure (Fig.4.6). Noteworthy,

the bimodal distribution displayed by the $g_{Pb-Si}(r)$ function gradually displays the short distance as the more expressive under pressure. Given its link with the two distinct Q^3 entities [77], this MD result agrees with the significant increase in $Q^{3'}$ upon compression, as obtained by the Raman curve fit. Such a favoring is also observed on the densified glass, despite the decrease in the Q^3_{tot} population once the pressure is released [162].

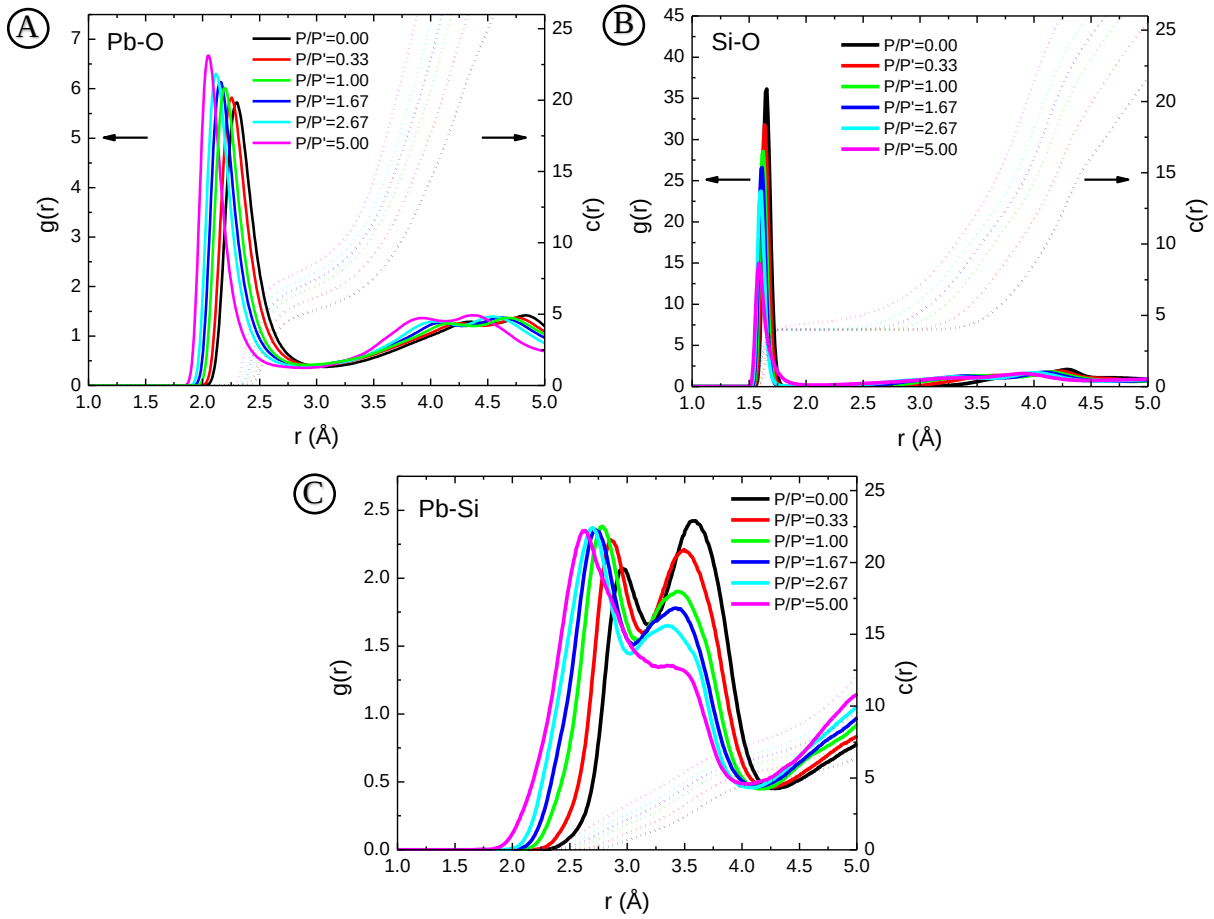

Figure 4.6: (a) Pb-O; (b) Si-O; and (c) Pb-Si pair correlation functions $g(r)$ and their respective coordination $c(r)$ as a function of the normalized pressure. Illustration kindly provided by Dr. Adalberto Picinin.

Bond lengths were modeled assuming a Lognormal distribution to fit the first peak in the $g(r)$ functions [77]. Si-O and Pb-O lengths reported in recent diffraction studies show a good agreement with the bond distances of the uncompressed glass [84, 208], which are found to decrease upon compression. This behavior follows the asserted decrease of cation-oxygen distance acting as a pressure mechanism on depolymerized glasses [203, 209]. We highlight the magnitude of the modifications involving the lead cations as five times higher than those taking place with the silicon cations, as shown in the evolution of the first peak in their respective $g(r)$ functions

(Fig. 4.6 a and Fig. 4.6 b). In the case of Pb-O bonds, the decrease in the average distances is attributed to the progressive formation of PbO_n polyhedra. On the other hand, the subtle decrease in the Si-O average distance with pressure cannot be explained by the same arguments. The non-monotonic behavior of the Si-O distribution (Fig. 4.7c) that first decreases and then increases with pressure suggests the participation of two processes in the bonding decrease, which we attribute: (i) initially, to the inter-tetrahedral angle closure (Si-O-Si) from 140º to 115º, which no longer changes above $P/P' = 1.67$; (ii) then, to the progressive network polymerization.

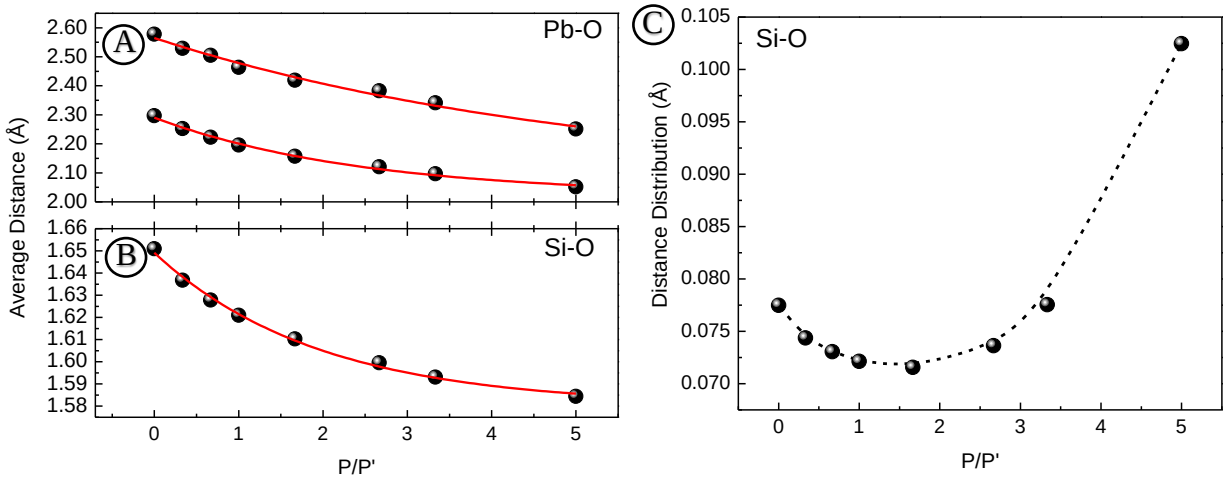

Figure 4.7: (a) Pb-O and (b) Si-O average distances and (b) Si-O distance distribution as a function of the normalized pressure. Exponential decay functions (red line) fit the average distances estimated by the simulations (black circles).

The closure of the inter-tetrahedral angle by a 'quasi-rigid' approaching of the SiO_4 tetrahedra corresponds to a decrease in the void space, leading to a homogenization of the Si-O distance distribution. Quasi-rigid as in our simulations inter-tetrahedral angle and Si-O average distance are both observed to decrease at the beginning of the compression, despite the inverse correlation found in crystalline silicates [210, 211]. It is also derived from these crystals the longer average distances to the Si-NBO (~1.62 Å) than to the Si-BO (~1.58 Å) bonds at room conditions [40, 211]. In consistence with the network polymerization upon compression, the decrease in the simulated average Si-O distances scales with these values. Such a length shortening without change in the coordination number leads to a more covalent character of the silicon bonding to oxygen [211].

MD simulations available in the literature indicate the presence of highly coordinated PbO_n polyhedra on high-density lead silicate glasses and melts [197-200]. In our simulations, the

$g_{Pb-O}(r)$ function presents non-zero values for distances immediately above the first peak (Fig. 4.6a). Hence, presenting a continuous distribution of allowed correlation distances between Pb and O atoms, which adds a further degree of complexity in delimitating the R_{cut}. For $R_{cut} = 2.6$ Å, the coordination sphere appoints to a continuous increase in the coordination number (CN) of oxygen atoms around lead, which *not necessarily* imply the formation of PbO_n polyhedra with n equal to the CN provided by the sphere.

As illustrated in Figure 4.8a, the simulated glass structure is mostly composed of 4-fold and 5-fold coordination at room conditions [77]. Upon compression, the number of oxygens coordinated to lead probed by the coordination spheres gradually increases, first by an increase in the 5-fold coordination, which presents a maximum at P/P'=0.33, and then to the substantial increase in the 6-fold coordination. In the plastic pressure regime, where P/P'>1, the proportions of 7-fold and 8-fold progressively become the most expressive with increasing pressure. In terms of the corresponding average coordination number, it increases exponentially toward 7.5 (Fig.4.8b). Interestingly, *in-situ* high-pressure simulation performed on the PS melt (3200 K and 35 GPa) also reports the same behavior converging to a similar value [197].

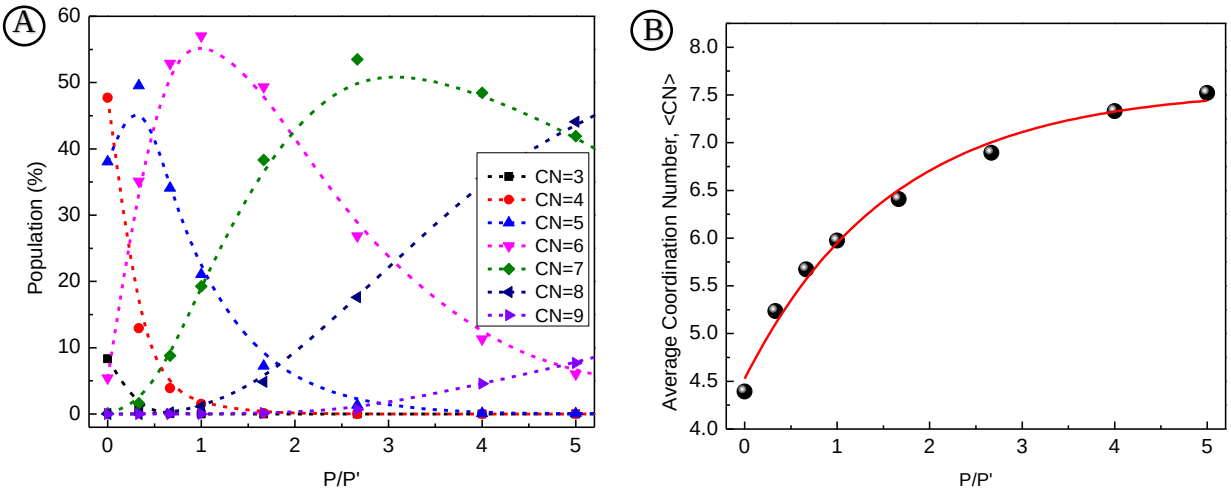

Figure 4.8: (a) Distribution of coordination numbers (CN) around the lead and (b) the corresponding average coordination number, <CN> as a function of the normalized pressure. The first illustration was kindly provided by Dr.David Sampaio.

Referring to the only *in-situ* spectroscopic study available in the literature [163], such a progressive change in the environment around Pb correlates well with the linear increase of the refractive index weighted longitudinal sound velocity observed by Brillouin spectroscopy and the

reported modifications on the low-wavenumber Raman region. Given the high-sensibility of Raman spectroscopy to the vibration of Pb-O bonds, we reasonably consider the formation of highly coordinated PbO_n polyhedra as a possible structural modification under high pressure, and whose detailed description regarding n requires suitable characterization methods, *e.g.* X-ray absorption or X-ray Raman Scattering spectroscopies.

4.4. Summary and Conclusions

In-situ Raman spectra were acquired in compression-decompression cycles applying nitrogen or argon gases as the PTMs. Such a procedure enabled us to probe the evolution of the high-wavenumber region and the related modifications of the symmetric Si-O stretching vibrational modes. The one-parameter barycenter displays increasing values during the compression and decreasing values in the decompression path, suggesting the resulting depolymerization in densified PS glass is intermediated by a more-polymerized state under pressure. We inferred that depolymerization occurs upon decompression, not necessarily through reverse mechanisms from the compression path.

Upon compression, the combination of *in-situ* Raman and MD simulations extended the corroborative effort to describe the structure of the PS glass towards high-pressure conditions, enabling a multiscale picture of the structural modifications. The Raman curve-fit and simulations agree on the increase of Q^3 units, then becoming the predominant tetrahedra under high pressure. In both techniques, the BO population increases at the expense of the NBO population. MD simulations further suggest the decrease in the cation-oxygen average distances as an important pressure mechanism, agreeing with studies conducted in other depolymerized glass compositions. For Pb, such a decrease occurs accompanied by the gradual formation of highly coordinated PbO_n polyhedra. Regarding Si, the subtle variation seems to correlate with the conversion of Si-NBO towards Si-BO and therefore, the increasing polymerization degree of the SiO_4 tetrahedra.

CHAPTER 5 – CRYSTALLIZATION IN PS GLASS: TOWARDS GLASS-CERAMICS

5.1. Introduction

The mastering and controlling of the glass crystallization upon heat treatment are mandatory conditions to obtain glass-ceramics. At a given temperature, the overall crystallization is a combination of the nucleation and the growth processes taking place in a glass matrix. Further complexity is delivered by the possible formation of metastable phases before reaching the most stable state, as enunciated by Ostwald's rule of stages [212]. Contrastingly, as critically addressed by Schmeltzer *et al.* [213], the classical theory of nucleation assumes implicitly the properties of the macroscopic crystalline phase to be the same as the beginning stages of the crystal, which once formed, grows without abrupt modification to the bulk and surface properties.

The nucleation consists of the crystalline nuclei formation, which may occur randomly with equal probability in any volumetric site (so-called homogeneous nucleation), or spanning on preferable volume or surface sites (heterogeneous nucleation) [214]. Noteworthy, the precipitation of metastable phases followed by the appearance of the stable crystalline phase on top has a heterogeneous character [215, 216]. Systems presenting heterogeneous surface nucleation are dependent on the density of defects on the surface, presence of edges, tips, cracks, scratches, foreign particles, *etc.*, as addressed therein [3].

Lead metasilicate glass is a composition where the crystal nucleation is heterogeneous. There is no evidence of internal, but only surface nucleation [4]. In its turn, the growth process is controlled by surface crystal growth [10, 11], whose kinetic rates are available from 673 K to 998 K, albeit the formation of different polymorphs in this temperature range. The crystalline phases that precipitate in heat-treated PS glass consist of stable alamosite, and two metastable referred to as hexagonal $PbSiO_3$ (H-PS) and 'low-temperature' $PbSiO_3$ (L-PS) [73, 74, 118].

The natural alamosite was first reported in 1909, from mineral samples originating from Alamos, Mexico [217]. Geller *et al.* [115] noticed the optical properties of the crystal formed in PS glass were very similar to the mineral alamosite, which was confirmed by X-ray diffraction [218]. Ever since, these findings inserted the knowledge of the alamosite in the material science field, enabling several distinct investigations of this crystal with respect to the parental glass [49, 50, 66, 73, 74]. Regarding the metastable phases, Billhardt *et al.* [116] were the first to describe

the hexagonal phase, under the designation T-$PbSiO_3$, and Smart *et al.* [118] were the first to report the L-PS phase. More details on each of these crystalline polymorphs are available in Chapter 6. Focusing on the overall crystallization and phase transitions, Lippmaa *et al.* [219] investigated by ^{29}Si NMR spectroscopy lead metasilicate glass submitted to different isothermal heat-treatments. They observed distinctions in their *ex-situ* spectra when contrasting the samples crystallized at 823 K, 748 K, and 983 K, and indicated the overall crystallization in lead metasilicate glass, from which alamosite emerges, as a very complex process.

In this chapter, we examine with *in-situ* Raman spectroscopy the overall crystallization in PS glass, in order to characterize the phase evolution and demystify some of the alleged complexity, further providing evidence for Ostwald's rule of stages in this system. The PS crystallization was approached in non-isothermal and isothermal conditions, with the latter resulting in a publication in *The Journal of Non-Crystalline Solids* entitled: "*In-situ Raman spectroscopy unveils metastable crystallization in lead metasilicate glass*" [28].

Noteworthy, this vibrational method is suitable for studying the crystallization kinetics of glasses [220], once it is sensitive to small quantities of well-ordered clusters that appear locally at relatively early crystallization stages as sharp peaks, against the broad glass bands that compose the spectral background [221]. Another advantage of the applied technique lies in the availability of the Raman spectra of the three crystalline phases at room temperature as reported by Furukawa *et al.* [73, 74].

5.2. Experimental Procedures

In-situ measurements were taken using a Horiba-Jobin-Yvon HR800 Evolution micro-Raman spectrometer (GEOR, Brazil). The laser wavelength of 532 or 633 nm was used as excitation sources with a maximum laser power of 1 mW on the sample. Spectra were collected using the 600 slits/mm grating between 10 and 1200 cm^{-1}. Despite the relatively low spectral resolution for the 1800 slits/mm grating, this step was justified for the temporal resolution required during the crystallization.

Very small polished samples (~ 1 mm^3) were used to minimize temperature gradient effects. Multiple non-isothermal and isothermal heating runs were performed, while we show here two of the most significant for each. Figure 5.1 illustrates schematic temperature increment in the conditions of (i) constant heating rate; and (ii) fast heating followed by stabilization at a given

temperature. The former represents a non-isothermal condition. In the latter, it is assumed that the heating process from room temperature until the target temperature has only a small influence on the crystallization effects.

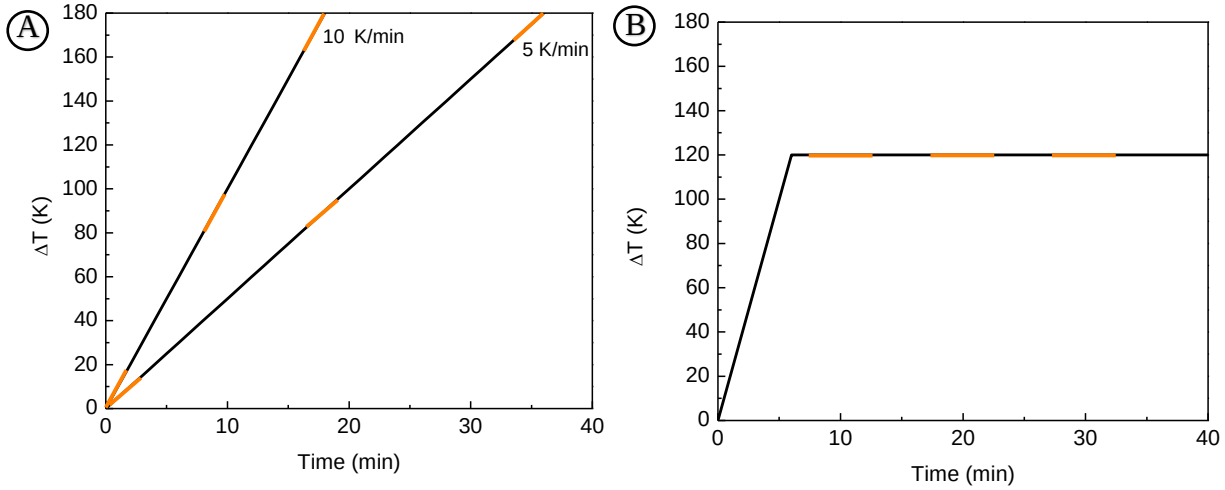

Figure 5.1: Schematic temperature increment for the (a) non-isothermal and (b) isothermal heating runs applied to study the overall crystallization of PS glass.

In the non-isothermal runs, the sample was heated from room temperature until 1093 K, at a constant heating rate of 10 K/min or 5 K/min (Fig. 5.1a). Spectra were collected as a function of the temperature, such that each spectrum is an average of three measurements of 10 s each, performed while the temperature was continuously increasing. The temperature variation during the measurement is therefore one-half of the applied heating rate. The labeled temperature sets the temperature where the acquisition started. Spectra were taken every 50 K up to 673 K, and 25 K thereafter. In the isothermal runs, the sample was heated from room temperature until the target temperature, 823 K or 873 K, at a heating rate of 20 K/min step (Fig.5.1b). Spectra were then collected in independent runs as a function of the time. Each spectrum is an average of six measurements of 15 s each, taken every 2 minutes (until 30 min), five minutes (until 60 min), and finally every ten minutes thereafter.

5.3. Results and Discussions

I. Non-Isothermal Crystallization

In the non-isothermal crystallization, the system is submitted to different temperatures, and hence energy configurations as a function of time. Such an investigation relates strongly to thermal studies where the temperature is incremented by a fixed rate, *e.g.*, differential scanning calorimetry

(DSC) and differential thermal analysis (DTA). For a heating rate of 8 K/min, the DTA curve available in the literature displays no abrupt thermal change, characterizing a gradual transformation towards alamosite [222]. For the standard heating rate of 10 K/min, the DSC curve of PS glass gives rise to two exothermic peaks at 893 K and 983 K attributed to crystallization [113]. We went for applying a constant heating rate (Fig.5.1a), whether 10 K/min or 5 K/min.

A one-parameter approach is obtained by the barycenter of the high-wavenumber Raman region during the glass heating, analogous to the procedure performed in the previous chapters. Because of the different behaviors of the barycenter with temperature, we distinguish three stages in both non-isothermal runs (Fig. 5.2.a and Fig. 5.3.a). First, the barycenter decreases monotonically, then abruptly increases, and so decreases to the position as the extrapolated line connected to the pristine glass. These stages correspond respectively to the glass depolymerization, crystallization onset, and melting, testifying to the potential of the barycenter in describing semi-quantitatively the phase transformation as a function of the temperature.

In the glass and SCL states, we observe an initial shift toward the low-wavenumber region as a function of temperature. For the 10 K/min rate, this variation is satisfactorily approximated by a linear function ($R^2 = 0.94$), whose angular coefficient is $-1.10^{-2} cm^{-1} K^{-1}$. Anharmonic studies performed on the alamosite crystal appoints to temperature coefficients one order of magnitude lower [223]. Beyond the anharmonicity, these quantitative distinctions indicate that structural modifications may take place. Indeed, the detailed description of the PS structure performed by combining Raman spectroscopy and molecular dynamics simulations corroborate depolymerization, as the NBO population increases with temperature. Crystallization onset manifests by the increase of the barycenter value to those of the glass/SCL, due to the spectral line shape that changes drastically.

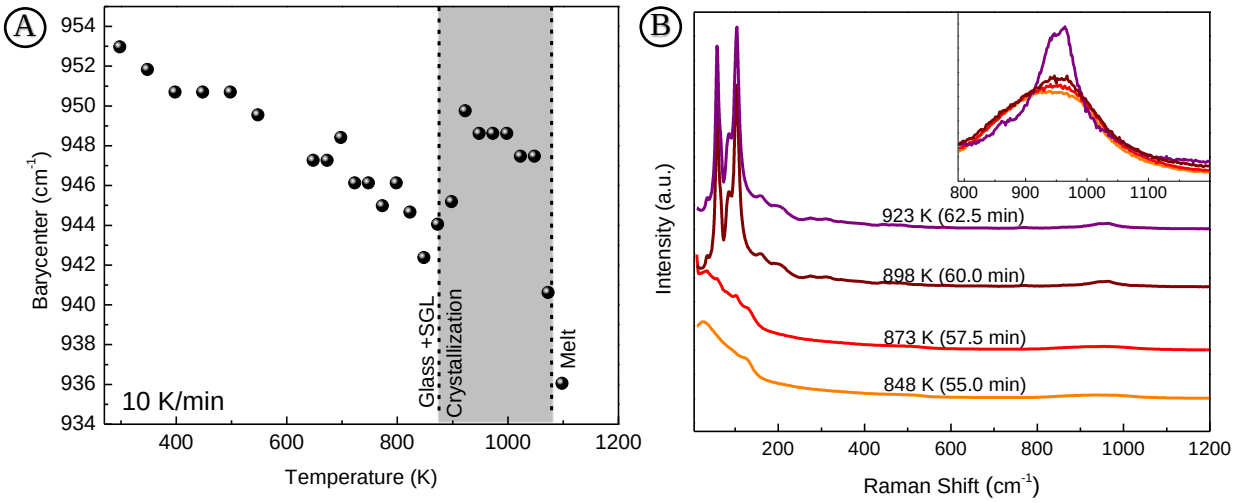

Figure 5.2: (a) Barycenter of the high-wavenumber Raman region and (b) selected Raman spectra as a function of temperature during non-isothermal crystallization for a 10 K/min heating rate.

Following the 10 K/min heating of PS above ~848 K (Fig. 5.2b), we observe the overall crystallization taking place as the spectra change towards the one of alamosite. At 873 K, crystal peaks start to overlap the broad glass features, indicating the crystallization onset. Already at 923 K, the high-temperature spectrum of alamosite becomes evident [223]. In the range of 50 K (5 minutes), the crystallization modifications taking place in the glass cease. Then, alamosite spectra modify gradually towards the melt, which was detected by Raman spectroscopy at 1073 K. For the same heating rate, the DSC curve in Figure 2.1 (page 32) displays an inflection point at 682 K, which at this rate delivers an estimation of T_g [34]; two exothermic peaks at 838 K and 883 K, marked as T_{c1} and T_{c2}, respectively associated with the formation of the metastable and alamosite crystalline phases [113]; and a narrow endothermic peak at 1039 K, corresponding to the melting temperature [115-118]. Despite the distinctions between Raman and DSC absolute temperatures, the detailed phase transformation is too fast to be probed at a 10 K/min temperature rate.

We proceeded with an analogous run at a 5 K/min heating, for which the evolution of the barycenter (Fig. 5.3a) was similar to the observed previously where the evolution can be fit by linear regression ($R^2 = 0.96$), presenting the same angular coefficient as the obtained previously at a faster rate. Due to the relatively long time in between one spectrum and another, we were able to collect micrographs along the crystallization process.

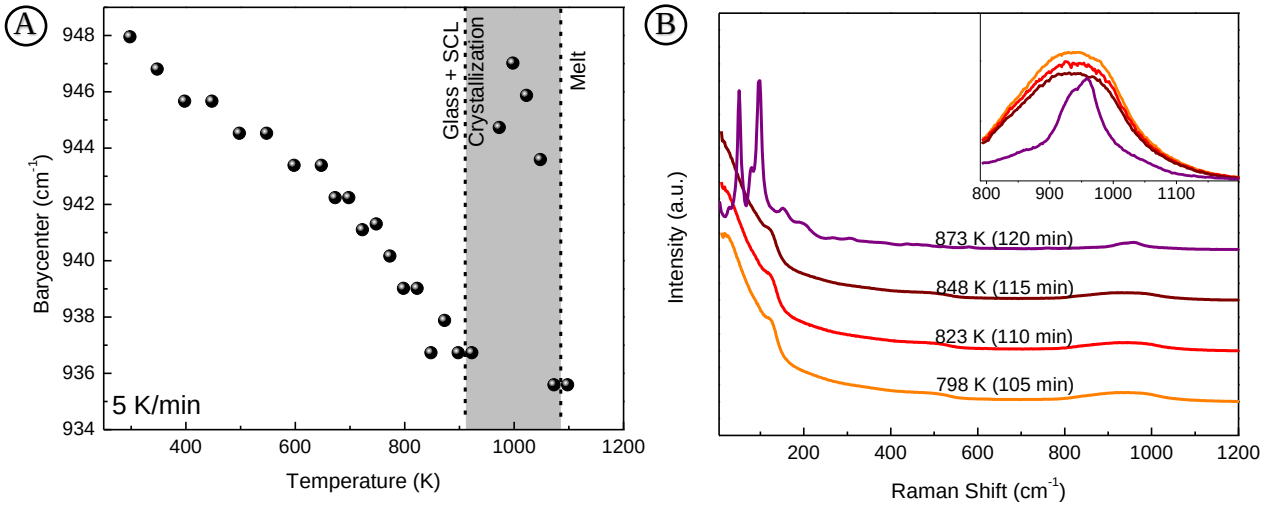

Figure 5.3: (a) Barycenter of the high-wavenumber Raman region and (b) selected Raman spectra as a function of temperature during non-isothermal crystallization for a 5 K/min heating rate.

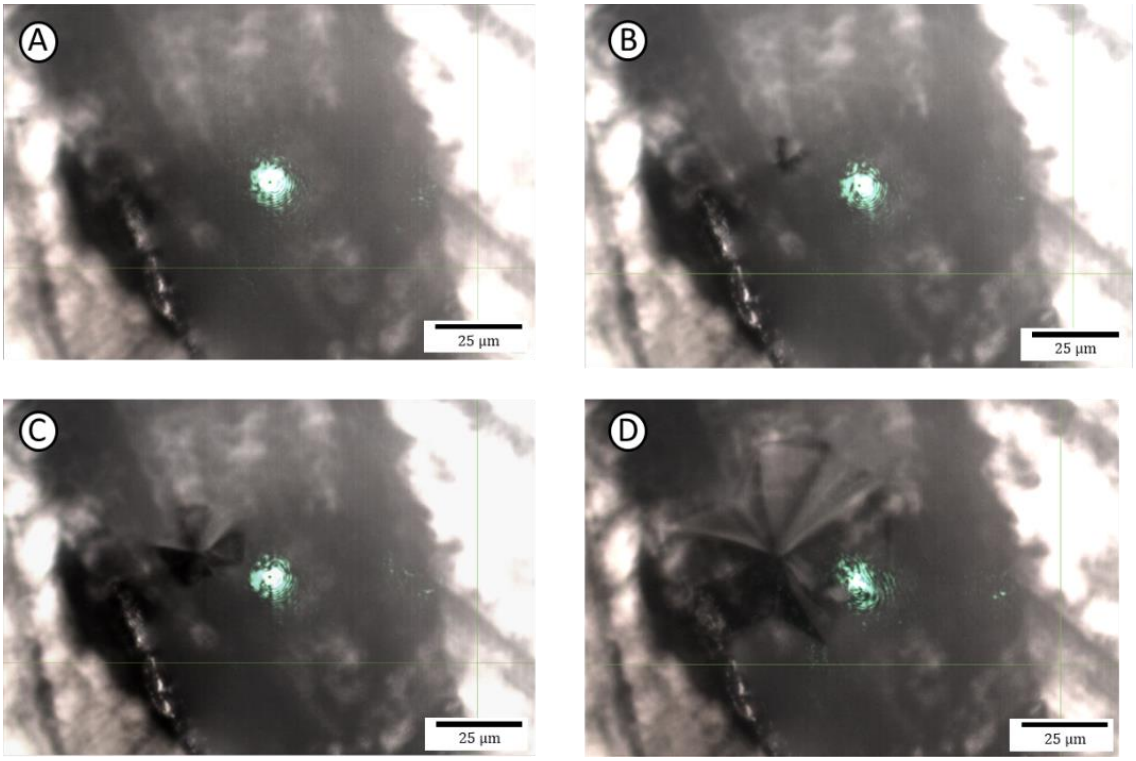

Figure 5.4: Micrographs during the non-isothermal heating of PS glass at a 5K/min rate obtained at a fixed position at (a) 773 K (100 min); (b) 823 K (110 min); (c) 848 K (115 min) and (d) 873 K (120 min).

Focusing on the crystalline morphology, H-PS was reported to associate with a hexagonal-like crystal shape, whereas L-PS relates to an ellipsoidal crystal habit [28]. The succession of micrographs indicates the precipitation of L-PS at 773 K. As the temperature continuously increases, no abrupt change occurred up to 823 K, where H-PS precipitates at a neighboring location. The appearance of these metastable crystals at different sites suggests that there is no interconversion between them. At 848 K, the hexagonal-like morphology is visually larger. Already at 873 K, the crystal edges coalesce; the acquired spectrum then (Fig. 5.3b) shows characteristic alamosite features, indicating the phase conversion towards the stable crystalline phase, whose growth rate is maximum at this temperature.

As a matter of fact, Neiman *et al.* [11] performed the first study of alamosite kinetics in PS glass for temperatures ranging from 773 K to 998 K. Cassar *et al.* [10] reinvestigated the crystal growth rate on these glasses extending the low-bound temperature of the available experimental dataset to 673 K. Despite the good agreement with Neiman`s dataset in the temperature range where they overlap (773 K - 823K), the crystalline morphology presented in the publication is that of L-PS confirmed with Raman spectroscopy (not shown). In the case of Neiman`s work: (i) either they worked with the alamosite phase as they alleged; (ii) or they obtained a phase transition that does not change the kinetics behavior over the investigated temperatures. We exclude the hexagonal polymorph to take part due to the morphological constraint reported therein [11]. The conjunction of these observations leads one to infer that L-PS and alamosite have coincident growth rates, at least in the temperature range where they overlap. In the countersense, the scarce investigations addressing growth rates of the metastable polymorphs in the literature seem to converge to the stable phase presenting at least one order of magnitude higher than those of the metastable phases [224, 225].

A general trend identified in all the non-isothermal runs is the transformation of the metastable phases towards alamosite is completed at 923 K, the temperature where the growth rate is maximum in such a crystal. This observation suggests that studies performed in view to understand the crystalline phase transformation should be performed either at lower temperatures or require an approach with quasi-stationary heating variation, such as the isothermal crystallization presented in the next section.

II. Isothermal Crystallization

In the isothermal crystallization, the system is held at a given temperature at which the probed modifications as a function of time are due to its intrinsic instability to the crystalline state at a given energy configuration. As the probing temperatures are usually higher than the glass transition temperatures ($T > T_g \approx 682$ K), such investigations rigorously address the SCL state. Given that higher temperatures are associated with higher kinetic energies, and the crystal growth rate is maximum at 923 K [11], we conducted the isothermal runs below this temperature.

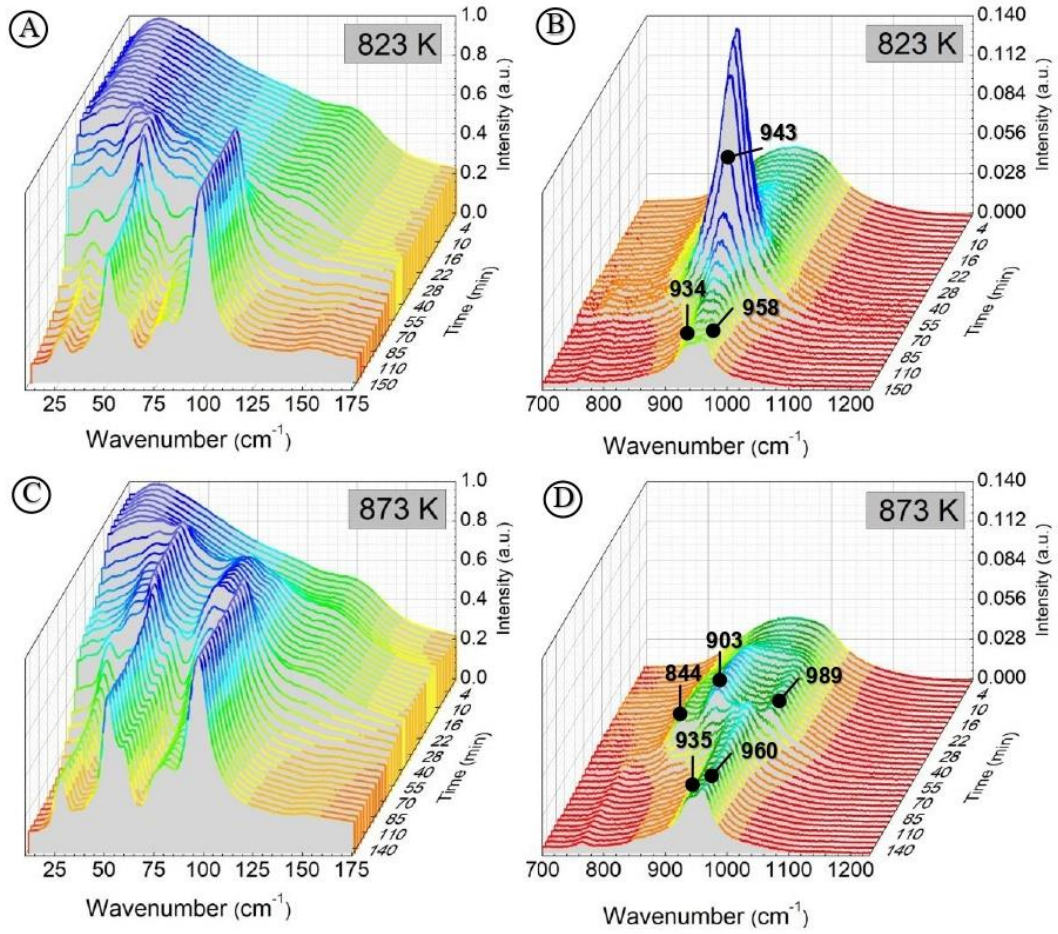

Figure 5.5: Time evolution of the Raman spectra obtained in isothermal crystallization at a fixed position show (a) the low-wavenumber and (b) the high-wavenumber spectral regions at 823 K and (c) the low-wavenumber and (d) the high-wavenumber spectral regions at 873 K. Adapted from Pena et al., 2020 [28].

The spectra evolution as a function of time is presented in Figure 5.5 as published therein [28]. Our *in-situ* spectroscopic study unveiled the intermediate polymorphs to differ as a function of the isothermal temperature. *In-situ* Raman spectra taken as a function of time at 873 K revealed that the crystalline phases evolved from H-PS polymorph to alamosite, whereas at 823 K, the

crystallization pathway proceeded directly from the L-PS to alamosite [28]. These attributions are enforced by the comparison with the Raman spectra of these crystalline phases at room temperature [73, 74], for which more details are presented in the next chapter.

Figure 5.6 illustrates the isothermal crystallization pathway from the SCL to alamosite, intermediated whether by L-PS (for T < 823 K) or H-PS (T > 873 K). Except for the early and final stages, the processes display mixed phases that makes it difficult for a quantitative approach due to two major reasons. First, any curve fit should account for the six Gaussian functions for the glass and a multiple number of characteristic Lorentzian functions for each crystal. Second, any estimation quantifying the distinct phases in the intermediate crystallization stages would further require their Raman activity [220].

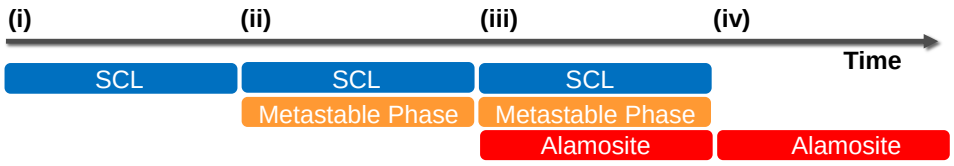

Figure 5.6: Flow-chart of the isothermal crystallization pathway in PS glass as a function of time. The intermediate metastable phase is temperature-dependent: L-PS (at 823 K) and H-PS (at 873 K).

As a function of the time, semi-quantitative analysis by the barycenter distinguishes the four different stages of the phase evolution in the isothermal processes (Fig 5.7a), which comprises: (i) initially the SCL, and then (ii) the SCL along with the intermediate metastable phase. The processes follow with (iii) a mixture of the intermediate and alamosite phases, coexisting with a remaining SCL phase prior to (iv) a complete conversion to alamosite, as qualitatively stated previously [28]. Although not evident from this one-parameter procedure, one experimental characteristic that supports the assertive of a remaining SCL phase along with the metastable phases is the persistent signal due to the BP at 40 cm^{-1} (Fig. 5.3a and Fig. 5.3c).

Closer regard on stage (iii) in both isotherms (Fig.5.4b and Fig. 5.4c) indicates that the phase mixing evolved rapidly towards the crystallization completion, possibly self-stimulated by the initial appearance of the alamosite. The presence of the stable crystal prompting the metastable crystal disappearance was reported in calcium aluminum silicate [226]. In the case of PS, such an evolution from both metastable crystals towards alamosite is adjusted by an exponential curve, whose distinct characteristic times could be attributed either to the distinct transformation mechanisms or to the temperatures involved.

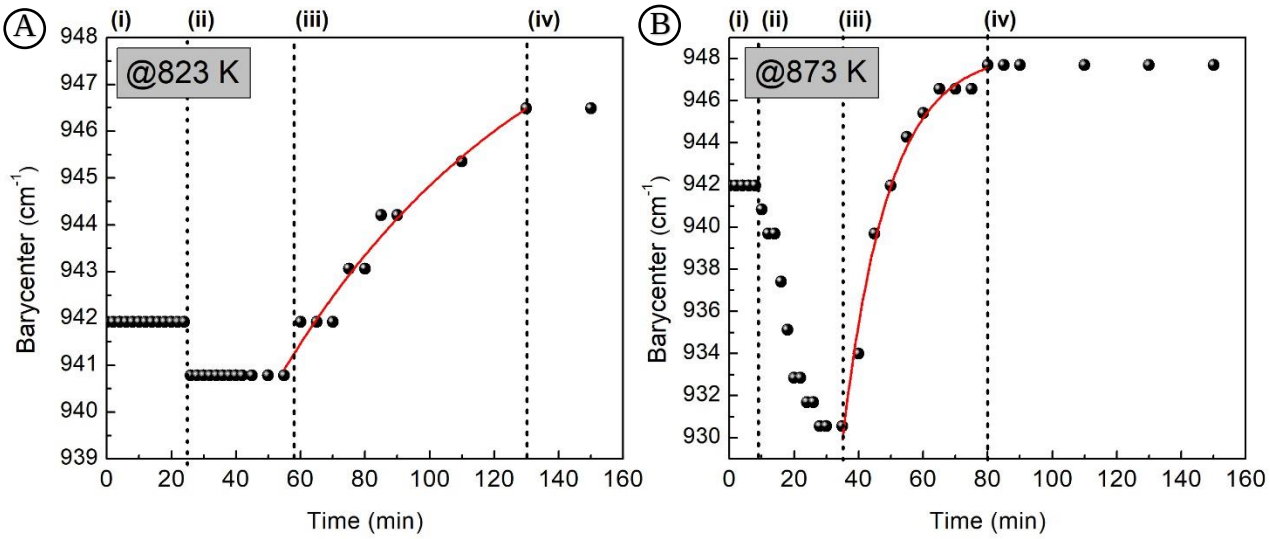

Figure 5.7: Barycenter of the high-wavenumber Raman region as a function of time during isothermal crystallization at (a) 823 K and (b) 873K.

5.4. Summary and Conclusions

This study of lead metasilicate glass by *in-situ* Raman spectroscopy provided a detailed description of the phase evolution during the overall crystallization of PS glass. Three phases crystallize in lead metasilicate glass: the stable alamosite and the metastable H-PS and L-PS. Their visual appearance and crystalline degree depend on the time and temperatures involved, as observed during the non-isothermal and isothermal runs.

Ostwald's rule of stages predicts that crystal nucleation is intermediated by one or more metastable phases before the thermodynamically stable phase. We provide evidence for its occurrence in the PS glass composition, through distinct metastable crystalline phases at different temperature treatments: Raman spectra taken as a function of time at 873 K revealed the crystalline phases to evolve from the H-PS polymorph to alamosite, whereas at 823 K, the crystallization pathway proceeded from the L-PS to alamosite. These runs do not evidence any signal of conversion of one metastable crystal to the other.

More generally, in systems where the Ostwald rule applies, the overall crystallization extends to the combination of nucleation, crystal-crystal phase transformation, and growing processes occurring simultaneously, indicating a new variable to be continuously probed in the kinetics investigations: the crystalline phase.

CHAPTER 6 - CRYSTALS IN PS GLASS: EXTREMAL CONDITION INVESTIGATION

6.1. Introduction

Smart *et al.* [118] have described the synthesis conditions to obtain single-phase samples of the three lead metasilicate crystals. According to them, there are four different ways to obtain alamosite, consisting of (i) a series of sintering and grinding of lead oxide and quartz precursors; (ii) crystallization of PS glass above 813 K; which the authors claimed to be ready; (iii) PS melt undercooling down to temperatures higher than 933 K, where it is left to crystallize for several hours; (iv) glass hydrothermal crystallization at 773 K and 300 bars for 48 h. These authors reported that the H-PS phase could be obtained solely by undercooling a PS melt to 923 K, and the pure L-PS can be formed at 753 K by glass crystallization for 14 days.

As a straight consequence of our finding regarding the overall crystallization in Chapter 5, we rectify the assertion that alamosite is 'readily' obtained above 813 K and described specific heating conditions to precipitate H-PS phase on the PS supercooled liquid, as reported in Ref.[28]. Even so, the physical reasons for the temperature-dependent crystallization routes at different temperature treatments are yet unclear.

In this chapter, we will investigate the fully crystallized alamosite, L-PS and H-PS under extreme conditions. Such a study is two-fold. Firstly, it indicates the stability ranges and phase transformation regimes of each crystalline phase. Secondly, it sheds further light on the pathways from the glass to the alamosite phase under different temperature treatments.

6.2. Experimental Procedures

The three crystalline phases were obtained following the synthesis procedures detailed therein [118], and were kindly provided by Dr. David Sampaio and MSc. Ricardo Lancelotti. The final samples showed high crystallinity as revealed by the defined XRD peaks (not shown).

Raman investigations were performed at high temperature and high pressure under similar spectral acquisition conditions. Raman spectra were acquired using a Horiba-Jobin-Yvon HR800 Evolution micro-Raman spectrometer and the laser wavelength of 532 nm as the excitation source. Spectra were acquired using the 1800 slits/mm grating. Each spectrum is an average of seven measurements of 40 s each, with a maximum laser power of 1 mW on the sample.

The effect of temperature or pressure was investigated alternatively. At room pressure, the temperature was incremented every 50 K (or 25 K at higher temperatures). In this case, the polymorphs investigated were the finely powdered crystals. At room temperature, the pressure was increased every 1 GPa in a DAC loaded with 4:1 methanol-ethanol solution as the PTM and ruby as pressure calibrant. In this case, the probed sample was a crystal piece of each phase selected from the abovementioned powder. At each step, the spectral acquisition was performed after waiting at least 5 minutes for temperature and 10 minutes for pressure to stabilize.

6.3. Results and Discussions

Initially, we explore the structural distinctions of the crystalline phases at room conditions based on the assignments available in the literature. Then, we summarize the effect of temperature and pressure on the phase stability, discussing possible mechanisms related to the different crystallization pathways observed in the last chapter. In-situ Raman spectra as a function of temperature were taken up to 1000 K, whereas the pressure was incremented up to ~6 GPa.

6.3.1. Crystalline Polymorphs at Room Condition

Since the XIX century, crystalline structures are characterized by their lattice type and atomic motifs, which describes completely the crystalline structure by translational symmetry of the unit cell. As known for half a century, alamosite is monoclinic consisting of 12 silica tetrahedral chains and pyramidal spiral chains of lead [227, 228], whereas the metastable phases, namely L-PS and H-PS, still lack such a detailed structural description [73, 74, 118]. Even so, the X-ray diffraction pattern from the H-PS phase can be indexed as a hexagonal unit cell [229].

Full Raman spectra obtained at room conditions of the three crystalline phases together with the PS glass are displayed in Figure 6.1a. In analogy with the isochemical $PbSiO_3$ glass [71, 72] and the isomorphic monoclinic $PbGeO_3$ crystal [230, 231], we assign as a general trend the low-wavenumber spectral range either to extended lattice modes or localized Pb-O modes of vibration, whereas the high-wavenumber is due to Si-O vibrational modes [231]. A detailed description of their phonon assignments would require first the solution of their lattice structure and then labored theoretical simulation.

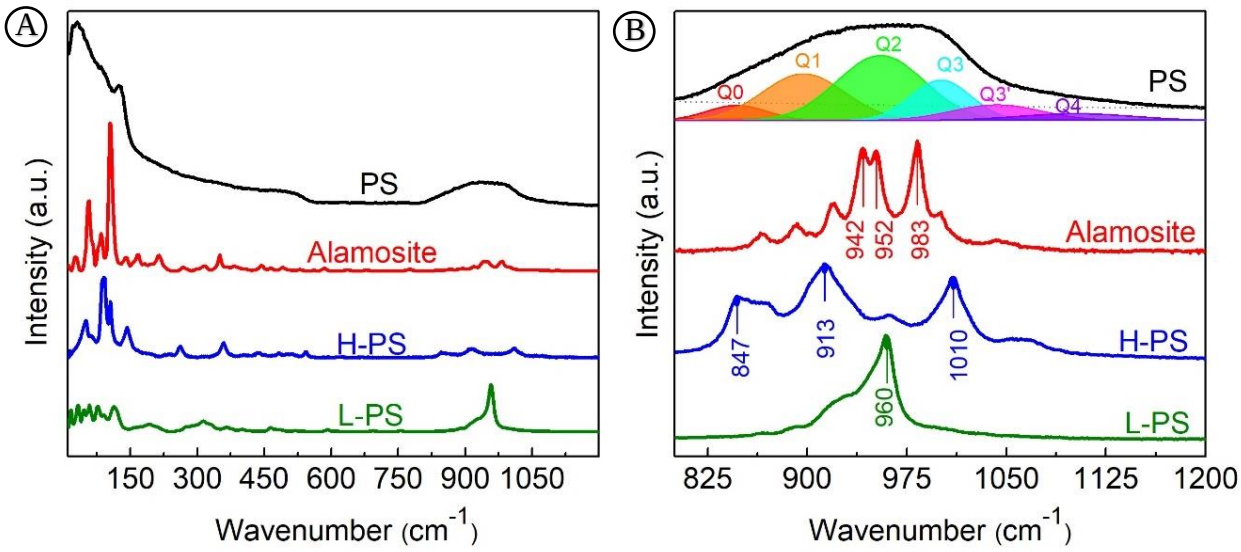

Figure 6.1: (a) Full (10-1200 cm^{-1}) and (b) detailed high-wavenumber (800-1200 cm^{-1}) Raman spectra of PS glass and its three crystalline phases alamosite, H-PS, and L-PS taken at room conditions. Retrieved from Pena et al., 2020 [28].

Without pretension to substitute the classical description of crystals, a more specific picture can be performed in a short-range order (SRO) scale in terms of the Q^n entities. Furukawa and co-workers [73, 74] conducted a detailed investigation of the crystalline phases in the PbO-SiO_2 system, providing their Raman spectra and elucidating their silicate connectivity. According to them, the high-wavenumber Raman features for the alamosite phase are attributed to the complex arrangement of SiO_4 tetrahedra into three distinct Q^2 entities. The L-PS phase shows an intense band at 960 cm^{-1}, associated with the Q^2 tetrahedra constituting chains. On the other hand, the hexagonal phase exhibits a three-summit profile in a spread wavenumber range (847, 913, and 1010 cm^{-1}), proposed to comprise Q^0 to Q^3 entities [73, 74].

Figure 6.1b shows the high-wavenumber region of the Raman spectra for these crystalline polymorphs, whose vibrational bands are in the same spectral region as the Q^n bands in the glass [77]. Despite the different probings between NMR and Raman spectroscopies, chemical shifts and vibrational wavenumbers have an established correlation in the literature [232]. The aforementioned Raman assignments are also consistent with the ^{29}Si NMR spectra obtained in heat-treatments of the PS glass at different temperatures [219]. Such a correlation between NMR and Raman crystalline spectra, along with the isothermal runs presented in Chapter 5 were of utmost importance to understand the crystallization through different metastable phases under different heating conditions, as reported in Ref. [28].

6.3.2. Crystalline Polymorphs Under Extreme Conditions

I. High-Temperature Raman Measurements

Figure 6.2 illustrates the *in-situ* Raman spectra of the three crystalline polymorphs for some selected temperatures. Alamosite is stable over the full range up to 1000 K, whereas the L-PS and H-PS polymorphs transform towards alamosite, in agreement with the inferences of Smart *et al.* [118]. The appearance of the peaks at 960 cm^{-1} arising at about 875 K marks the beginning of the phase transition in both metastable polymorphs. At the low-wavenumber region, also arises a peak at 100 cm^{-1} corresponding to the maximum intensity of the alamosite Raman spectrum (see Fig. 6.1a). The transformation from L-PS to alamosite completes at 900 K, whereas from H-PS to alamosite ceases at 925 K (Fig. 6.2b and Fig. 6.2c).

These results confirm the lack of interconversion from one metastable phase to the other, as both metastable phases transform towards alamosite, with small difference in the transition temperatures. Both characterizations were performed under comparable experimental conditions, sharing the same temperature uncertainties estimated as ±50 K. We highlight the local accurate temperature during the Raman measurements is not an easy task, which unlike pressure does not present a continuing *in-situ* calibration.

At the temperatures where the overall crystallization is probed, the diffusion mechanisms controlling the crystal growth process are attributed to cooperative movements of structural units [10]. An attempting to describe the crystallization pathways will be considered below and is based on the differences in the SRO between the involved phases. For example, the distinct lead environment between the PS glass and alamosite is attributed as the reason for the lack of nucleation of this glass in the bulk [66], and similar arguments could also be a plausible explanation for the alamosite formation through metastable phases. Unfortunately, the local environment around the lead cations is unknown for the metastable crystals in order to proceed in this direction.

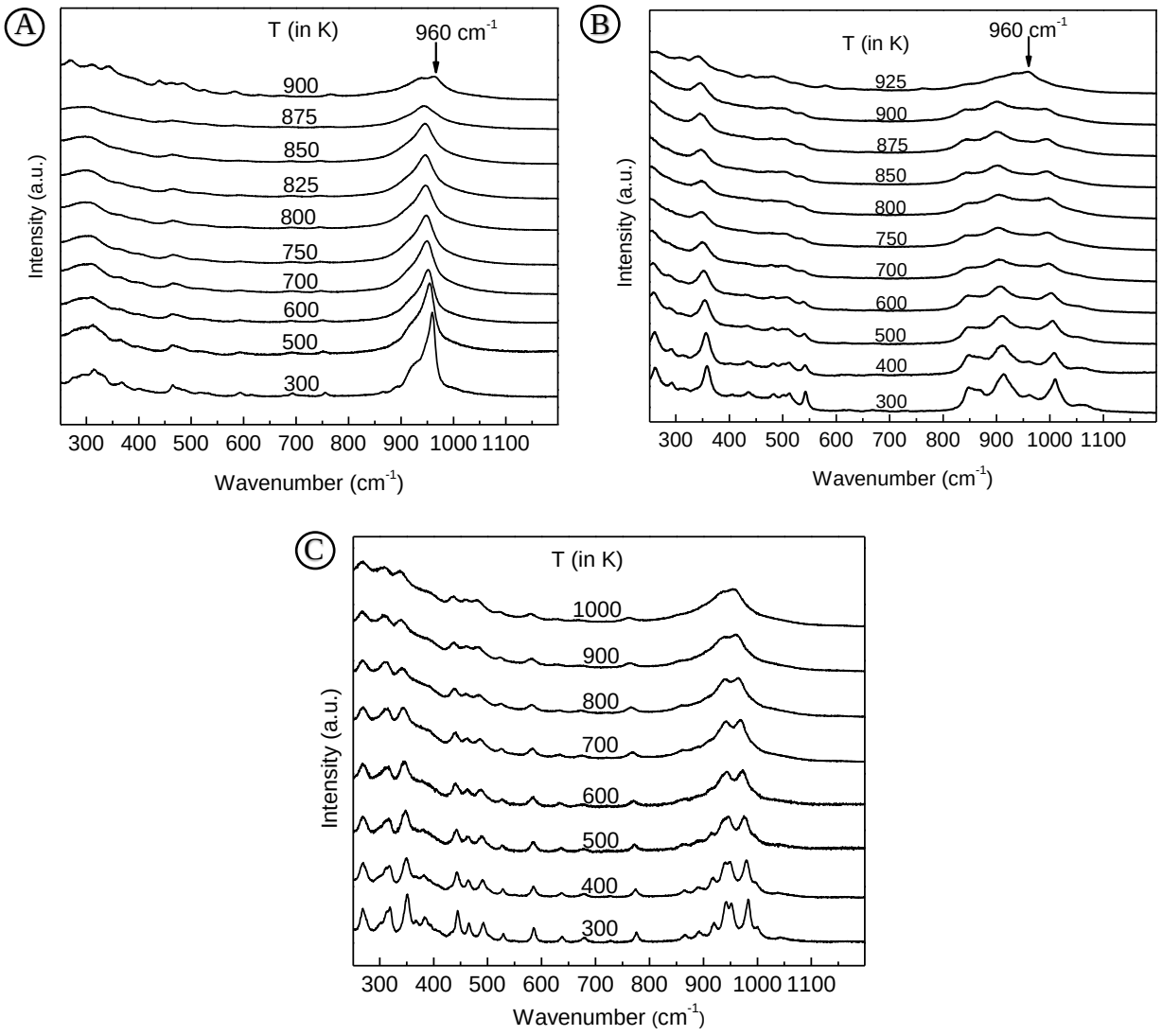

Figure 6.2: In-situ Raman spectra of the three crystalline phases (a) L-PS; (b) H-PS and (c) alamosite as a function of the temperature.

Through the analysis of different metasilicate compositions with different nucleation abilities, Schneider *et al.* [233] proposed the correlation between the bulk nucleation and the similar tetrahedra connectivity between the glass and the isochemical crystal. According to them, these similarities consist of sharing a great amount of tetrahedra having the same connectivity in both phases, and a relatively low Q^n distribution around these tetrahedra in the parental glass. In this sense, the structure of PS glass presents a distribution of Q^n entities, configuring mostly as Q^2 tetrahedra. On the other hand, the ^{29}Si NMR spectrum of alamosite displays three peaks (-84.2, -86.5, and -94.4 ppm) due to three different Si sites [50, 219]. These chemical shift values are attributed to three distinct Q^2 sites [219, 234]. The higher chemical shift was attributed to the Q^2

site presenting a linear Si-O-Si bond, whereas the other peaks cannot be differentiated by Si-O bond length [50]. That said, considering solely the initial and final stages, the phase transformation from the glass toward alamosite occurs with Q^2 tetrahedral formation, where disproportion reactions such as:

$$Q^3_{tot} + Q^1 \rightarrow 2Q^2 \quad (6.1)$$

May explain the tetrahedra transformation during the crystallization, mass balancing silicon, and oxygens [235].

At room conditions, in most of the structural studies, the average Q^n distribution, $<Q^n>$, is higher than the 2.0 expected for the metasilicate composition (see Table 1.1). Such numerical difference is not a mathematical artifact, but an indication of depolymerization reactions (Eq. 1.1) in the phase transformation towards the crystal, as reported in other silicates [236]. In the PbO-SiO_2 glass system, this difference to the nominal $<Q^n>$ values occurs for higher lead content and is attributed to the formation of the lead sub-network [51]. For the PS composition, Raman experiments and MD simulations in a wide range of temperatures comprising the glass, SCL, and melt states appoint to network depolymerization as temperature increases [27]. At the temperatures where the crystallization occurs, the effect of depolymerization reduces the difference between the degree of connectivity from the SCL and alamosite, not necessarily excluding (de)polymerization reactions to take place during the crystallization.

Further considering the intermediary metastable phases, the connectivity degree of alamosite is closer to the L-PS than to the H-PS phase, as reported by Furukawa and coworkers [73, 74]. This way, the crystallization pathway intermediated by H-PS would lead to disproportion reaction and (de)polymerization from the H-PS to the alamosite precipitation, whereas the intermediation by L-PS presents straightforward connectivity to that of alamosite.

II. High-Pressure Raman Measurements

Figure 6.3 shows the *in-situ* Raman spectra of the three crystalline phases as a function of pressure. Qualitatively, we observe that the crystalline polymorphs are stable up to ~ 6 GPa. Such stability would enable the prospective fabrication of the composite material in larger pressure apparatus, where the maximum pressures are lower. The combinatory study of these crystals under extreme conditions by XRD and Raman spectroscopy is in advancement in the GEOR laboratory, and may expand the detailed structural and phonon description of these phases towards high-

pressure and high-temperature conditions (see references therein for the alamosite phase [223, 237]).

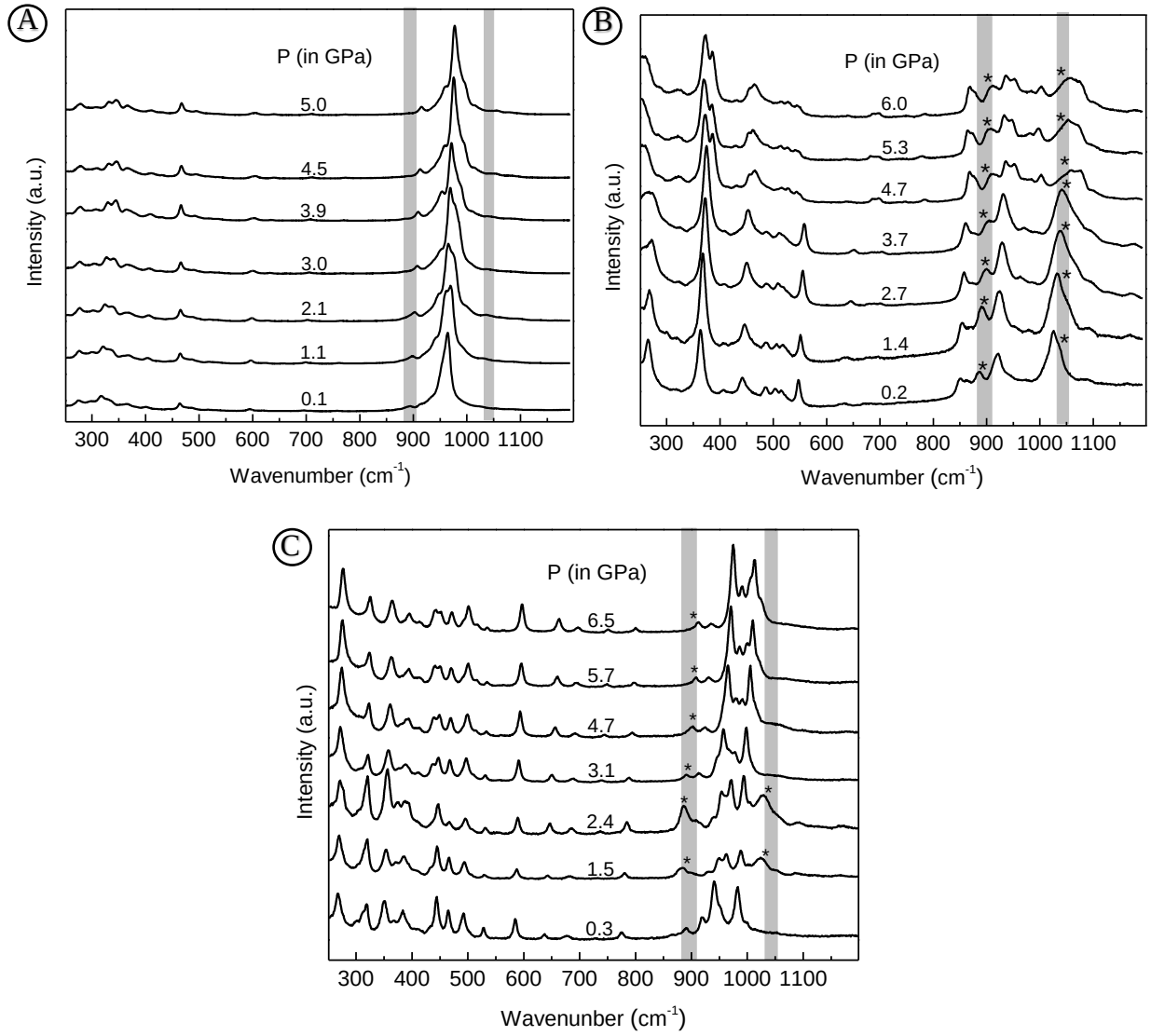

Figure 6.3: In-situ Raman spectra of the three crystalline phases (a) L-PS; (b) H-PS and (c) alamosite as a function of the pressure (P). Shadowed regions exhibit possible parasitic peaks due to the alcohol solution used as the PTM. Alamosite spectra under high-pressure was kindly provided by Dr. Thiago Cunha.

6.4. Summary and Conclusions

Each of the three structural phases crystallized in the PS glass were investigated as a function of high-pressure and high-temperature. Pressure investigations indicated the polymorphs to be stable up to ~6 GPa. Temperature investigations indicate the transformation of both metastable phases into alamosite occurring at comparable temperatures, starting at 875 K. Within

our experimental condition, such a phase-transformations exclude the hypothesis of interconversion from one metastable phase to the other.

The understanding of the structural mechanisms taking place during the overall crystallization is far from a final verdict and should simultaneously address the phase preference intermediated by the L-PS at low temperatures, and the H-PS at higher temperatures. Perhaps, the interplay between disproportion and (de)polymerization reactions permeate the crystallization mechanisms, combined with other structural rearrangements. In this sense, the description of the crystalline structures at room conditions and their subtle modifications already at the temperatures where the crystallization occurs are of paramount importance.

CHAPTER 7 – COBALT DOPED SAMPLES

7.1. Introduction

Glass and glass-ceramics hosts are promising candidates for tunable lasers in the visible and near-infrared regions [238]. In this final chapter, the advances achieved previously to understand the PS composition under extreme conditions are extended toward those doped with cobalt. These materials are optically interesting for their red photoluminescent band, which we attempted to tune with the precipitation in different crystalline phases or pressure effects.

For a fixed dopant concentration, the effects of doping different transition metal ions in lead silicate glasses were addressed therein [239, 240]. Combining optical and magnetic characterizations in a glass matrix composed of 37.9 mol.% PbO, 0.3 mol.% Pb_2O and 61.8 mol.% SiO_2, Baiocchi *et al.* [240] reported the cobalt incorporated in the glass host in the divalent state, Co^{2+} ($3d^7$), with coexisting tetrahedral and octahedral site symmetries, despite displaying the optical absorption spectrum to be characteristic of the former without any features from the latter.

More generally, White and co-workers [241-243] studied the incorporation mechanisms of different transition metal ions in a variety of glass hosts. Due to the similar absorption spectra of cobalt-bearing glass across different compositions, these authors suggested that Co^{2+} is incorporated as 'quasi-molecular complexes', where the ion distorts the local glass network to form a tetrahedron coordinated by NBO [243]. Interestingly, when added to crystalline hosts, Co^{2+} is also reported to preserve its tetrahedral site substantially retaining its average Co-O distance despite the different surrounding environments [244].

This chapter is organized as follows: Firstly, cobalt-doped glasses are investigated by multi spectroscopic techniques for probing the effect of doping on the structure and resulting optical properties at room conditions. In the second section, the simultaneous effect of cobalt doping and temperature on the overall crystallization is explored by *in-situ* Raman and *ex-situ* PL spectroscopies. Finally, the influence of pressure on the optical emission was investigated by PL spectroscopy for the PSCo1.1 glass (1.1 mol.% CoO). Possibilities offered by each variable for tailoring the glass-ceramics optical properties are then critically discussed.

7.2. Experimental Procedures

The set of cobalt-doped glasses was investigated by Raman, optical absorption, and PL spectroscopies. Raman spectra were acquired from 10 to 1300 cm^{-1} in a LabRAM HR micro-Raman spectrometer from Horiba Jobin Yvon using the 532 nm laser wavelength and the 1800 slits/mm grating chosen to proceed with the curve fit of the high-wavenumber region by multiple Gaussian functions. Optical absorption characterizations were performed at room conditions in an Agilent UV-VIS-NIR Cary 5000 spectrophotometer in transmission mode for the spectral range between 350 and 800 nm. PL spectra were acquired at room temperature at the same acquisition conditions as the Raman spectra but using the 600 slits/mm grating and over a wider spectral range covering up to 780 nm. Each PL spectrum is an average of three or four measurements of 20 seconds of accumulation time. The PL signal was curve-fit for one Gaussian function, which enabled the probe of the center position and full width at half maximum (FWHM).

High-temperature *in-situ* Raman characterizations were performed in non-isothermal and isothermal runs. In the former, the temperature was incremented similarly to the characterization of the crystalline polymorphs in Chapter 6. In the latter, the experimental procedure is the same as described in Chapter 5. High pressure was applied in a DAC apparatus and its effect was investigated *in-situ* and *ex-situ* by PL spectroscopy. Pressure calibration was estimated by the evolution of the Raman active phonon modes: comprising the silicon ($\nu_0 = 520.7\ cm^{-1}$) up to 13 GPa, and the center of the diamond cullet ($\nu_0 = 1333\ cm^{-1}$) above this pressure, as described in Chapter 2.

7.3. Results and Discussions

I. Room-Conditions Characterizations

A. Raman Spectroscopy

Figure 7.1 illustrates the evolution of the Raman spectra as a function of the cobalt content, displaying no new peaks as a result of doping. We observe an increase in the intensity of the low-wavenumber to the high-wavenumber region. A plausible cause is an increase in the intensity of the BP due to a higher disordering of the glass structure driven by the incorporation of the cobalt ions. Besides, the high-wavenumber spectral region evolves due to the change in the Q^n distribution, whereas the full area provides the total population that remains invariable, *i.e.*,

$\sum_n Q^n = 100$. Indeed, the barycenter of the high-wavenumber envelope shifts towards lower wavenumbers with cobalt concentration (Fig.7.2a).

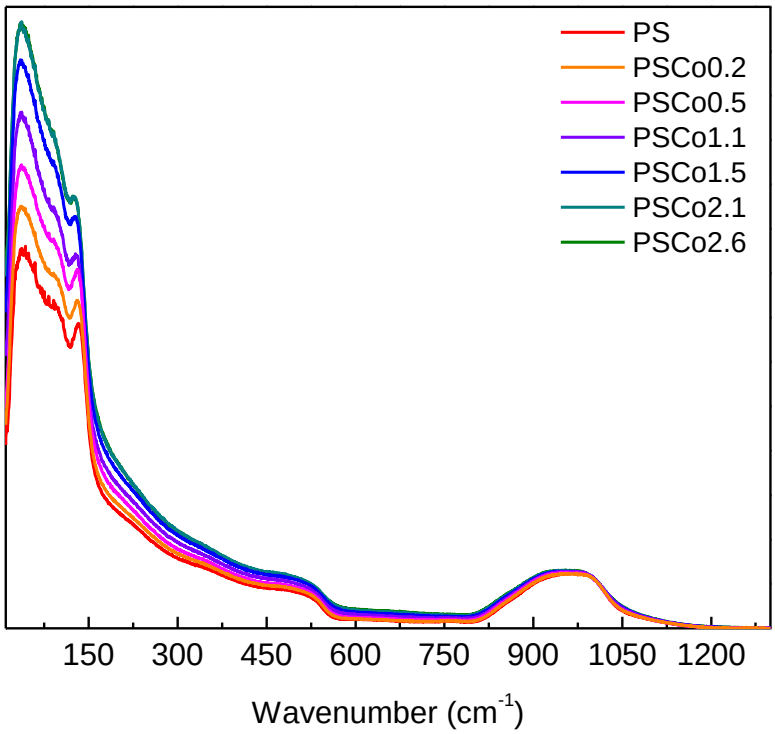

Figure 7.1: Raman spectra of Co-doped PS glass at room conditions. Spectra were normalized by the integrated area comprising the Q^n envelope.

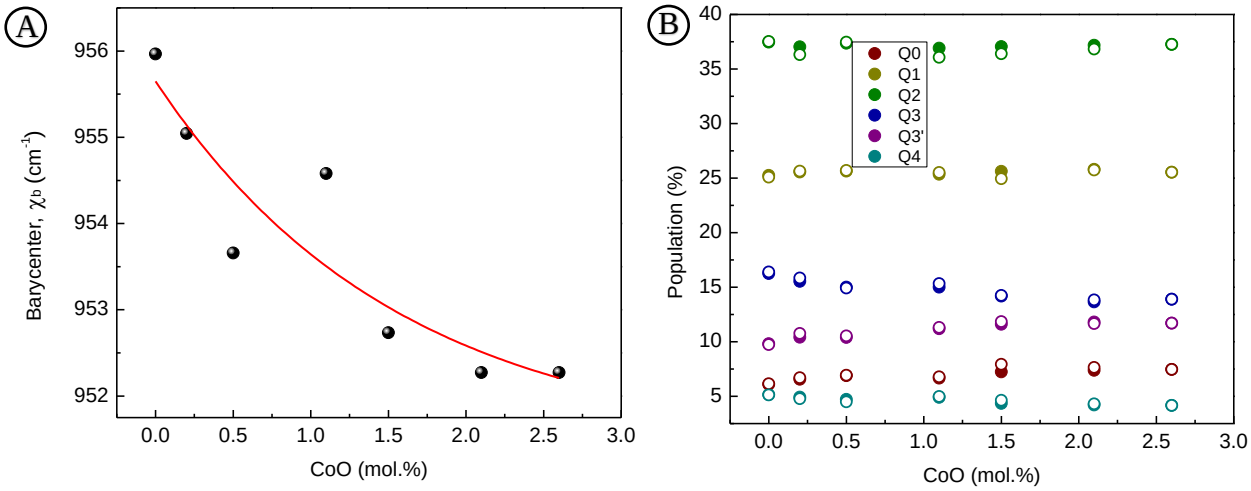

Figure 7.2: Barycenter of the high-wavenumber spectral region and Q^n population as a function of the cobalt concentration. The dots symbolize the P1 (full-colored) and P4 (empty) procedures.

Complementarily, the curve fit of the high-wavenumber envelope indicated subtle modifications in the Q^n distribution (Fig. 7.2b), inducing a decrease in the Q^4 population and consequent depolymerization. The calculated BO and NBO proportions suggested this trend despite the low variation, $\Delta NBO \approx 1\%$ (not shown). Remarkably, the influence of doping on the Q^3 entities is in the same sense as the pressure: cobalt incorporation induces an increase in the $Q^{3'}$ tetrahedra whereas the Q^3 tetrahedra decrease. As a function of the cobalt content, the total Q^3 population is not affected. Recalling the correlation between the distinct Q^3 tetrahedra and the Pb-Si distances, it is straight that cobalt doping favors the structural configuration with shorter distances in between the cations. The increase in the NBO population along with the glass structural rearrangement reiterates the incorporation mechanism as quasi-molecular complexes proposed therein [243].

B. Ultraviolet-Visible Absorption Spectroscopy

Undoped PS glass is essentially transparent in the visible range, presenting a strong absorption below 350 nm attributed in the literature to Pb^{2+} electronic transitions [27]. In contrast, cobalt-doped PS glasses are blue. This change in the color manifests as an intense absorption composed of three peaks centered on 540 nm, 600 nm, and 650 nm (Figure 7.3).

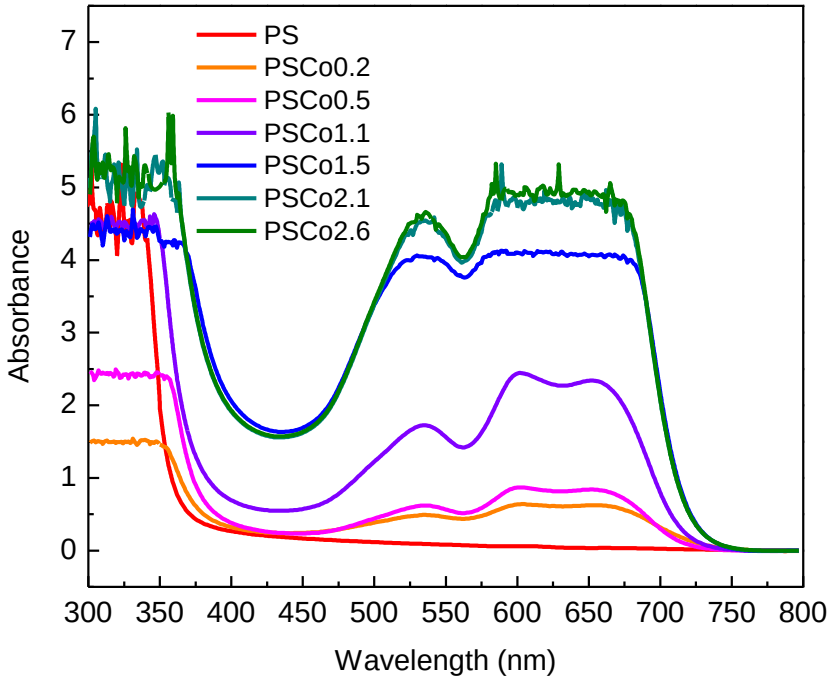

Figure 7.3: Optical absorption spectra of Co-doped PS glass at room conditions.

Absorption spectra of the cobalt-doped PS glasses are similar to that reported by Baiocchi *et al.* [240]. According to these authors, Co^{2+} in the tetrahedral site is responsible for such an absorption attributed to the $^4A_2 \rightarrow {}^4T_1$ spin-allowed transition. In Figure 7.3, we observe a progressive increase in the absorbance of these peaks with the doping content, which is very strong from the lowest doping level investigated here (PSCo0.2). As a matter of fact, Co^{2+} in four-fold coordination is reported to be optically detectable even in the ppm concentration [244]. Despite the characteristic absorption signal of the tetrahedral sites, the co-presence of divalent cobalt highly coordinated (octahedral site) is not ruled out in lead silicate glass and other glass compositions [240, 245, 246].

C. Photoluminescence (PL) Spectroscopy

When excited with a 532 nm laser, Co-doped glasses present a broad PL signal centered on 700 nm. As illustrated in Figure 7.4a, the intensity of this radiative emission signal increases with the cobalt concentration up to 2.6 mol.% where it achieves a plateau (inset Fig.7.4a). The increasing intensity is due to the higher population of tetrahedral cobalt sites. In its turn, the plateau can be attributed either to radiative emission losses in favor of non-radiative emissions (quenching) or to the saturation of the Co^{2+} ions occupying the tetrahedral site in the glass [247]. The energy of the emission is not sensitive to the cobalt content, whereas the width increases about linearly with it (Fig.7.4c).

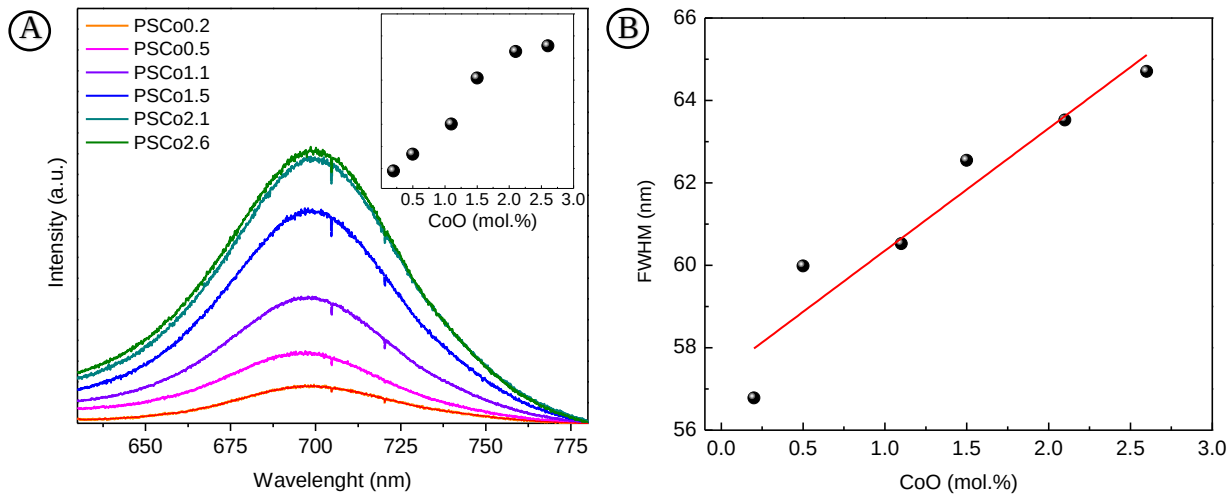

Figure 7.4: (a) PL spectra of Co-doped PS glasses excited with a 532 nm laser at room conditions and (b) respective full width at half maximum (FWHM).

II. High-temperature Characterizations

The simultaneous effects of temperature and doping on the precipitation of the crystalline phases were investigated for the full set of Co-PS glass. In the non-isothermal runs, the temperature was incremented following the same protocol (see page 79) for all compositions. Such a procedure enables in only one run the qualitative characterization of the crystalline phases, and their stability as a function of the temperature, whether the phases are distinct from those precipitated in the PS glass. Figure 7.5 shows the *in-situ* Raman spectral evolution for each sample.

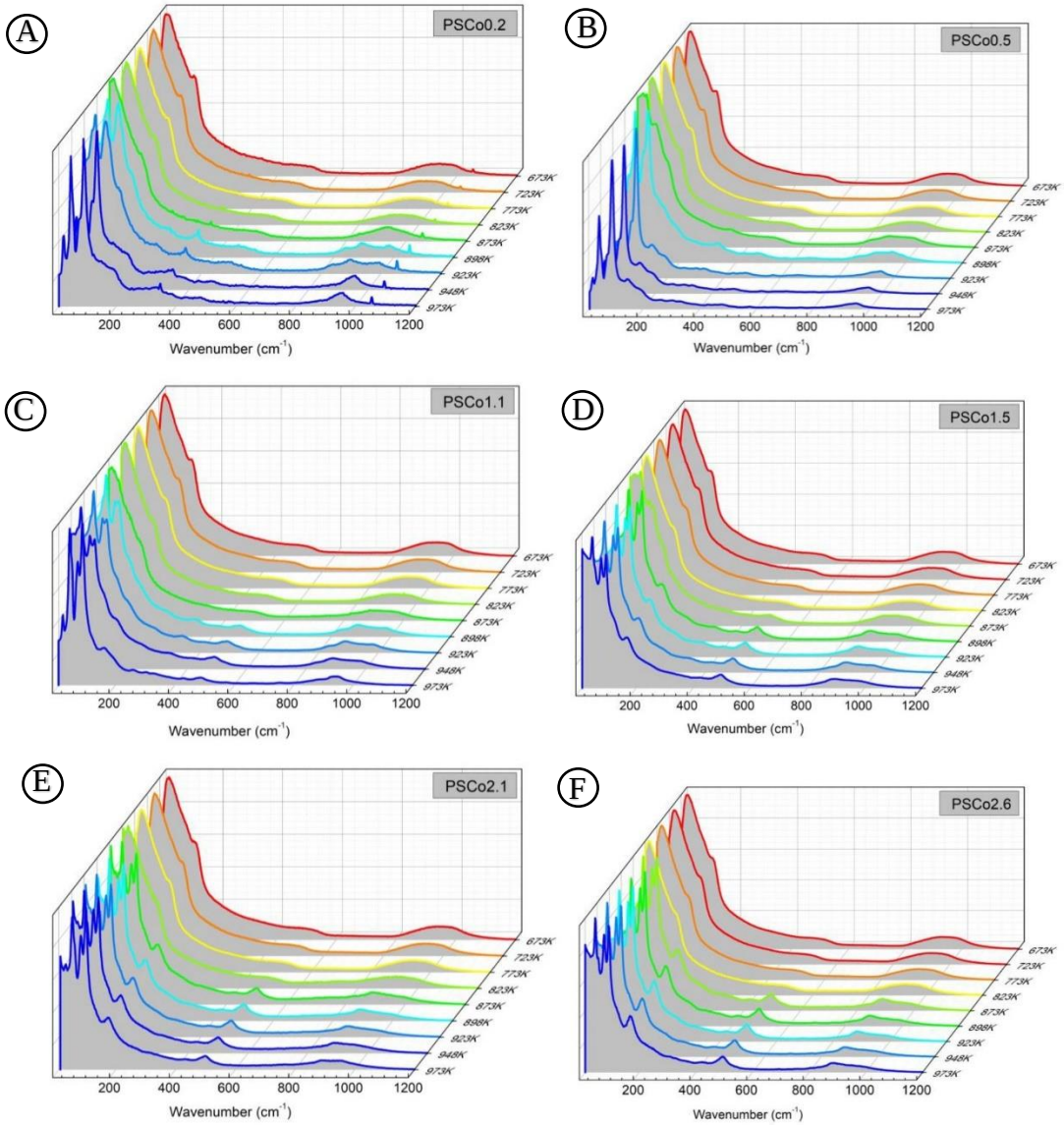

Figure 7.5: Phase evolution in the (a) PSCo0.2; (b) PSCo0.5; (c) PSCo1.1; (d) PSCo1.5; (e) PSCo2.1 and (f) PSCo2.6 samples under non-isothermal treatment.

Table 7.1 summarizes the phase evolution under such a non-isothermal treatment. It is evident that the phase transformation changes expressively for cobalt concentrations above 1.5 mol.% CoO, from where the crystallization occurs without intermediary phases and is stable up to 973 K. It characterizes by the appearance of the Raman peaks centered on 170 and 490 cm^{-1} at high temperatures, which suggests the precipitation of a cobalt-rich phase. Such an occurrence could be linked to the solubility limit of the glass matrix to the transition metal ion doping [27]. Upon the crystal precipitation, the PL signal disappears, dismissing the study of the resulting composite when based on such an optical property. More generally, this statement also holds when the L-PS and alamosite are the major crystallized phases for which there is no PL signal.

Table 7.1: Phase evolution of Co-PS glasses with different cobalt content in non-isothermal heating conditions. Temperatures are in K.

Sample	673	723	773	793	823	873	898	923	948	973	998
PSCo0.2	SCL					L-PS	H-PS		Alamosite		
PSCo0.5	SCL					H-PS			Alamosite		
PSCo1.1	SCL						H-PS			Alamosite	
PSCo1.5	SCL						'New Phase'				
PSCo2.1	SCL						'New Phase'				
PSCo2.6	SCL						'New Phase'				

In the isothermal runs, the PSCo glasses presenting the same crystalline phases as the undoped were submitted to 823 K. As discussed in Chapter 5, in the PS glass such a heating condition induces the precipitation of the metastable L-PS prior to the stable alamosite, whereas from 873K the crystalline pathways evolve from H-PS. Instead, across the doping up to 1.1 mol.% CoO, we observe the predominant formation of the H-PS polymorph that precipitates at temperatures lower than in the undoped glass. As a general trend, cobalt acts as a nucleant agent [6], facilitating the crystallization as described in other multicomponent glass-ceramics [247, 248]. In the case of the cobalt-bearing lead metasilicate, it further lowers the temperatures where the H-PS phase appears.

The doped sample presenting 1.1 mol.% cobalt (PSCo1.1) was selected to be further investigated under extreme conditions, *i.e.*, additional isothermal runs and high-pressure characterization. The reason is two-fold, this composition crystallizes presenting the same phases as the undoped PS glass, and the maximum PL signal.

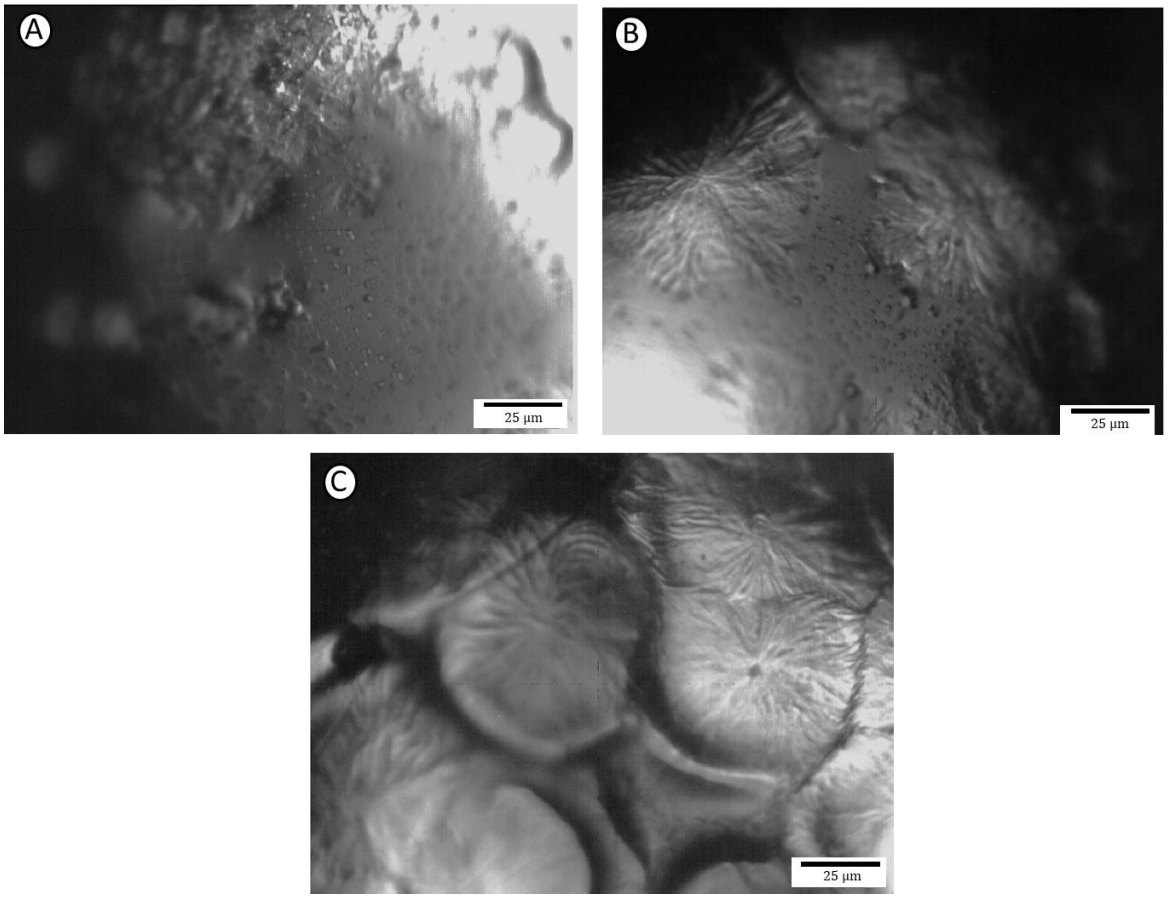

Figure 7.6: Micrographs of the PSCo1.1 glass-ceramics obtained after isothermal heating for (a) 60 minutes;(b) 120 minutes and (c) 180 minutes.

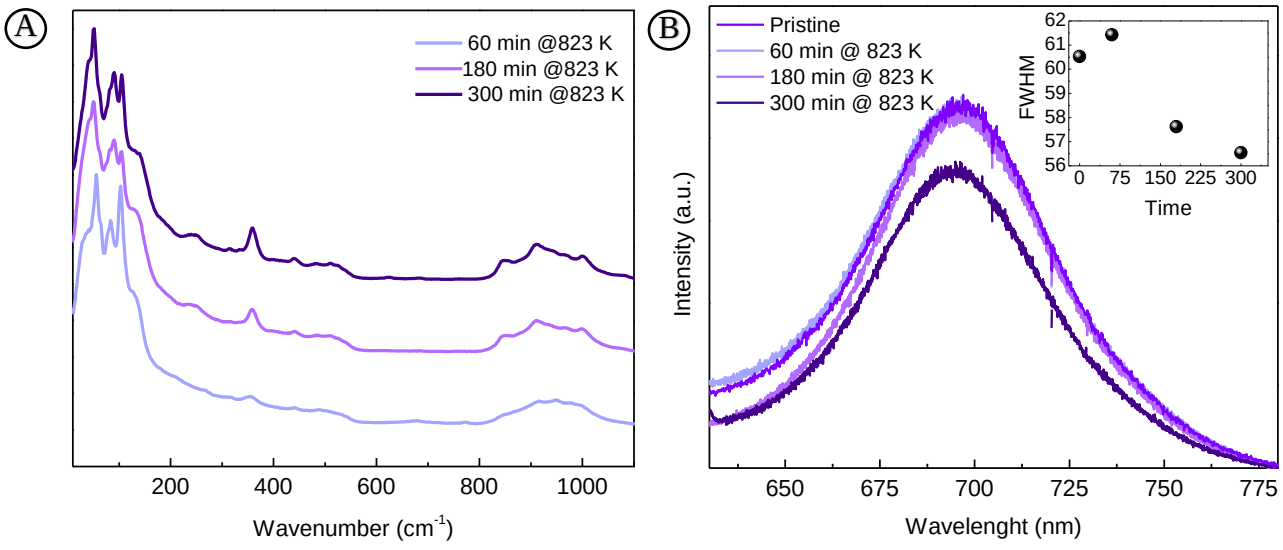

Figure 7.7: (a) Raman and (b) PL spectra of the PSCo1.1 glass-ceramics obtained after isothermal heating for different times.

Figure 7.6 illustrates the *ex-situ* micrographs obtained for the PSCo1.1 glass-ceramics under heat treatment at 823 K for 60, 180, and 300 minutes. We observed the progressive definition of the interface borders between the H-PS crystal and the glass, accompanied by a definition of the characteristic Raman spectra of the crystal (Fig. 7.7a). PL spectra of the resulting composite displayed narrower photoluminescent bandwidth (inset Fig. 7.7b), with values comparable to the lower doping concentration synthesized here, yet redshifting the center position by 5 nm. These modifications occur concomitantly to a subtle decrease in the intensity of the PL signal.

III. High-Pressure Characterizations

High-pressure characterizations were performed for pressures (P) and maximum pressures (Pmax) above the PS glass elastic limit at around ~ 4 GPa [162, 163]. Raman measurements of the undoped PS glass as a function of these distinct variables are described in detail in the third and fourth chapters. The extension of the response under pressure towards the 1.1 mol.% CoO doping is straight, once the uncertainty in determining the Q^n distribution by the Raman curve fit was evaluated as ± 1% [162]. *In-situ* PL investigations of Co-PS glasses presented broad and low intense signals to extract reliable information (not shown). On the other hand, *ex-situ* measurements displayed a decrease in the intensity of the PL signal with Pmax (Figure 7.8), exhibiting little modifications above 8.5 GPa. The peak position decreases to 693 nm, whereas it is inconclusive the pressure effect on the bandwidth, due to the appearance of a tail that arises at about 660 nm.

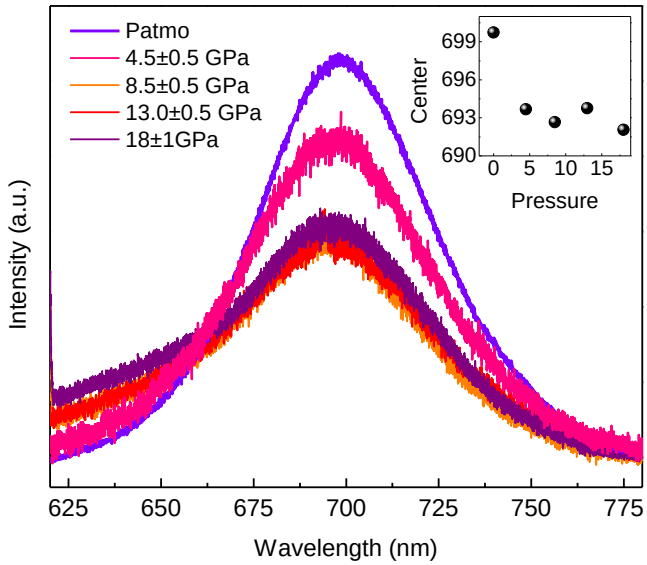

Figure 7.8: Ex-situ PL spectra of the PSCo1.1 glass as a function of the maximum pressure (Pmax).

As addressed in previous chapters, pressure may intrinsically increase the coordination numbers in glasses; further modifying cation-oxygen bond lengths and angles, network polymerization, *etc*. Given that the photoluminescent property is attributed to the tetrahedral coordination within the glass network [240], the decrease in the PL intensity can be attributed to a coordination modification of Co^{2+}. Such an assertion is in line with Tischer *et al.* [249], who studied the effect of pressure on silicate glasses doped with transition metal ions, reporting the cobalt coordination to modify from tetrahedral to octahedral sites. In the case of PSCo1.1 composition, this modification in the coordination is at least partially permanent for the densified glass. Similar pressure-induced coordination change was reported for the densified albite glass doped with 1 wt.% CoO [250].

Two situations may occur: either pressure transforms some tetrahedral into octahedral sites, leading to the coexistence of these entities in the densified glass then absent in the uncompressed glass. Otherwise, the pristine glasses present the octahedral sites at room conditions [240], and pressure affects the equilibrium between tetrahedral and octahedral sites in the glass network, shifting the distribution towards octahedral sites up to a saturation limit.

IV. Tailoring the Glass-Ceramics Optical Properties

The tripod composition-temperature-pressure presents a great number of possible combinations and permutations to be accessed: for a given composition, modifying the temperature and after the pressure, or performing in the opposite order, or both of them simultaneously, may result in different structures, which may lead distinct optical properties. This fascinating characteristic is due to the instability of the glass and its inherent structural dependence on the pressure and thermal histories.

In the case of the cobalt-doped PS glass, each of these variables modifies the photoluminescent signal differently:

i) Increasing cobalt content may increase the population of the tetrahedral sites, positively affecting the PL intensity and broadening the signal bandwidth, not sensibly modifying the emission energy;

ii) Combining composition and temperature affects the precipitated phases, for which only the H-PS polymorph preserved the PL property. Upon its precipitation, different crystallinity degrees may decrease the PL bandwidths and central position wavelengths of the resulting glass-ceramics. Two major challenges can be outlined: First, the promising phase is an intermediate metastable,

whereas longer temperature treatments may lead to the precipitation of the stable and not photoluminescent alamosite. Second, the detailed structure of H-PS is still unknown, making it difficult to understand the exact way how the cobalt ions incorporate into the crystalline phase and its correlation to the optical properties.

iii) Pressure affects the cobalt coordination in the glass, permanently modifying it towards octahedral sites. Because the PL character is due to the cobalt in the tetrahedral site, such a treatment may abruptly reduce the PL signal. Despite the intensity drop, pressure treatments at around 4.5 GPa could be feasible for modifying the central position wavelengths by 6 nm. Higher pressures destructively affect the resulting PL signal without changing any other interesting emission parameter.

7.4. Summary and Conclusions

Cobalt-doped PS glass presents optical properties attributed to the divalent cobalt in tetrahedral sites, which concerns the light absorption centered on the 540 nm, 600 nm, and 650 nm, and a photoluminescent emission centered on 700 nm when excited with 532 nm laser wavelength. These cations are incorporated in the glass structure depolymerizing slightly the silicate network, further favoring the configuration where the cations are closer to each other, as suggested by the increase in the $Q^{3'}$ over Q^3 species.

Crystallization dynamics obtained previously to the PS glass are extended to the doped glass with concentrations up to 1.1 mol.% CoO, with the formation of the same crystalline phases but different characteristic temperatures. Among the three original crystalline phases from the PS glass and the new phase that appeared for higher cobalt concentration, the H-PS phase was the most promising for tuning the PL signal: decreasing its central position wavelength and bandwidth. These results indicate the incorporation of the divalent cobalt in tetrahedral site only in the H-PS phase, which could be further investigated in future studies in view to improve the photoluminescent response.

Pressure treatments decrease the PL signal due to the permanent modification of tetrahedral towards octahedral sites. Such a symmetry conversion occurs not only in the lead metasilicate but seems to be the general rule in cobalt-bearing silicate glasses, possibly with different pressure responses depending on the matrix composition.

GENERAL CONCLUSIONS

Through this thesis work, we succeeded in extending the fundamental comprehension of the lead metasilicate under extreme conditions in the non-crystalline and crystalline states. Raman spectroscopy shed further light on the (i) densification and corresponding glass structure; (ii) phase evolution during the overall crystallization under different heating conditions; and (iii) temperature and pressure stability of the crystalline phases.

The effect of glass densification was investigated at room conditions for maximum pressures up to 23 GPa. Above 4 GPa, a compression-decompression cycle induces subtle network depolymerization that ceases at 20 GPa, with these pressures corresponding to the elastic and saturation limits, respectively. Upon compression, the glass network gradually polymerizes, presenting mostly Q^3 instead the Q^2 tetrahedra that are the highest population in the uncompressed glass. MD simulations further indicate a decrease in the cation-oxygen distances and formation of highly coordinated lead cations, whereas silicon retains the tetrahedral coordination. The resulting depolymerization observed in the densified glass probably occurs during decompression as suggested by the decrease of the barycenter values.

For the investigation of the glass structure as a function of the maximum pressure and pressure, the complementary analysis of the high-wavenumber region of the Raman spectra either by the one-parameter barycenter or by the multi-component curve fit showed good agreement. Such a fact suggests using the former in the 'fast analyses' regarding polymerization and depolymerization trends for a given silicate composition. Beyond the anharmonic effects on the vibrational modes, an expressive increase on the barycenter is linked to polymerization, whereas a relevant decrease may indicate depolymerization.

Lead metasilicate glass presents three crystalline phases: L-PS, H-PS, and alamosite. The crystallization occurs by the intermediary formation of two metastable phases before the alamosite, with the pathways depending on the temperature. Through the *in-situ* Raman investigation of the overall crystallization, we achieved the ideal conditions to stabilize the three crystalline phases by heat-treating the PS glass, which enables the potential development of future composite materials based on their combination. Noteworthy, the H-PS phase was previously described in the literature to be obtained solely from the slow cooling of the melt. The high-temperature investigation of L-

PS and H-PS elucidates the glass crystallization routes not occurring through the interconversion from one metastable to the other, as both crystals transform into alamosite at comparable temperatures. The detailed description of their crystalline structures may aid in building a fundamental comprehension of the crystallization pathways. The overall crystallization protocols performed here could be extended to other glass compositions providing further knowledge on the relevant but underexplored crystallization by the formation of metastable phases.

These concepts were transposable to the doped glass with cobalt content up to 1.1 mol.%, for which the low level of doping does not markedly modify the glass structure, nor the final crystalline phases precipitated, providing an interesting optical property, the photoluminescence. The controlled partial crystallization of the H-PS phase presents potential optical properties, which could be further improved in future studies. At room temperature, this crystalline phase presents pressure stability up to 6 GPa, whereas pressures higher than 4.5 GPa affect destructively the photoluminescent emission of the glass matrix. These pressure limits make it feasible to produce these composite materials in larger pressure apparatuses, from which macroscopic properties could be further investigated and tailored. To this aim, the number of possible combinations and permutations of the different temperature-pressure processing is unlimited.

Some perspectives and prospective fundamental works applying Raman spectroscopy as the main probe to investigate the PS glass comprise:

1) As a function of the temperature

(i) The relaxation of the densified glass structure, whether and how the Q^n population evolves under successive temperature treatments;

(ii) The overall crystallization of the pressure-induced glass structure, whether the densification modifies the kinetics;

2) As a function of pressure

(iii) Quantitatively describe the modifications on the low-wavenumber region comprising the Boson Peak and the two peaks attributed to lead vibrational modes;

3) As a function of the temperature and pressure

(iv) The *in-situ* structural modification during the hot-compression of the glass and its distinction to the cold-compression;

(v) The overall crystallization, whether the crystalline routes remain the same as in the uncompressed glass.

REFERENCES

1. Zanotto, E.D., *Bright future for glass-ceramics.* American Ceramics Society Bulletin, 2010. **89**(8): p. 19-27.

2. Deubener, J., et al., *Updated definition of glass-ceramics.* Journal of Non-Crystalline Solids, 2018. **501**: p. 3-10.

3. Müller, R., E.D. Zanotto, and V.M. Fokin, *Surface crystallization of silicate glasses: nucleation sites and kinetics.* Journal of Non-Crystalline Solids, 2000. **274**(1): p. 208-231.

4. Hishinuma, A., *Crystal nucleation in glass-forming liquid.* 1986, Massachusetts Institute of Technology.

5. Stookey, S.D., *History of the Development of Pyroceram.* Research Management, 1958. **1**(3): p. 155-163.

6. DeCeanne, A.V., et al., *Examining the role of nucleating agents within glass-ceramic systems.* Journal of Non-Crystalline Solids, 2022. **591**: p. 121714.

7. Sugano, S., *Multiplets of transition-metal ions in crystals*. 2012: Elsevier.

8. Bray, K.L., *High Pressure Probes of Electronic Structure and Luminescence Properties of Transition Metal and Lanthanide Systems*, in *Transition Metal and Rare Earth Compounds: Excited States, Transitions, Interactions I*, H. Yersin, Editor. 2001, Springer Berlin Heidelberg: Berlin, Heidelberg. p. 1-94.

9. Hynes, M.J. and B. Jonson, *Lead, glass and the environment.* Chemical Society Reviews, 1997. **26**(2): p. 133-146.

10. Cassar, D.R., et al., *Elemental and cooperative diffusion in a liquid, supercooled liquid and glass resolved.* The Journal of Chemical Physics, 2017. **147**(1): p. 014501.

11. Neiman, T.S., H. Yinnon, and D.R. Uhlmann, *Crystallization kinetics of lead metasilicate.* Journal of Non-Crystalline Solids, 1982. **48**(2): p. 393-403.

12. Lindner, R., W. Hassenteufel, and Y. Kotera, *Diffusion of Radioactive Lead in Lead Metasilicate Glass.* Z. Phys. Chem., 1960. **23**: p. 408.

13. Schaeffer, H.A., *The application of silicon-30 in self-diffusion investigations.* Phys. Status Solidi A, 1974. **22**: p. 281.

14. Langanke, B. and H. Schmalzried, *Ionic Transport in PbO–SiO_2 Melts (I). Tracerdiffusion and Chemical Interdiffusion.* Ber. Bunsengesellschaft Phys. Chem., 1979. **83**: p. 59.

15. Yoshimoto, M. and N. Soga, *Elastic Properties and the Short- and Medium-Range Structures of Lead Silicate Glasses.* Yogyo-Kyokai-Shi(J. Ceram. Soc. Jpn.), 1986. **94**(10): p. 1041-1048.

16. Yoshihoto, M. and N. Soga, *The effect of composition on crack propagation in lead silicate glasses.* Journal of Non-Crystalline Solids, 1987. **95-96**: p. 1039-1046.

17. Kaur, A., et al., *Structure–property correlations in lead silicate glasses and crystalline phases.* Phase Transitions, 2013. **86**(8): p. 759-777.

18. Cohen, B.M., D.R. Uhlmann, and R.R. Shaw, *Optical and electrical properties of lead silicate glasses.* Journal of Non-Crystalline Solids, 1973. **12**(2): p. 177-188.

19. Dimitrov, V.V., et al., *Third Harmonic Generation in PbO-SiO_2 and PbO-B_2O_3 Glasses.* Journal of the Ceramic Society of Japan, 1993. **101**(1169): p. 59-63.

20. Weinstein, I.A., A.F. Zatsepin, and Y.V. Shchapova, *The phonon-assisted shift of the energy levels of localized electron states in statically disordered solids.* Physica B: Condensed Matter, 1999. **263**: p. 167-169.

21. Weinstein, I.A., A.F. Zatsepin, and V.S. Kortov, *Effects of structural disorder and Urbach's rule in binary lead silicate glasses.* Journal of non-crystalline solids, 2001. **279**(1): p. 77-87.

22. Lancelotti, R.F., et al., *Is the structural relaxation of glasses controlled by equilibrium shear viscosity?* Journal of the American Ceramic Society, 2021. **104**(5): p. 2066-2076.

23. Ben Kacem, I., et al., *Structure and properties of lead silicate glasses and melts.* Chemical Geology, 2017. **461**: p. 104-114.

24. Ouchi, Y. and E. Kato, *Effects of Alkaline-Earth Metal-Oxides, Nickel-Oxide, and Cobalt Oxide on The Viscosity of Lead-Metasilicate Melts.* Journal of the Japan Institute of Metals, 1979. **43**(7): p. 625-633.

25. Koide, M., et al., *Viscosity and relaxation of glasses below the glass transition temperature.* Thermochimica acta, 1996. **280**: p. 401-415.

26. Nemilov, S., *Viscosity and structure of the glasses of PbO-SiO_2 system* Izv. Akad. Nauk SSSR Neorg. Mater., 1968. **4**: p. 952.

27. Sampaio, D.V., et al., *Chromium in lead metasilicate glass: Solubility, valence, and local environment via multiple spectroscopy.* Ceramics International, 2021.

28. Pena, R.B., et al., *In-situ Raman spectroscopy unveils metastable crystallization in lead metasilicate glass.* Journal of Non-Crystalline Solids, 2020. **546**: p. 120254.

29. Bolt, M., *Glass: The eye of science.* International Journal of Applied Glass Science, 2017. **8**(1): p. 4-22.

30. Morse, D.L. and J.W. Evenson, *Welcome to the Glass Age.* International Journal of Applied Glass Science, 2016. **7**(4): p. 409-412.

31. Zachariasen, W.H., *The Atomic Arrangement in Glass.* Journal of the American Chemical Society, 1932. **54**(10): p. 3841-3851.

32. Zanotto, E.D. and J.C. Mauro, *The glassy state of matter: Its definition and ultimate fate.* Journal of Non-Crystalline Solids, 2017. **471**: p. 490-495.

33. Gutzow, I. and J. Schmelzer, *The vitreous state*. 1995: Springer.

34. Zheng, Q., et al., *Understanding Glass through Differential Scanning Calorimetry.* Chemical Reviews, 2019. **119**(13): p. 7848-7939.

35. Mauro, J.C. and M.M. Smedskjaer, *Statistical mechanics of glass.* Journal of Non-Crystalline Solids, 2014. **396-397**: p. 41-53.

36. Elliott, S.R., *Physics of amorphous materials*. 1984, London; New York: Longman.

37. Warren, B.E., *X-Ray Determination of The Structure of Glass.* Journal of the American Ceramic Society, 1934. **17**(1-12): p. 249-254.

38. Galeener, F.L., *The structure and vibrational excitations of simple glasses.* Journal of Non-Crystalline Solids, 1990. **123**(1): p. 182-196.

39. Elliott, S.R., *Medium-range structural order in covalent amorphous solids.* Nature, 1991. **354**(6353): p. 445-452.

40. Henderson, G.S. and J.F. Stebbins, *The Short-Range Order (SRO) and Structure.* Reviews in Mineralogy and Geochemistry, 2022. **87**(1): p. 1-53.

41. Greaves, G.N., *EXAFS and the structure of glass.* Journal of Non-Crystalline Solids, 1985. **71**(1): p. 203-217.

42. Le Losq, C., et al., *Percolation channels: a universal idea to describe the atomic structure and dynamics of glasses and melts.* Scientific Reports, 2017. **7**(1): p. 16490.

43. Nesbitt, H.W., et al., *Direct and indirect evidence for free oxygen (O^{2-}) in MO-silicate glasses and melts (M = Mg, Ca, Pb).* American Mineralogist, 2015. **100**(11-12): p. 2566-2578.

44. Stebbins, J.F., *"Free" oxide ions in silicate melts: Thermodynamic considerations and probable effects of temperature.* Chemical Geology, 2017. **461**: p. 2-12.

45. Hung, I., et al., *Detection of "free" oxide ions in low-silica Ca/Mg silicate glasses: Results from $^{17}O \rightarrow ^{29}Si$ HETCOR NMR.* Journal of Non-Crystalline Solids, 2016. **445-446**: p. 1-6.

46. Stebbins, J.F., *Anionic speciation in sodium and potassium silicate glasses near the metasilicate ($[Na,K]_2SiO_3$) composition: ^{29}Si, ^{17}O, and ^{23}Na MAS NMR.* Journal of Non-Crystalline Solids: X, 2020. **6**: p. 100049.

47. Dayanand, C., G. Bhikshamaiah, and M. Salagram, *IR and optical properties of PbO glass containing a small amount of silica.* Materials Letters, 1995. **23**(4): p. 309-315.

48. Fujiu, T. and M. Ogino, *^{29}Si NMR study on the structure of lead-silicate glasses.* Journal of non-crystalline solids, 1984. **64**(1-2): p. 287-290.

49. Yoko, T., et al., *A ^{207}Pb MAS-NMR study of Pb-containing glasses.* Journal of Non-Crystalline Solids, 1992. **150**(1): p. 192-196.

50. Bessada, C., et al., *^{29}Si MAS-NMR in lead silicates.* Journal of Non-Crystalline Solids, 1994. **168**(1): p. 76-85.

51. Fayon, F., et al., *^{29}Si and ^{207}Pb NMR study of local order in lead silicate glasses.* Journal of Non-Crystalline Solids, 1998. **232-234**: p. 403-408.

52. Fayon, F., et al., *Pb^{2+} environment in lead silicate glasses probed by Pb-L_{III} edge XAFS and ^{207}Pb NMR.* Journal of Non-Crystalline Solids, 1999. **243**(1): p. 39-44.

53. Schneider, J., et al., *Q^n distribution in stoichiometric silicate glasses: thermodynamic calculations and ^{29}Si high resolution NMR measurements.* Journal of Non-Crystalline Solids, 2003. **325**(1): p. 164-178.

54. Takaishi, T., et al., *Structural Study on PbO–SiO_2 Glasses by X-Ray and Neutron Diffraction and ^{29}Si MAS NMR Measurements.* Journal of the American Ceramic Society, 2005. **88**(6): p. 1591-1596.

55. Feller, S., et al., *A multispectroscopic structural study of lead silicate glasses over an extended range of compositions.* Journal of Non-Crystalline Solids, 2010. **356**(6): p. 304-313.

56. Lee, S.K. and E.J. Kim, *Probing metal-bridging oxygen and configurational disorder in amorphous lead silicates: insights from ^{17}O solid-state nuclear magnetic resonance.* The Journal of Physical Chemistry C, 2015. **119**(1): p. 748-756.

57. Alderman, O.L.G., et al., *Lead silicate glass structure: New insights from diffraction and modeling of probable lone pair locations.* Journal of the American Ceramic Society, 2021. **105.** p. 938-957

58. Shrikhande, V.K., et al., *^{29}Si MAS NMR and microhardness studies of some lead silicate glasses with and without modifiers.* Journal of non-crystalline solids, 2001. **283**(1-3): p. 18-26.

59. Bair, G.J., *The Constitution of Lead Oxide-Silica Glasses: I, Atomic Arrangement.* Journal of the American Ceramic Society, 1936. **19**(1-12): p. 339-347.

60. Krogh-Moe, J., *An X-Ray Investigation of Lead Silicate Glass*, in *Zeitschrift für Physikalische Chemie*. 1958. p. 223.

61. Morikawa, H., Y. Takagi, and H. Ohno, *Structural analysis of 2PbO·SiO_2 glass.* Journal of Non-Crystalline Solids, 1982. **53**(1): p. 173-182.

62. Takagi, Y., et al., *X-ray Diffraction Analysis of the PbO–SiO_2 System in the Glassy and the Molten State*. Transactions of the Japan institute of metals, 1985. **26**(7): p. 451-461.

63. Imaoka, M., H. Hasegawa, and I. Yasui, *X-ray diffraction analysis on the structure of the glasses in the system PbO-SiO_2.* Journal of Non-Crystalline Solids, 1986. **85**(3): p. 393-412.

64. Kohara, S., et al., *Lead silicate glasses: Binary network-former glasses with large amounts of free volume.* Physical Review B, 2010. **82**(13): p. 134209.

65. Suzuya, K., S. Kohara, and H. Ohno, *A reverse monte carlo study of lead metasilicate glass.* Japanese Journal of Applied Physics, 1999. **38**(S1): p. 144.

66. Mastelaro, V.R., et al., *Relationship between short-range order and ease of nucleation in $Na_2Ca_2Si_3O_9$, $CaSiO_3$ and $PbSiO_3$ glasses.* Journal of Non-Crystalline Solids, 2000. **262**(1): p. 191-199.

67. Rybicki, J., et al., *The structure of lead-silicate glasses: molecular dynamics and EXAFS studies.* Journal of Physics: Condensed Matter, 2001. **13**(43): p. 9781-9797.

68. Smets, B.M.J. and T.P.A. Lommen, *The structure of glasses and crystalline compounds in the system PbO-SiO_2, studied by X-ray photoelectron spectroscopy.* Journal of Non-Crystalline Solids, 1982. **48**(2): p. 423-430.

69. Wang, P.W. and L.P. Zhang, *Structural role of lead in lead silicate glasses derived from XPS spectra.* Journal of Non-Crystalline Solids, 1996. **194**(1-2): p. 129-134.

70. Dalby, K.N., et al., *Resolution of bridging oxygen signals from O 1s spectra of silicate glasses using XPS: Implications for O and Si speciation.* Geochimica et Cosmochimica Acta, 2007. **71**(17): p. 4297-4313.

71. Hagiwara, H. and R. Oyamada, *Raman Spectra of Glassy PbO-SiO_2 System.* Journal of the Physical Society of Japan, 1974. **36**(3): p. 917-917.

72. Worrell, C.A. and T. Henshall, *Vibrational spectroscopic studies of some lead silicate glasses.* Journal of Non-Crystalline Solids, 1978. **29**(3): p. 283-299.

73. Furukawa, T., S.A. Brawer, and W.B. White, *The structure of lead silicate glasses determined by vibrational spectroscopy.* Journal of Materials Science, 1978. **13**(2): p. 268-282.

74. Furukawa, T., S.A. Brawer, and W.B. White, *Raman and Infrared Spectroscopic Studies of the Crystalline Phases in the System Pb_2SiO_4-$PbSiO_3$.* Journal of the American Ceramic Society, 1979. **62**(7-8): p. 351-356.

75. Piriou, B. and H. Arashi, *Raman and Infrared Investigations of Lead Silicate-Glasses.* High Temperature Science, 1980. **13**(1-4): p. 299-313.

76. Ohno, H., et al., *Neutron irradiation effects of PbO-SiO_2 glasses.* Journal of Nuclear Materials, 1991. **179-181**: p. 473-476.

77. Sampaio, D.V., et al., *Raman scattering and molecular dynamics investigation of lead metasilicate glass and supercooled liquid structures.* Journal of Non-Crystalline Solids, 2018. **499**: p. 300-308.

78. Liu, L., *Infrared spectroscopy on lead silicate glass.* Zeitschrift für Physik B Condensed Matter, 1993. **90**(4): p. 393-399.

79. De Sousa Meneses, D., M. Malki, and P. Echegut, *Structure and lattice dynamics of binary lead silicate glasses investigated by infrared spectroscopy.* Journal of Non-Crystalline Solids, 2006. **352**(8): p. 769-776.

80. Cormier, G., T. Peres, and J.A. Capobianco, *Molecular dynamics simulation of the structure of undoped and Yb^{3+}-doped lead silicate glass.* Journal of Non-Crystalline Solids, 1996. **195**(1): p. 125-137.

81. Rybicki, J., et al., *Structure of lead-silicate glasses via constant-pressure MD simulations.* Computer Physics Communications, 1996. **97**(1): p. 191-194.

82. Rybicka, A., et al., *The structure of the first co-ordination shell of Pb atoms in lead-silicate glasses: a molecular dynamics study.* Computational Methods in Science and Technology, 1999. **5**: p. 67-74.

83. Rabinovich, E.M., *Lead in glasses.* Journal of Materials Science, 1976. **11**(5): p. 925-948.

84. Alderman, O.L., *The structure of vitreous binary oxides: silicate, germanate and plumbite networks*. 2013, University of Warwick.

85. Ross, M., *Atomic Diffusion in Glasses Studied with Coherent X-Rays*. 2016: Springer.

86. Ben Kacem, I., *From lead crystal up to domestic waste : role of lead in glass and glass-ceramics : study of PbO-SiO_2, PbO-CaO-SiO_2 and PbO-Al_2O_3-SiO_2 systems*. 2017, Université Paris-Est.

87. Neuville, D.R., D. De Ligny, and G.S. Henderson, *Advances in Raman spectroscopy applied to earth and material sciences.* Reviews in Mineralogy and Geochemistry, 2014. **78**(1): p. 509-541.

88. Parshin, D.A., *Soft potential model and universal properties of glasses.* Physica Scripta, 1993. **T49A**: p. 180-185.

89. Taraskin, S.N., et al., *Origin of the Boson Peak in Systems with Lattice Disorder.* Physical Review Letters, 2001. **86**(7): p. 1255-1258.

90. Duval, E., A. Boukenter, and T. Achibat, *Vibrational dynamics and the structure of glasses.* Journal of Physics: Condensed Matter, 1990. **2**(51): p. 10227-10234.

91. Malinovsky, V.K. and A.P. Sokolov, *The nature of boson peak in Raman scattering in glasses.* Solid State Communications, 1986. **57**(9): p. 757-761.

92. Ruta, B., *Vibrational properties of glasses at the transition from microscopic to macroscopic regime*. 2010, Université Joseph-Fourier - Grenoble I.

93. Duval, E., et al., *Boson peak, nanostructure and relaxation of glasses.* Journal of Non-Crystalline Solids, 1998. **235-237**: p. 203-207.

94. Sokolov, A.P., et al., *Medium-range order in glasses: Comparison of Raman and diffraction measurements.* Physical Review Letters, 1992. **69**(10): p. 1540-1543.

95. Malinovsky, V.K., V.N. Novikov, and A.P. Sokolov, *Log-normal spectrum of low-energy vibrational excitations in glasses.* Physics Letters A, 1991. **153**(1): p. 63-66.

96. Pócsik, I. and M. Koós, *Cluster size determination in amorphous structures using the Boson peak.* Solid State Communications, 1990. **74**(12): p. 1253-1256.

97. Pang, T., *Local vibrational states of glasses.* Physical Review B, 1992. **45**(5): p. 2490-2492.

98. Ando, M.F., et al., *Boson peak, heterogeneity and intermediate-range order in binary SiO_2-Al_2O_3 glasses.* Scientific reports, 2018. **8**(1): p. 5394-5394.

99. Chemarin, C. and B. Champagnon, *Medium range order in sodium silicate glasses: role of the network modifier.* Journal of non-crystalline solids, 1999. **243**(2-3): p. 281-284.

100. Chakraborty, S., et al., *Anomalous variation of Boson peak and fragility and their correlations with intermediate-range structure in PbO-B_2O_3 glasses.* Journal of Alloys and Compounds, 2017. **713**: p. 95-107.

101. Schroeder, J., et al., *Raman scattering and Boson peaks in glasses: temperature and pressure effects.* Journal of Non-Crystalline Solids, 2004. **349**: p. 88-97.

102. Chemarin, C., B. Champagnon, and E. Duval, *Low-frequency Raman scattering in glasses: Thermal treatments and viscosity.* Philosophical Magazine B, 1999. **79**(11-12): p. 2057-2064.

103. Mantisi, B., et al., *Non-Debye normalization of the glass vibrational density of states in mildly densified silicate glasses.* Journal of Physics: Condensed Matter, 2009. **22**(2): p. 025402.

104. Andrikopoulos, K.S., et al., *Pressure dependence of the Boson peak in glassy As_2S_3 studied by Raman scattering.* Journal of Non-Crystalline Solids, 2006. **352**(42): p. 4594-4600.

105. Yagi, M.Y.a.T., *Anharmonicity of low-frequency vibrations in a -GeS_2 studied by light scattering.* EPL (Europhysics Letters), 1999. **47**(4): p. 462.

106. Deschamps, T., et al., *Silica under hydrostatic pressure: A non continuous medium behavior.* Journal of Non-Crystalline Solids, 2009. **355**(48): p. 2422-2424.

107. Sugai, S. and A. Onodera, *Medium-Range Order in Permanently Densified SiO_2 and GeO_2 Glass.* Physical Review Letters, 1996. **77**(20): p. 4210-4213.

108. Morgan, S.H., D.O. Henderson, and R.H. Magruder, *Infrared and Raman spectra of lead fluorosilicate glasses.* Journal of Non-Crystalline Solids, 1991. **128**(2): p. 146-153.

109. Pan, Z., D.O. Henderson, and S.H. Morgan, *A Raman investigation of lead haloborate glasses.* The Journal of chemical physics, 1994. **101**(3): p. 1767-1774.

110. Filho, A.G.S., et al., *Raman spectroscopy study of high B_2O_3 content lead fluoroborate glasses.* Journal of Raman Spectroscopy, 1999. **30**(7): p. 525-529.

111. Sigaev, V.N., et al., *Structure of lead germanate glasses by Raman spectroscopy.* Journal of Non-Crystalline Solids, 2001. **279**(2): p. 136-144.

112. Zahra, A.M., C.Y. Zahra, and B. Piriou, *DSC and Raman studies of lead borate and lead silicate glasses.* Journal of Non-Crystalline Solids, 1993. **155**(1): p. 45-55.

113. Silva, D.C., et al., *Synthesis of $PbO{\cdot}SiO_2$ glass by CO_2 laser melting method.* Journal of Non-Crystalline Solids, 2019. **522**: p. 119572.

114. Lancelotti, R.F., *Relaxação estrutural de vidros metassilicato de chumbo e dissilicato de lítio.* 2021. Universidade Federal de São Carlos.

115. Geller, R.F., A.S. Creamer, and E.N. Bunting, *The System PbO-SiO_2.* J. Res. Natl. Bur. Stand.(US), 1934. **13**(2): p. 237-244.

116. Billhardt, H.W., *Phasenuntersuchungen im System PbO-$PbSiO_3$.* Glastechn. Ber, 1969. **42**(12): p. 498-505.

117. Jak, E., et al., *Thermodynamic optimization of the systems PbO-SiO_2 , PbO-ZnO, ZnO-SiO_2 and PbO-ZnO-SiO_2.* Metallurgical and Materials Transactions B, 1997. **28**(6): p. 1011-1018.

118. Smart, R.M. and F.P. Glasser, *Compound Formation and Phase Equilibria in the System PbO-SiO_2.* Journal of the American Ceramic Society, 1974. **57**(9): p. 378-382.

119. Deschamps, T., et al., *Permanent densification of compressed silica glass: a Raman-density calibration curve.* Journal of Physics: Condensed Matter, 2012. **25**(2): p. 025402.

120. Moulton, B.J.A., et al., *In situ structural changes of amorphous diopside ($CaMgSi_2O_6$) up to 20 GPa: A Raman and O K-edge X-ray Raman spectroscopic study.* Geochimica et Cosmochimica Acta, 2016. **178**: p. 41-61.

121. Jurca, S., H. Chen, and S. Sen, *Structural, shear and volume relaxation in a commercial float glass during aging*. Journal of Non-Crystalline Solids, 2022. **589**: p. 121650.

122. McMillan, P., *Structural studies of silicate glasses and melts—applications and limitations of Raman spectroscopy.* American Mineralogist, 1984. **69**(7-8): p. 622-644.

123. Efimov, A.M., *Vibrational spectra, related properties, and structure of inorganic glasses.* Journal of Non-Crystalline Solids, 1999. **253**(1): p. 95-118.

124. Mysen, B.O., et al., *Curve-fitting of Raman spectra of silicate glasses.* American Mineralogist, 1982. **67**(7-8): p. 686-695.

125. Rossano, S. and B. Mysen, *Raman Spectroscopy of Silicate Glasses and Melts in Geological Systems*, in *Raman spectroscopy applied to Earth sciences and cultural heritage*. 2012, European Mineralogical Union. p. 0.

126. Bancroft, G.M., et al., *Lorentzian dominated lineshapes and linewidths for Raman symmetric stretch peaks (800–1200 cm^{-1}) in Q^n (n = 1–3) species of alkali silicate glasses/melts.* Journal of Non-Crystalline Solids, 2018. **484**: p. 72-83.

127. Nesbitt, H.W., et al., *Factors affecting line shapes and intensities of Q^3 and Q^4 Raman bands of Cs silicate glasses.* Chemical Geology, 2019. **505**: p. 1-11.

128. O'Shaughnessy, C., et al., *The influence of modifier cations on the Raman stretching modes of Q^n species in alkali silicate glasses.* Journal of the American Ceramic Society, 2020. **103**(7): p. 3991-4001.

129. Takemura, K., *Hydrostatic Experiments up to Ultrahigh Pressures.* Journal of the Physical Society of Japan, 2007. **76**(Suppl.A): p. 202-205.

130. Klotz, S., et al., *Hydrostatic limits of 11 pressure transmitting media*. Journal of Physics D: Applied Physics, 2009. **42**(7): p. 075413.

131. Jayaraman, A., *Diamond anvil cell and high-pressure physical investigations.* Reviews of Modern Physics, 1983. **55**(1): p. 65-108.

132. Mackenzie, J.D. and R.P. Laforce, *High-pressure Densification of Glass and the Effects of Shear.* Nature, 1963. **197**(4866): p. 480-481.

133. Barnett, J.D., S. Block, and G.J. Piermarini, *An Optical Fluorescence System for Quantitative Pressure Measurement in the Diamond-Anvil Cell.* Review of Scientific Instruments, 1973. **44**(1): p. 1-9.

134. Datchi, F., et al., *Optical pressure sensors for high-pressure–high-temperature studies in a diamond anvil cell.* High Pressure Research, 2007. **27**(4): p. 447-463.

135. Forman, R.A., et al., *Pressure Measurement Made by the Utilization of Ruby Sharp-Line Luminescence.* Science, 1972. **176**(4032): p. 284.

136. Piermarini, G.J., et al., *Calibration of the pressure dependence of the R_1 ruby fluorescence line to 195 kbar.* Journal of Applied Physics, 1975. **46**(6): p. 2774-2780.

137. Mao, H.K., et al., *Specific volume measurements of Cu, Mo, Pd, and Ag and calibration of the ruby R_1 fluorescence pressure gauge from 0.06 to 1 Mbar.* Journal of Applied Physics, 1978. **49**(6): p. 3276-3283.

138. Mao, H.K., J. Xu, and P.M. Bell, *Calibration of the ruby pressure gauge to 800 kbar under quasi-hydrostatic conditions.* Journal of Geophysical Research: Solid Earth, 1986. **91**(B5): p. 4673-4676.

139. Chijioke, A.D., et al., *The ruby pressure standard to 150 GPa.* Journal of Applied Physics, 2005. **98**(11): p. 114905.

140. Dewaele, A., P. Loubeyre, and M. Mezouar, *Equations of state of six metals above 94 GPa.* Physical Review B, 2004. **70**(9): p. 094112.

141. Zha, C.-S., H.-k. Mao, and R.J. Hemley, *Elasticity of MgO and a primary pressure scale to 55 GPa.* Proceedings of the National Academy of Sciences, 2000. **97**(25): p. 13494-13499.

142. Shen, G., et al., *Toward an international practical pressure scale: A proposal for an IPPS ruby gauge (IPPS-Ruby2020).* High Pressure Research, 2020. **40**(3): p. 299-314.

143. Hanfland, M. and K. Syassen, *A Raman study of diamond anvils under stress.* Journal of Applied Physics, 1985. **57**(8): p. 2752-2756.

144. Mitra, S.S., et al., *Pressure-Induced Phonon Frequency Shifts Measured by Raman Scattering.* Physical Review, 1969. **186**(3): p. 942-944.

145. Whalley, E., A. Lavergne, and P.T.T. Wong, *Hydrostatic optical cell with glass windows for 25 kilobar.* Review of Scientific Instruments, 1976. **47**(7): p. 845-848.

146. Hanfland, M., et al., *Pressure dependence of the first-order Raman mode in diamond.* Physical Review B, 1985. **31**(10): p. 6896-6899.

147. Boppart, H., J. Van Straaten, and I.F. Silvera, *Raman spectra of diamond at high pressures.* Physical Review B, 1985. **32**(2): p. 1423.

148. Tardieu, A., F. Cansell, and J.P. Petitet, *Pressure and temperature dependence of the first-order Raman mode of diamond.* Journal of Applied Physics, 1990. **68**(7): p. 3243-3245.

149. Occelli, F., P. Loubeyre, and R. LeToullec, *Properties of diamond under hydrostatic pressures up to 140 GPa.* Nature Materials, 2003. **2**(3): p. 151-154.

150. Eremets, M.I., *Megabar high-pressure cells for Raman measurements.* Journal of Raman Spectroscopy, 2003. **34**(7-8): p. 515-518.

151. Popov, M., *Pressure measurements from Raman spectra of stressed diamond anvils.* Journal of Applied Physics, 2004. **95**(10): p. 5509-5514.

152. Akahama, Y. and H. Kawamura, *High-pressure Raman spectroscopy of diamond anvils to 250 GPa:Method for pressure determination in the multimegabar pressure range.* Journal of Applied Physics, 2004. **96**(7): p. 3748-3751.

153. Sun, L., A.L. Ruoff, and G. Stupian, *Convenient optical pressure gauge for multimegabar pressures calibrated to 300 GPa.* Applied Physics Letters, 2004. **86**(1): p. 014103.

154. Akahama, Y. and H. Kawamura, *Pressure calibration of diamond anvil Raman gauge to 310 GPa.* Journal of Applied Physics, 2006. **100**(4): p. 043516.

155. Akahama, Y. and H. Kawamura. *Pressure calibration of diamond anvil Raman gauge to 410 GPa*. 2010. IOP Publishing.

156. Mammone, J.F., S.K. Sharma, and M. Nicol, *Raman spectra of methanol and ethanol at pressures up to 100 kbar.* The Journal of Physical Chemistry, 1980. **84**(23): p. 3130-3134.

157. Lemos, V. and F. Camargo, *Effects of pressure on the Raman spectra of a 4:1 methanol–ethanol mixture.* Journal of Raman Spectroscopy, 1990. **21**(2): p. 123-126.

158. Singh, D., Y. Li, and S.C. Sharma, *Effect of pressure on the Raman spectra of methanol–ethanol–water mixture at room temperature.* Journal of Raman Spectroscopy, 2005. **36**(1): p. 24-27.

159. Weinstein, B.A. and G.J. Piermarini, *Raman scattering and phonon dispersion in Si and GaP at very high pressure.* Physical Review B, 1975. **12**(4): p. 1172-1186.

160. Mernagh, T.P. and L.-G. Liu, *Pressure dependence of Raman phonons of some group IVA (C, Si, and Ge) elements.* Journal of Physics and Chemistry of Solids, 1991. **52**(3): p. 507-512.

161. Yoshimoto, M., et al., *Effects of densification on mechanical properties of lead silicate glasses.* Journal of the Ceramic Society of Japan, 1989. **97**(1132): p. 1446-1450.

162. Pena, R.B., et al., *High-pressure plastic deformation of lead metasilicate glass accessed by Raman spectroscopy: Insights into the Q^n distribution.* Journal of Non-Crystalline Solids, 2021. **567**: p. 120930.

163. Pena, R.B., et al., *Normal to abnormal behavior of $PbSiO_3$ glass: A vibrational spectroscopy investigation under high-pressure.* Journal of Non-Crystalline Solids, 2022. **589**: p. 121614.

164. Rouxel, T., et al., *Poisson's Ratio and the Densification of Glass under High Pressure.* Physical Review Letters, 2008. **100**(22): p. 225501.

165. Huang, L. and J. Kieffer, *Amorphous-amorphous transitions in silica glass. II. Irreversible transitions and densification limit.* Physical Review B, 2004. **69**(22): p. 224204.

166. Poe, B.T., C. Romano, and G. Henderson, *Raman and XANES spectroscopy of permanently densified vitreous silica.* Journal of Non-Crystalline Solids, 2004. **341**(1): p. 162-169.

167. Meade, C., R.J. Hemley, and H.K. Mao, *High-pressure X-ray diffraction of SiO_2 glass.* Physical Review Letters, 1992. **69**(9): p. 1387-1390.

168. Deschamps, T., et al., *Elastic Moduli of Permanently Densified Silica Glasses.* Scientific Reports, 2014. **4**(1): p. 7193.

169. Mackenzie, J.D., *High-Pressure Effects on Oxide Glasses: I, Densification in Rigid State.* Journal of the American Ceramic Society, 1963. **46**(10): p. 461-470.

170. Salmon, P.S. and A. Zeidler, *Networks under pressure: the development of in situ high-pressure neutron diffraction for glassy and liquid materials.* Journal of Physics: Condensed Matter, 2015. **27**(13): p. 133201.

171. Deschamps, T., et al., *Soda-lime silicate glass under hydrostatic pressure and indentation: a micro-Raman study.* Journal of Physics: Condensed Matter, 2011. **23**(3): p. 035402.

172. Buchner, S., et al., *X-ray study of lithium disilicate glass: High pressure densification and polyamorphism.* Journal of non-crystalline solids, 2014. **387**: p. 112-116.

173. Buchner, S., C. Radtke, and N.M. Balzaretti, *Densification of lithium disilicate under high pressure investigated by XPS.* 2013.

174. Meade, C. and R. Jeanloz, *Frequency-dependent equation of state of fused silica to 10 GPa.* Physical Review B, 1987. **35**(1): p. 236-244.

175. Lee, S.K., et al., *Degree of Permanent Densification in Oxide Glasses upon Extreme Compression up to 24 GPa at Room Temperature.* The Journal of Physical Chemistry Letters, 2020: p. 2917-2924.

176. Williams, Q. and R. Jeanloz, *Spectroscopic Evidence for Pressure-Induced Coordination Changes in Silicate Glasses and Melts.* Science, 1988. **239**(4842): p. 902.

177. Lin, J.-F., et al., *Electronic bonding transition in compressed SiO_2 glass.* Physical Review B, 2007. **75**(1): p. 012201.

178. Sato, T. and N. Funamori, *High-pressure structural transformation of SiO_2 glass up to 100 GPa.* Physical Review B, 2010. **82**(18): p. 184102.

179. Benmore, C.J., et al., *Structural and topological changes in silica glass at pressure.* Physical Review B, 2010. **81**(5): p. 054105.

180. Susman, S., et al., *Intermediate-range order in permanently densified vitreous SiO_2: A neutron-diffraction and molecular-dynamics study.* Physical Review B, 1991. **43**(1): p. 1194.

181. Xue, X., et al., *Pressure-induced silicon coordination and tetrahedral structural changes in alkali oxide-silica melts up to 12 GPa: NMR, Raman, and infrared spectroscopy.* American Mineralogist, 1991. **76**(1-2): p. 8-26.

182. Wolf, G.H., D.J. Durben, and P.F. McMillan, *High-pressure Raman spectroscopic study of sodium tetrasilicate ($Na_2Si_4O_9$) glass.* The Journal of Chemical Physics, 1990. **93**(4): p. 2280-2288.

183. Dickinson Jr, J.E., C.M. Scarfe, and P. McMillan, *Physical properties and structure of $K_2Si_4O_9$ melt quenched from pressures up to 2.4 GPa.* Journal of Geophysical Research: Solid Earth, 1990. **95**(B10): p. 15675-15681.

184. Kubicki, J.D., R.J. Hemley, and A.M. Hofmeister, *Raman and infrared study of pressure-induced structural changes in $MgSiO_3$, $CaMgSi_2O_6$, and $CaSiO_3$ glasses.* American Mineralogist, 1992. **77**(3-4): p. 258-269.

185. Gaudio, S.J., S. Sen, and C.E. Lesher, *Pressure-induced structural changes and densification of vitreous $MgSiO_3$.* Geochimica et Cosmochimica Acta, 2008. **72**(4): p. 1222-1230.

186. Polsky, C.H., K.H. Smith, and G.H. Wolf, *Effect of pressure on the absolute Raman scattering cross section of SiO_2 and GeO_2 glasses.* Journal of Non-Crystalline Solids, 1999. **248**(2): p. 159-168.

187. Nesbitt, H.W., et al., *Bridging, non-bridging and free (O^{2-}) oxygen in Na_2O-SiO_2 glasses: An X-ray Photoelectron Spectroscopic (XPS) and Nuclear Magnetic Resonance (NMR) study.* Journal of Non-Crystalline Solids, 2011. **357**(1): p. 170-180.

188. Stebbins, J.F., J. Wu, and L.M. Thompson, *Interactions between network cation coordination and non-bridging oxygen abundance in oxide glasses and melts: Insights from NMR spectroscopy.* Chemical Geology, 2013. **346**: p. 34-46.

189. Lee, S.K., et al., *Nature of polymerization and properties of silicate melts and glasses at high pressure.* Geochimica et Cosmochimica Acta, 2004. **68**(20): p. 4189-4200.

190. Allwardt, J.R., B.C. Schmidt, and J.F. Stebbins, *Structural mechanisms of compression and decompression in high-pressure $K_2Si_4O_9$ glasses: an investigation utilizing Raman and NMR spectroscopy of glasses and crystalline materials.* Chemical Geology, 2004. **213**(1): p. 137-151.

191. Hemley, R.J., et al., *Raman Spectroscopy of SiO_2 Glass at High Pressure.* Physical Review Letters, 1986. **57**(6): p. 747-750.

192. Deschamps, T., et al., *Elastic anomalous behavior of silica glass under high-pressure: In-situ Raman study.* Journal of Non-Crystalline Solids, 2009. **355**(18): p. 1095-1098.

193. Champagnon, B., et al., *High pressure elastic and plastic deformations of silica: In situ diamond anvil cell Raman experiments.* Journal of Non-Crystalline Solids, 2008. **354**(2): p. 569-573.

194. Le Parc, R., et al., *In situ high pressure and high temperature Raman studies of $(1-x)SiO_2xGeO_2$ glasses*. Journal of Physics: Condensed Matter, 2009. **21**(37): p. 375109.

195. Muniz, R.F., et al., *In situ structural analysis of calcium aluminosilicate glasses under high pressure*. Journal of Physics: Condensed Matter, 2016. **28**(31): p. 315402.

196. Muniz, R.F., et al., *High pressure effect on the short- and intermediate-range structure of depolymerized soda lime silicate glass: Insights from micro-Raman spectroscopy.* Vibrational Spectroscopy, 2020. **110**: p. 103113.

197. Yen, N.V., et al., *Structural heterogeneity and dynamics in liquid $PbSiO_3$: insight from analysis and visualization of molecular dynamics data.* Materials Research Express, 2015. **2**(6): p. 065201.

198. Hong, N.V., et al., *Microstructure of lead silicate melt under compression: insight from computer simulation.* The European Physical Journal B, 2019. **92**(12): p. 268.

199. Chomenko, K., et al., *The structure of porous and spontaneously densified amorphous $PbSiO_3$: A molecular dynamics study*. Computational Methods in Science and Technology, 2004. **10**: p. 21-38.

200. Bergmański, G., et al., *The structure of rarefied and densified $PbSiO_3$ glass: a molecular dynamics study.* Task quarterly, 2004. **8**(3): p. 393-412.

201. *Challenges and opportunities in atomistic simulations of glasses: a review.* Comptes Rendus. Géoscience, 2022.

202. Welch, R.S., et al., *High-coordinated alumina and oxygen triclusters in modified aluminosilicate glasses.* International Journal of Applied Glass Science, 2022.

203. Wang, Y., et al., *Atomistic insight into viscosity and density of silicate melts under pressure.* Nature Communications, 2014. **5**(1): p. 3241.

204. Lan, M.T., et al., *Computer simulation of $CaSiO_3$ glass under compression: correlation between Si–Si pair radial distribution function and intermediate range order structure.* Materials Research Express, 2017. **4**(6): p. 065201.

205. Ghosh, D.B., B.B. Karki, and L. Stixrude, *First-principles molecular dynamics simulations of $MgSiO_3$ glass: Structure, density, and elasticity at high pressure.* American Mineralogist, 2014. **99**(7): p. 1304-1314.

206. Li, X., et al., *Cooling rate effects in sodium silicate glasses: Bridging the gap between molecular dynamics simulations and experiments.* The Journal of Chemical Physics, 2017. **147**(7): p. 074501.

207. Welch, R.S., et al., *Topological hardening through oxygen triclusters in calcium aluminosilicate glasses.* Journal of the American Ceramic Society, 2021. **104**(12): p. 6183-6193.

208. Drewitt, J.W.E., L. Hennet, and D.R. Neuville, *From Short to Medium Range Order in Glasses and Melts by Diffraction and Raman Spectroscopy.* Reviews in Mineralogy and Geochemistry, 2022. **87**(1): p. 55-103.

209. Sakamaki, T., et al., *Contrasting sound velocity and intermediate-range structural order between polymerized and depolymerized silicate glasses under pressure.* Earth and Planetary Science Letters, 2014. **391**: p. 288-295.

210. Boisen, M.B., et al., *The dependence of the SiO bond length on structural parameters in coesite, the silica polymorphs, and the clathrasils.* American Mineralogist, 1990. **75**(7-8): p. 748-754.

211. Gibbs, G.V., F.C. Hill, and M.B. Boisen Jr, *The SiO bond and electron density distributions.* Physics and Chemistry of Minerals, 1997. **24**(3): p. 167-178.

212. Ostwald, W., *Studien über die Bildung und Umwandlung fester Körper.* Zeitschrift für physikalische Chemie, 1897. **22**(1): p. 289-330.

213. Schmelzer, J.W.P., et al., *How Do Crystals Form and Grow in Glass-Forming Liquids: Ostwald's Rule of Stages and Beyond.* International Journal of Applied Glass Science, 2010. **1**(1): p. 16-26.

214. Fokin, V.M., et al., *Homogeneous crystal nucleation in silicate glasses: A 40 years perspective.* Journal of Non-Crystalline Solids, 2006. **352**(26): p. 2681-2714.

215. Zanotto, E.D., *Glass Crystallization Research — A 36-Year Retrospective. Part I, Fundamental Studies.* International Journal of Applied Glass Science, 2013. **4**(2): p. 105-116.

216. Burgner, L.L., et al., *On the persistence of metastable crystal phases in lithium disilicate glass.* Journal of non-crystalline solids, 2000. **274**(1-3): p. 188-194.

217. Palache, C. and H.E. Merwin, *Alamosite, a new lead silicate from Mexico.* American Journal of Science, 1909. **Series 4 Vol. 27**(161): p. 399-401.

218. McMurdie, H.F. and N. Bunting, *X-Ray Studies of Compounds in The System.* 1939.

219. Lippmaa, E., et al., *High resolution ^{29}Si NMR study of the structure and devitrification of lead-silicate glasses.* Journal of Non-Crystalline Solids, 1982. **50**(2): p. 215-218.

220. Neuville, D., et al., *From glass to crystal. Nucleation, growth and phase separation: from research to applications*. 2017.

221. Furukawa, T. and W.B. White, *Vibrational spectra and glass structure.* Journal of Non-Crystalline Solids, 1980. **38-39**: p. 87-92.

222. Ott, W.R. and M.G. McLaren, *Subsolidus Studies in the System PbO-SiO_2.* Journal of the American Ceramic Society, 1970. **53**(7): p. 374-375.

223. Pena, R.B., et al., *Temperature Effects on the Vibrational Raman-modes of Alamosite ($PbSiO_3$).* Unpublished mansucript.

224. Nakamura, H., K. Tsukamoto, and I. Sunagawa, *In-situ observation of high temperature silicate solutions.* Journal of crystal growth, 1990. **99**(1-4): p. 1227-1231.

225. Abe, T. and I. Sunagawa, *Nucleation, growth and stability of $CaAl_2Si_2O_8$ polymorphs.* Physics and Chemistry of Minerals, 1991. **17**(6): p. 473-484.

226. Abe, T. and I. Sunagawa, *Hexagonal $CaAl_2Si_2O_8$ in a high temperature solution; metastable crystallization and transformation to anorthite.* Mineralogical Journal, 1995. **17**(6): p. 257-281.

227. Mackay, A.L., *The unit cell and space-group of alamosite ($PbSiO_3$).* Mineralogical Magazine and Journal of the Mineralogical Society, 1952. **29**(218): p. 933-935.

228. Boucher, M.L. and E. Peacor Donald, *The crystal structure of alamosite, $PbSiO_3$*, in *Zeitschrift für Kristallographie - Crystalline Materials*. 1968. p. 98.

229. Yamaguchi, O., et al., *New modification of $PbGeO_3$.* Materials Letters, 1984. **2**(3): p. 242-244.

230. Sugii, K., H. Iwasaki, and S. Miyazawa, *Crystal growth and optical properties of lead germanium oxide single crystals.* Journal of Crystal Growth, 1971. **10**: p. 127-132.

231. Oelker, E.N., et al., *Pressure-induced transformations in crystalline and vitreous $PbGeO_3$.* Solid State Communications, 2009. **149**(43): p. 1940-1943.

232. Moulton, B.J.A., et al., *A theoretical and experimental investigation of hetero-vs. homo-connectivity in barium silicates.* American Mineralogist: Journal of Earth and Planetary Materials, 2022. **107**(4): p. 716-728.

233. Schneider, J., et al., *^{29}Si MAS–NMR studies of Q^n structural units in metasilicate glasses and their nucleating ability.* Journal of Non-Crystalline Solids, 2000. **273**(1): p. 8-18.

234. Grimmer, A.R., et al., *^{29}Si-MAS-NMR-Untersuchungen an kristallinen Bleisilicaten.* Zeitschrift für anorganische und allgemeine Chemie, 1987. **547**(4): p. 45-56.

235. Nesbitt, H.W., et al., *Melting, crystallization, and the glass transition: Toward a unified description for silicate phase transitions.* American Mineralogist, 2017. **102**(2): p. 412-420.

236. Nesbitt, H.W., G.M. Bancroft, and G.S. Henderson, *Polymerization during melting of ortho- and meta-silicates: Effects on Q species stability, heats of fusion, and redox state of mid-ocean range basalts (MORBs).* American Mineralogist, 2020. **105**(5): p. 716-726.

237. Cunha, T.R., et al., *Thermal expansion and compressibility of alamosite ($PbSiO_3$) determined by in-situ synchrotron X-ray diffraction.* Ceramics International, 2022.

238. Suresh, B., et al., *Enhancement of orange emission of Co^{2+} ions with Bi^{3+} ions in lead silicate glasses.* Journal of Luminescence, 2016. **172**: p. 47-52.

239. Stroud, J.S., *Optical absorption and color caused by selected cations in high-density, lead silicate glass.* Journal of the American Ceramic Society, 1971. **54**(8): p. 401-&.

240. Baiocchi, E., et al., *Optical and magnetic properties of first-row transition metal ions in lead-silicate glass.* Journal of Non-Crystalline Solids, 1981. **46**(2): p. 203-215.

241. Nelson, C., T. Furukawa, and W.B. White, *Transition metal ions in glasses: Network modifiers or quasi-molecular complexes?* Materials Research Bulletin, 1983. **18**(8): p. 959-966.

242. White, W.B. and D.S. Knight, *Transition metal ion species in glass: a comparison of optical absorption and luminescence evidence.* MRS Online Proceedings Library Archive, 1985. **61**.

243. Nelson, C. and W.B. White, *Transition metal ions in silicate melts. IV. Cobalt in sodium silicate and related glasses.* Journal of Materials Research, 1986. **1**(1): p. 130-138.

244. Dondi, M., et al., *Tetrahedrally coordinated Co^{2+} in oxides and silicates: Effect of local environment on optical properties.* American Mineralogist, 2014. **99**(8-9): p. 1736-1745.

245. Hunault, M., et al., *Local ordering around tetrahedral Co^{2+} in silicate glasses.* Journal of the American Ceramic Society, 2014. **97**(1): p. 60-62.

246. Terczynska-Madej, A., K. Cholewa-Kowalska, and M. Laczka, *The effect of silicate network modifiers on colour and electron spectra of transition metal ions.* Optical Materials, 2010. **32**(11): p. 1456-1462.

247. Satyanarayana, T., et al., *Structural investigations on $PbO–Sb_2O_3–B_2O_3$: CoO glass ceramics by means of spectroscopic and dielectric studies.* Journal of Physics: Condensed Matter, 2009. **21**(24): p. 245104.

248. Tirupataiah, C., et al., *Characterization, optical and luminescence features of cobalt ions in multi-component $PbOAl_2O_3TeO_2GeO_2SiO_2$ glass ceramics.* Optical Materials, 2019. **88**: p. 289-298.

249. Tischer, R.E. and H.G. Drickamer, *Use of pressure to investigate local symmetry and compressibility in glass.* The Journal of Chemical Physics, 1962. **37**(7): p. 1554-1562.

250. Keppler, H. and D.C. Rubie, *Pressure-induced coordination changes of transition-metal ions in silicate melts.* Nature, 1993. **364**(6432): p. 54-56.

251. Kittel, C. and J.K. Gait, *Solid State Physics ed. F. Seitz and D. Turnbull*. 1976, Academic Press, New York.

252. Marder, M.P., *Condensed matter physics*. 2010: John Wiley & Sons.

253. Ashcroft, N.W. and N.D. Mermin, *Solid state physics*. 1976, holt, rinehart and winston, new york London.

254. Madelung, O., *Introduction to Solid-State Theory*. Vol. 2. 1978: Springer Science & Business Media.

255. Thorpe, M.F., *Phonons in amorphous materials.* Kinam, 1982. **4**(serie C): p. 9-32.

256. Thorpe, M.F., *Phonons in Amorphous Solids*, in *Physics of Structurally Disordered Solids*, S.S. Mitra, Editor. 1976, Springer US: Boston, MA. p. 623-663.

257. Vetelino, J.F. and S.S. Mitra, *Dynamics of Structurally Disordered Solids*, in *Physics of Structurally Disordered Solids*, S.S. Mitra, Editor. 1976, Springer US: Boston, MA. p. 541-622.

258. Shuker, R. and R.W. Gammon, *Raman-Scattering Selection-Rule Breaking and the Density of States in Amorphous Materials.* Physical Review Letters, 1970. **25**(4): p. 222-225.

APPENDIX A: PHONONS IN NON-CRYSTALLINE MATERIALS

This section is an extension of the phonon formalism presented in solid-state textbooks, which approaches most fundamentally the crystalline matter [251-253]. Indeed, an interested reader who wants to physically treat the non-crystalline matter with solid-state 'tools' is invited to navigate through the reference therein [36].

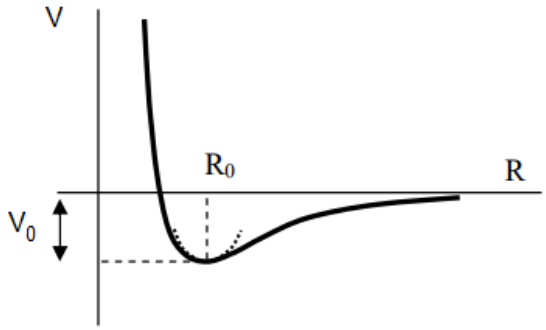

Figure A.1: The potential energy in a one-dimensional solid as a function of the displacement from the equilibrium position.

In any temperature above absolute zero, atoms vibrate about their equilibrium position within the solid structure. The formal calculation of dynamical properties in solids, whether crystalline or not, generally bases on two assumptions [36]. Firstly, the *adiabatic* approximation considers the potential energy in terms of nuclear coordinates, ignoring the relative electronic motion to the nucleus, so that vibrations do not affect the bonding nature. Secondly, the *harmonic*' approximation expands the potential in powers of the displacement from their equilibrium position up to the quadratic term, which is equivalent to assume the elastic response as a linear function of the forces [251].

For simplicity, considering a bound atom in movement in a one-dimensional solid, a typical curve for the binding energy presents a minimum at the equilibrium position (R_0), as illustrates Figure A.1. Describing the potential energy, V(R) as a Taylor expansion series around R_0 provides:

$$V(R) = V_0 + \frac{\partial V}{\partial R}\Big|_{R_0} (R - R_0) + \frac{1}{2}\frac{\partial^2 V}{\partial \mathrm{R}^2}\Big|_{R_0} (R - R_0)^2 \qquad \text{(A.1)}$$

Where $\boldsymbol{s} = R - R_0$ is the instantaneous vector displacement from the equilibrium position. The first term V_0 is the potential energy in equilibrium and does not contribute to the dynamics of vibrations. The second term disappears, once the potential energy at the equilibrium position is a minimum, $\frac{\partial V}{\partial R} = 0$.

The harmonic potential is therefore solely quadratic in the displacement, and in a *three-dimensional solid* is given by [254]:

$$V = \frac{1}{2}\sum_{\substack{n\alpha i \\ n'\alpha' i'}} \frac{\partial^2 V}{\partial R_{n\alpha i}\partial R_{n'\alpha' i'}} \boldsymbol{s}_{n\alpha i}\, \boldsymbol{s}_{n'\alpha' i'} = \frac{1}{2}\sum_{\substack{n\alpha i \\ n'\alpha' i'}} \boldsymbol{\Phi}_{n\alpha i}^{n'\alpha' i'}\, \boldsymbol{s}_{n\alpha i}\, \boldsymbol{s}_{n'\alpha' i'} \qquad \text{(A.2)}$$

Where n runs over N, the number of Wigner Seitz cells in the volume, α runs over r, the number of atoms in the basis. The index i distinguishes the three Cartesian coordinates of the vector $\boldsymbol{s_{n\alpha}}$ that is the instantaneous displacement from equilibrium. The force constant $\boldsymbol{\Phi_{n\alpha i}^{n'\alpha' i'}}$ is a square matrix of order $3Nr$ representing the force in the i-direction acting on the αth atom in the nth cell when the α'th atom in the n'th cell is displaced by unit distance in the i'-direction. From the definition, it is straight the symmetric nature of the Φ components with respect to interchange of indices [36].

The equation of motion can be written as:

$$M_\alpha \ddot{\boldsymbol{s}}_{\boldsymbol{n\alpha i}} = -\frac{\partial V}{\partial s_{n\alpha i}} = \sum_{n'\alpha' i'} \boldsymbol{\Phi_{n\alpha i}^{n'\alpha' i'}}\, \boldsymbol{s_{n'\alpha' i'}} \tag{A.3}$$

With M_α the mass of the αth basis atom. The solutions are periodic in time, *i.e.*

$$\boldsymbol{s_{n\alpha i}(t)} = \frac{1}{\sqrt{M_\alpha}} \boldsymbol{u_{n\alpha i}} \exp^{-i\omega t} \tag{A.4}$$

Where $\boldsymbol{u_{n\alpha i}}$ are the time-independent part of the displacement vector out of a mass factor. Substituting into the equation of motion:

$$\omega^2 \boldsymbol{u_{n\alpha i}} = \sum_{n'\alpha' i'} \frac{\boldsymbol{\Phi_{n\alpha i}^{n'\alpha' i'}}}{\sqrt{M_\alpha M_{\alpha'}}}\, \boldsymbol{u_{n'\alpha' i'}} \tag{A.5}$$

The core of the vibrational description concerns the matrix $\boldsymbol{D} = \frac{\boldsymbol{\Phi_{n\alpha i}^{n'\alpha' i'}}}{\sqrt{M_\alpha M_{\alpha'}}}$ being real and symmetric, and therefore diagonalizable [254]. Mathematically, this step introduces normal coordinates related to the displacement, characterized by the index j, $D^{(j)}$ can be written in terms of eigenvectors $\boldsymbol{u_{n\alpha i}^{(j)}}$ and eigenvalues ω_j^2. For each ω_j, there are $3Nr\boldsymbol{u_{n\alpha i}^{(j)}}$ linearly independent normal modes. Such a procedure formally translates into replacing coupled individual oscillations of the atoms into decoupled collective excitations, which are known as *phonons* in quantum mechanics [36].

The mathematical development above has not assumed anything about the lattice configuration. In section A.1, we simplify the dynamical problem by further considering the translational symmetry due to periodicity in crystals. In section A.2, we discuss the extension of some core dynamical concepts from crystalline to non-crystalline matter.

A.1. Phonons in crystals

In crystalline matter, the presence of translational lattice periodicity reduces the number of equations to be solved from $3Nr$ to $3r$, by the application of Bloch's theorem [36]. Such a simplification is achieved by considering periodic the potential energy given by *Eq.(A.2),* and the eigenvectors as plane-waves modulated by a function with the same periodicity as the lattice [253]:

$$\boldsymbol{u_{n'\alpha'i'}} = c_{\boldsymbol{\alpha i}}(\boldsymbol{R_n}) \exp^{i\boldsymbol{q}\cdot\boldsymbol{R_n}} \tag{A.6}$$

Where $\boldsymbol{R_n}$ is a point in the Wigner-Seitz cell and $\boldsymbol{q}$ is the wavevector related to the size of the unit cell in the reciprocal space (space of coordinates with the dimension of inverse length).

Thus, Eq.(A.5) can be rewritten as

$$\omega^2 c_{\boldsymbol{\alpha i}}(\boldsymbol{R_n}) = \sum_{\alpha' i'} D_{\boldsymbol{\alpha i}}^{\boldsymbol{\alpha' i'}} c_{\boldsymbol{\alpha' i'}}(\boldsymbol{R_n}) \tag{A.7}$$

With the matrix

$$D_{\boldsymbol{\alpha i}}^{\boldsymbol{\alpha' i'}} = \sum_{n'} \frac{\boldsymbol{\Phi}_{\boldsymbol{n\alpha i}}^{\boldsymbol{n'\alpha' i'}}(n'-n)}{\sqrt{M_\alpha M_{\alpha'}}} \exp^{i\boldsymbol{q}\cdot(\boldsymbol{R_n}-\boldsymbol{R_{n'}})} \tag{A.8}$$

It arises that in crystals ω_j is a function of $\boldsymbol{q}$, periodic in the reciprocal space. Consequently, to fully address the dynamical problem one needs to consider only the first Brillouin zone, whose shape is defined by the point group of the crystal [254].

The number of atoms in the basis, r, imposes the number of distinct 'branches' in the Brillouin zone, $3r$. These branches picture the set of phonons as dispersion curves, with the type of branch distinguished by the behavior of $\omega_j(\boldsymbol{q})$ as $\boldsymbol{q}$ tends to zero, *i.e.* the infinite wavelength limit [36]. There are 3 branches for which the frequencies $\omega_j(\boldsymbol{q})$ goes to zero as $\boldsymbol{q}$ goes to zero, displaying for small values of $\boldsymbol{q}$ a linear behavior on the dispersion curve, whose slope is the sound speed; those are referred to as acoustic branches. The other 3 $(r-1)$ branches display finite non-zero frequencies as $\boldsymbol{q}$ tends to zero and are known as optic branches.

For the acoustic modes, in the infinite wavelength limit $(\boldsymbol{q}=0)$, basis atoms move essentially in unison, whereas for the optical modes the atoms vibrate out of phase within the unit cell [252]. At a general value of $\boldsymbol{q}$, the acoustic vibrations are not completely in phase nor are the optic modes out of phase [36].

In first-order scattering process, which comprises the participation of only one phonon, conservation of energy and momentum leads to [251, 252]:

$$E' = E \pm \hbar\omega(\boldsymbol{q}) \tag{A.9}$$

$$\boldsymbol{p}' = \boldsymbol{p} \pm \hbar(\boldsymbol{q} + \boldsymbol{G}) \quad \text{(A.10)}$$

Where the convention adopted is (E', $\boldsymbol{p}'$) for the scattered and (E , $\boldsymbol{p}$) for the incident beams, with the $(+)$ sign referring to absorption and $(-)$ to the emission of one phonon with frequency ω and wavevector $\boldsymbol{q}$ located in the first Brillouin zone.

Note that for a monochromatic beam in the visible spectral region (λ = 400-700 nm), the module of the wavevector $|\boldsymbol{q}| = 2\pi/\lambda \approx 10^{-3}\text{Å}^{-1}$ is small compared to the extension of the Brillouin zone ($2\pi/a \approx 1\text{Å}^{-1}$, where a is the lattice parameter). As a straight consequence of the momentum conservation law stated in *Eq. (A.10)*, Raman spectroscopy access only optical phonons close to the center of the Brillouin zone, *i.e.* $|\boldsymbol{q}| \approx 0$, which also satisfies the non-zero polarizability variation rule, as presented in Eq. (1.8) in the main text.

A.2. Phonons in non-crystalline solids: glass

Considering the topological structural disorder in glass, Bloch's formalism does not hold in simplifying the vibrational dynamics of these materials. It follows that dynamical equations such as *Eq.(1.5)* cannot be diagonalized using plane waves as in crystals [255]. Phonons, *i.e.* quantum of energy in a vibrational mode, still apply to non-crystalline solids, being qualitatively different from crystals for not presenting well-defined $\boldsymbol{q}$ vectors [255].

One can easily understand such distinction by picturing real and reciprocal spaces. As glass structures intrinsically lack translational periodicity, *i.e.* their full structural description would require a unity cell of "infinity" parameter a in real space. Consequently, the mathematical treatment in reciprocal space $\left(\boldsymbol{q} = \frac{2\pi}{a} \to 0\right)$ has no longer physical meaning [36]. The exception lies at the infinite wavelength limit ($\boldsymbol{q} = 0$): on the low-frequency limit, the vibrations are described as acoustic phonons with the distinction that the waves present shorter phonon lifetimes due to the long-range disorder. On the high-frequency limit, the optical modes are no longer plane-waves, but rather spatially localized vibrations [36].

In non-crystalline solids, a broad response over a range of frequencies ω_j occurs, as the excitations are *not* eigenstates of $\boldsymbol{q}$ [256]. Indeed, the phonon wavevector $\boldsymbol{q}$ is not a good quantum number in non-crystalline solids, as the selection rules obeyed by the wavevector are then relaxed, such that all the vibrational modes can take part in the inelastic scattering [257, 258].